Effects of CO_2 on seismic wave speed in Fontainebleau sandstone

by

Md Mizanul Huq Chowdhury

A thesis submitted in partial fulfillment of the requirements for the degree of

Master of Science
in Geophysics

Department of Physics
University of Alberta

Abstract

In geological sequestration CO_2 leakage is a vital concern; consequently monitoring and verifying the subsurface movement and phase behaviour of the injected CO_2 is very important to ensure the integrity of the reservoir. Seismic methods are thought to be one way to monitor the changes in subsurface because the seismic velocities are sensitive to a rock's pore space content. The study of the effect of CO_2 on seismic wave propagation is scientifically interesting because CO_2 can exist in gas, liquid, and supercritical fluid phases over the modest temperature and pressure ranges; CO_2's critical point lies near 31^0C and 7.4 MPa. We have carried out a series of ultrasonic pulse transmission experiments on several samples of fully CO_2 saturated Fontainebleau sandstone over pore fluid pressure ranges of 1 MPa to 20 MPa and at two constant temperatures below (21^0C) and above (50^0C) the critical temperature. These ranges were chosen to cross the gas-liquid and gas-supercritical transitions, respectively. We have noticed a 1.5-2% P-wave speed reduction in our gas to liquid transition while other two transitions show gradual changes. The main motivation of this work is to obtain a good understanding of the rock physics involved with CO_2 as pore fluid. This work also provides an idea of remote seismic detectability of CO_2 in the monitoring process.

“Indeed, in the creation of the heavens and the earth and the alternation of the night and the day are signs for the people of understanding. Who remember God while standing or sitting or [lying] on their sides and give thought to the creation of the heavens and the earth, [saying], ”Our Lord, You did not create this aimlessly; exalted are You [above such a thing]; then protect us from the punishment of the Fire.”

The Holy Quran

Surah Al-Imran, Verse: 190-191

For my parents and my family

Acknowledgements

Very first and foremost I have to thank my supervisor, Douglas R Schmitt, without whom this thesis would not have been possible to be accomplished. He has been showing me the path on this research work as a mentor with his enlightened wisdom and knowledge. I appreciate his open door and always ready to help me on my all kinds of questions and curiosities. Its a great honour for me to work with him as a graduate student.

My especial thanks to our group's post-doctoral fellow Gautier Njiekak who has helped me to understand several theoretical and experimental details makes my work way easier. I also have to offer my heartful thank to Randolf Kofman, our group's research professional, without whose constant assistant in the lab experimental part would be very difficult to finish. I also need to thank Mafijul Islam, my colleague, for helping me on MATLAB codes and Latex formatting of my thesis.

My special thanks to my supervisory committee, Moritz Heimpel, Mark and my external committee member Dr. Alireza Nouri for reading my thesis and also for their valuable remarks.

I also like to thank Sarah Derr who always have helped me all way of my Masters on any kind of academic needs.

I also need to mention the contributions of my parents and my family especially my wife, Nahida Sultana, who always encourage and support me all through my life. Finally I am offering my heartful gratitude to almighty God who has given me the ability to finish this thesis on time.

Contents

List of Tables

List of Figures

Chapter 1

Introduction

This thesis is focused on the effects of CO_2 phase state on the seismic properties of a sandstone. The work is of scientific interest by itself. However, it is motivated by society's need to control the emissions of greenhouse gases of which CO_2 is the most important. Consequently, in this chapter I first review the reasons why we are concerned about greenhouse gas concentrations and describe some of the strategies that have and are being considered for reducing our CO_2 footprints. This general background is then followed by more detailed technical reviews of the existing work with regards to seismic monitoring and laboratory experimentation

1.1 Observed Climate Change

Scientists have been warning the global community about the potential for significant global warming due to rapidly increasing concentrations of greenhouse gases in the atmosphere for over 50 years. The concentrations have increased from about 315 ppm in 1958 and exceeded, for the first time, 400 ppm in late 2013 (Figure 1.1). This increase should by itself be alarming as it well illustrates the geological scale influence that humans now hold. What is further alarming is that CO_2 is a greenhouse gas and its increased concentrations are expected to intensify the greenhouse effect of earth's atmosphere.

The greenhouse effect is responsible for maintaining our planet habitable at an average temperature of 14^0C, life as we know it may not be otherwise possible as without this effect it has been estimated that the average temperature would be only -19^0C. The greenhouse effect is essentially a balancing of energy between that incoming to the earth from the sun and what the earth re-radiates back. The incoming radiation lies mostly within the optical and near infrared regions (from about 300 nm to 3 μm) of the spectrum. This is absorbed to varying degrees and re-emitted as up-going infrared (about 3 μm to 70 μm) waves. This radiation is absorbed by various greenhouse gases who then re-emit it with a proportion returning to the surface. Essentially, the greater the proportion of greenhouse gases the greater is the energy trapped by this process.

Atmospheric components are considered to be greenhouse gases (GHG) if they are strong absorbers of this up-going infrared radiation. Water vapour (H_2O) is by far the strongest absorber and also has the greatest concentration (on average about 0.25% by mass). However, modelling of atmospheric dynamics suggests that Carbon dioxide (CO_2) is the most important GHG contributing to global warming although others such as methane (CH_4) and Nitrous Oxide (N_2O) could also have an impact and their concentrations, too, are rapidly growing. The reason CO_2 is key is because its absorption over the band of 12-15 μm partially closes the strong transmission window of H_20 from about 7 to 15 μm.

There has been considerable controversy with regards to how important GHG gases are. Much of this controversy it driven by economic concerns related to the fact that modern economies rely on the burning of hydrocarbons in one form or another. However, the IPCC (Intergovernmental Panel on Climate Change)[1] in its Fifth Assessment Report (AR5) has listed new evidence for climate change based on various scientific observations all over the world. From this report we know that the global average temperature over the period from 1880 to 2012 and considering the overall land and water surfaces rose 0.85^0C (0.65 to 1.06^0C). If only the oceanic surface is considered (the upper 75m) the temperature increment is 0.11^0C (0.09 to 0.13^0C) per decade over the period of 1971 to 2010.

Excluding those glaciers on the periphery of the ice sheets, globally 226 (91 to 361) Gt/yr of ice is lost from glaciers over the period 1971 to 2009 and 275 (140 to 410) Gt/yr over the period 1993 to 2009. The rise in sea level since the mid-19th century is larger than the average rate of the previous two millennia. Aside from the rapid rate of increase, the overall GHG concentrations in the atmosphere have increased to levels not seen for at least the last 800,000 years. As noted, among the GHG the atmospheric carbon dioxide concentration has increased 40% from the pre-industrial period. Just as worryingly, 30% of the emitted carbon dioxide is being absorbed by the ocean and this results in acidification of seawater. The atmospheric concentrations of CO_2 in 2011 was 391 ppm (part per million), which is the largest of all time (Figure 1.1)

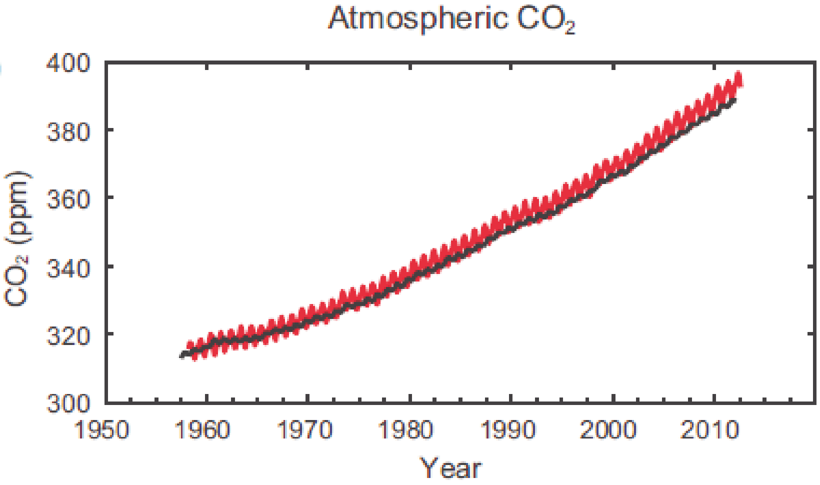

Figure 1.1: Atmospheric concentration of carbon dioxide (CO_2) since 1958. Original source: IPCC, 2013 report [1] and reproduced with permission from IPCC and WMO.

Radiative forcing (RF), a quantity that gives the difference between the radiative energy absorbed by the earth and emitted back to surface relative to the reference year of 1750, is an important indicator of climate change. Positive and negative values of RF implies warming or cooling, respectively. Estimates of the total anthropogenic RF has increased by 43% between the 2005 IPCC-AR4 and 2011 IPCC-AR5 reports. These values are reported relative to those estimated in the year 1750 which is often taken as the starting point for industrialization. The estimated value in 2012 was 2.873 W/m^2 of which CO_2 and CH_4 account for 1.846 W/m^2 and 0.507 W/m^2, respectively [6]

These changes in climate are also believed to result in more severe weather events in recent decades such as frequent storms, floods, tornadoes, blizzards and so on. Other devastating events like change in ecosystem, early season changes, changes in the abundance of algal, plankton, and earlier migration of fish in rivers are also occurring.

One of the reasons behind these changes to climate are the GHG emission, and among these CO_2 is the most responsible. Consequently, it is important to look at where this CO_2 is being produced. The main emission of CO_2 come burning of oil, natural gas, and coal to produce electricity, drive transportation, and provide home and industrial heating. Increasing populations and the building of new cities will demands more energy consumption that in turn leads to more GHG emission.

There is a prediction that global energy usage will double between now and 2050. For these reasons moderating the growth of CO_2 concentrations is important. To mitigate the CO_2 emission scientists are proposing several approaches such as increasing energy efficiency, energy conservation, low or zero carbon alternative energy production, and carbon capture and storage (CCS).

CCS consists of capturing anthropogenically produced CO_2, most usually from large point sources of emission such coal or oil fired electrical generating plants or cement factories, and then safely storing this in a safe place from where it cannot come back to the atmosphere. As will be discussed in detail shortly, after sequestration the gas needs to be monitored. The work in this thesis is motivated by the need to be able to better interpret the observations of active time-lapse seismic investigations carried out as part of the monitoring mandate aspects of CCS. As such, it is necessary to briefly discuss the various CO_2 storage and monitoring scenarios.

1.2 Various CO_2 sequestration methods

Scientists have proposed several methods for CO_2 sequestration. Here we will discuss oceanic, terrestrial, mineral, carbonation, and geological sequestration.

1.2.1 Oceanic

Ocean waters are one of the biggest sinks of the atmospheric CO_2 through dissolution with about 38.5% of CO_2 emissions being naturally taken up by the world's oceans during the last two centuries. Oceanic storage capacity is estimated to be 39,000 Gt-C (Gigaton of carbon) making it one of the main carbon storage candidates [7]. For storage purpose we can inject the CO_2 into the ocean water using pipe lines or ships to deeper than 1000 m. At these temperatures and pressures the CO_2 would directly dissolve into the water until the solubility limit is reached. These strategies cannot be a permanent solution because through the carbon cycle eventually the CO_2 will re-enter the atmosphere. Moreover, the increment in acidification of the ocean water would develop a negative ecological impact that will disturb sea-life [8];[9]. Therefore this oceanic storage is not a permanent solution and rather would create further environment related problems.

1.2.2 Terrestrial ecosystem

Photosynthesis is another natural process in which CO_2 is removed from the atmosphere. Although part of this absorbed CO_2 comes back to the atmosphere through respiration, it is estimated that 2.8 Gt-C per year can be stored in the soil and biomass [7]. To utilize this effect ways to increase the amount of CO_2 captured and stored must be found. Barriers to the re-emission of CO_2 into the atmosphere are by holding it in tress (large capacity vegetation), wood (long life cycle biomass product), stabilized carbon components in soils, minimizing soil disturbance, increment of return of crop residuals to soil, increasing forestation and large carbon capacity plant growth. This process would create complex situations between the ecosystem and atmosphere relations of which scientists still have limited understanding.

1.2.3 Mineral Carbonation

Direct mineral carbonation is a process that converts gaseous CO_2 by reacting it with Mg- and Ca-rich minerals in the earth's crust into a geologically stable, solid final form in carbonates. This is a natural geological process. For using this phenomenon in CO_2 sequestration we need to accelerate the process using pre-treatment (heating, grinding, etc), catalysts and additives to produce carbonates. The mines from where the original silicates or oxides were extracted are suitable place to store the CO_2, which are trapped in the form of stable carbonates. Alternatively, the carbonates can have many uses in society. Among the all storage process in CO_2 sequestration this method is the only where there is no risk of leakage as carbonates are in an inert, stable, solid form.

1.2.4 Geological Sequestration

Geological sequestration is the process where captured CO_2 is injected into suitable subsurface formations typically with high pore volume, that are deeper than 1000 m down to avoid ground waters, and which have cap rocks to contain the stored gas. This process includes the capturing, separating, transporting, and storing in suitable subsurface formation. As we need to trap the sequestrated CO_2, depleted oil and gas reservoirs, coal mines, and saline aquifers are the best candidates for the storage locations. Geophysical monitoring of the storage site is also very important in helping to manage the injection process and to provide warning of any leakage. Figure 1.2 shows how a leak could occur in a geological sequestration site.

Geological sequestration is being used in many countries around the world now. On-going industrial-scale projects include Sleipner, Norway; Weyburn, Canada; In Salah, Algeria and Snohvit, Norway. The Quest project near Edmonton will soon begin operations with a goal of up to 1 Mt-C per year being injected to the basal sands lying immediately above the Canadian Shield.

The Sleipner project, operated by StatOil and partners offshore in the North Sea, is perhaps the longest operating and most famous project. It captures CO_2 from the off-shore natural gas processing platform and injects it back into a saline formation at depths of about 1 km. Five 3-D seismic surveys have already been acquired over this site during 1994(baseline), 1999, 2001, 2002 and 2005 for the purpose of subsurface storage monitoring. Through the seismic imaging a clear idea about the CO_2 plume and containment were verified.

The Weyburn project, operated by Cenovous Energy and Apache Corporation, is an EOR (Enhanced Oil Recovery) project operating in Saskatchewan. The CO_2 captured from a synfuel plant at North Dakota comes to Weyburn oilfield through a 325 Km pipeline crossing the US-Canada border. Different types of monitoring processes are implementing in this EOR project.

At In Salah, a collaboration of BP, Sonatrach and StatOil, CO_2 is captured from natural gas fields, processed at nearby gas plants and transported to the injection site to enhance natural gas recovery. This site has a cap rock of 950 m of impermeable mudstone that will protect the gas from leaking.

Snohvit in the Barents Sea operated by StatOil where CO_2 is injected in a sandstone layer located 2500 m beneath the seabed. Other significant sequestration projects are K12B (Netherlands, gas reservoir, initiated from 2004), Hokkaido (Japan, enhanced coal bed methane, 2004) and CASTOR (Europe, capture and storage, started from 2004) [2]. There are quite a few activities in Canada, particularly in Western Canada. The Alberta Government has committed $2B to projects related to CO_2 reduction. Only one major direct sequestration project has gone ahead at this time, The Shell operated Quest project where CO_2 will be stripped from the emissions at the Shell Scotford oil sands upgrader near Fort Saskatchewan and transported via a dedicated pipeline to a site north of Edmonton. Other projects proposed by Capital Power near Genessee and SaskPower (Boundary Dam 3 CCS Project) are currently on hold and will depend to some degree on the industrial needs for CO_2. CO_2 is being used to lower oil viscosities to enhance petroleum production by Penn West Petroleum near Joffre, Alberta, by Apache with acid gas near Zama, Alberta, by Cenovus and Apache in the Weyburn-Midale CO_2 project in Saskatchewan, and potentially by Spectra Energy near Fort Nelson, British Columbia.

1.3 Monitoring methods

In order to reduce the risks associated with CO_2 sequestration it is very important to have a clear understanding about the geologic, hydrologic, geochemical and geomechanical characteristics of the subsurface. The monitoring aspects of CO_2 sequestration deal with these process and their influences. To obtain and maintain acceptance we need to convince the public that all efforts have been taken to minimize the potential for hazards. Minimizing the possibility of CO_2 leakage from a geological sequestration site, detecting any potential leakage problems, and taking proper proactive action responding to these consequences are main purposes of the monitoring and safety part of a CO_2 sequestration

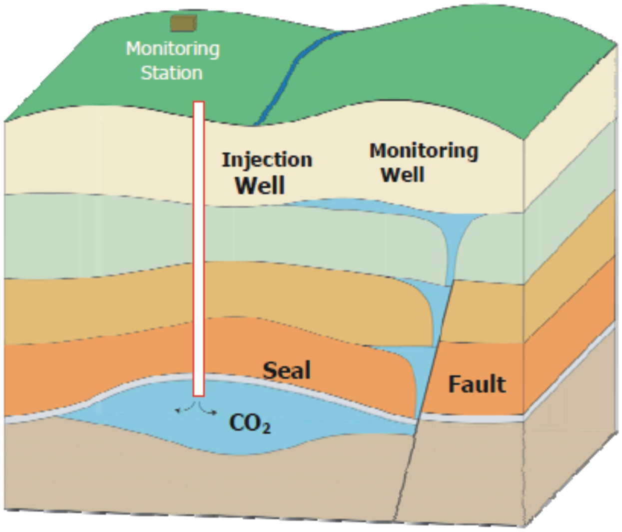

Figure 1.2: This sketch shows the importance of subsurface monitoring. There are layers that providing the sealing and flow barriers but the presence of fault put a risk of possible CO_2 leak through it. Original source: GCEP report 2007 [2] and reproduced with permission from GCEP.

project. In this section we briefly review strategies employed for remotely monitoring the sequestered CO_2 in the subsurface.

There are different monitoring technologies that can be used for preventing or checking for potential leakage in a geological site. The main three geophysical methods used are:

- Geodetic land surface deformation, whereby temporal variations in the ground surface elevations and lateral positions are monitored by repeated levelling, differential global positioning system (GPS), and space-borne interferometric synthetic aperture radar (INSAR).
- Electromagnetic (EM) or Electrical techniques that rely on changes in the electrical conductivity of the rock due variations in the saturation [10, 11].
- Gravitational measurements in which the differences in mass due to the substitution of fluids in the pore spaces are tracked [12, 13].
- Seismological tests in which variations in the seismic wave speeds and densities due to injected fluids and evolving effective stresses change the observed seismic responses, or by the tracking of induced microseismic events [14].

Among these methods seismic imaging is the most widely used and most highly technologically developed. Seismic techniques applied at the surface have a higher resolution than gravity and EM methods and have become the preferred candidate for time-lapse monitoring [4, 15, 16, 17, 18, 19, 20] . The bulk density and elastic stiffnesses of a medium have important effects on the speeds and impedances of a seismic wave (see Chapter 3 for more details). As CO_2 is more compressible and less dense than the oil or brine it replaces, seismic methods give an effective picture when any migration or leakage of CO_2 occurring at in the site using reflected amplitudes and velocity push down effects (i.e. showing low seismic velocity surrounded by rock with higher seismic velocity). The development on this method for making it more efficient and precise on quantitative assumptions is improving day by day through extensive on-going research.

The results of this thesis are most pertinent to the interpretation of active source seismic techniques, i.e. those which employ a triggered seismic source such as dynamite or seismic vibrators to produce seismic waves that are then detected using receivers such as geophones. It is the processed data from such surveys that, when repeated, can show the movement of CO_2 in the subsurface. Such surveys can be carried out in the following geometries of:

- Vertical seismic profiling in which geophones are placed along the borehole and the source is activated at the surface. This provides hard information about the time that it takes seismic waves to arrive at a given depth, on the in-situ seismic wave speeds, and on the true depths of the reflectors [21].
- Cross-well seismic profiling in which sources and receivers are placed in two nearly vertical boreholes [22, 23]. Tomographic images can be obtained from these data that provide high resolution structural information.
- Most importantly, surface seismic profiling or 3D surveys provide the widest spatial and geometric information coverage for the CO_2 plume in the site.

Among these methods surface seismic is widely used in various CO_2 sequestration projects such as Sleipner, Weyburn [24],Salalh, and Snohvit.

1.4 Literature reviews on laboratory work on CO_2 sequestration

As noted above, surface seismic profiling is the most popular for monitoring purposes. To date, such surveys have been very useful for highlighting zones where changes in the subsurface conditions have occurred. However, there have not to our knowledge been any more advanced quantitative interpretations applied to such data. A quantitative interpretation (QI) might yield information on in-situ fluid saturations and extrinsic pressures and temperatures. For QI it is very important to know about the variations in the elastic properties and density resulting from the fluid replacement or fluid distribution in the reservoir. That is, how will the seismic wave speeds and density change as CO_2 is injected to the reservoir?

In normal QI, well log information is used to provide relationships between various parameters such as P-wave speed and porosity, and in the vernacular of QI these relationshiops have been called templates. These templates are usually empirically derived from well log information through the reservoir. These well logs do not contain any information on how the rock physical properties will vary with saturation, pressure, or temperature and are insufficient to properly analyse the time lapse results. For this purpose ultrasonic laboratory measurements on rock samples saturated with CO_2 are necessary. The advantage of the laboratory setting is that the sample and its saturating fluids can be controlled. The disadvantage of such measurements is that they take place on small pieces of rock and that the measurements are typically made at high frequencies. Although large economic investments have already been made in developing CO_2 sequestration projects and in collecting surface seismic data, there are remarkably few studies that have directly focused on obtaining the requisite laboratory information. Indeed, it could be argued that the only public domain data extant has been produced in our laboratory. Now we will discuss briefly about the up-to-date literature on this seismic velocity measurements using rock physics.

Initially there was little outside motivation to study the effects of CO_2 on seismic velocity. Sequestration as a concept had not been developed. However, it has long been known that oil with CO_2 dissolved in it has a lower viscosity and hence flows more easily. For this reason, the earliest experiments were carried out on sandstones initially saturated with oil with CO_2 then injected. The pioneered work on laboratory experiments involving CO_2 as a pore fluid saturant was done by Wang and Nur [25] who flooded CO_2 into hexadecane -saturated sandstones (porosity ranging from 6%- 29%) and measured their elastic responses through P- and S-wave velocities. In their experiments measurements were carried out over the temperature range from 20^0C to 70^0C while the applied pore pressure varied from 2 to 16 MPa. Their observed P-wave velocities showed a notable decrease due to various porosity, temperature, and effective pressure while S-wave velocities showed very little change. They did not interpret these results in any way other than provide the empirical observations.

Xue and Oshumi [26] from RITE (Research Institute of Innovative Technology for the Earth) in Japan published an experimental study of effects of CO_2 injection on the P-wave velocities and mechanical change of water-saturated Tako sandstone. Their result showed that the largest decrease in P-wave velocities occurred when the injected CO_2 that displaced the water from the pore space of the sandstone is in supercritical phase. In a series of 2006 and 2009, Xue and Lei [27, 28] used differential arrival time to present the changes occurring in the P-wave velocity during CO_2 injection and showed the CO_2 migration and water displacement map in an efficient way. Shi, Xue and Durucan

[20] published a work where CO_2 distribution is imaged in a water-filled core. Significant reductions in P-wave velocity were observed in all cases just after the injection started. However, the observed velocities with different saturations showed a large disagreement with Gassmann's prediction [29] in the case of low-frequency poroelastic response (i.e. solid matrix shows elastic response while fluid inside the pores responses viscously) of rock. Further, their measurements essentially consisted of a flow-through geometry that did not allow for local control on saturation or pore pressure and while useful to demonstrate the changes produced by CO_2 saturation their data cannot be used for QI purposes.

Park et al.[30] from the KIGMR (Korea Institute of Geoscience and Resources) studied the effect of CO_2 saturation in a sandstone sample using ultrasonic laboratory measurements and found more than 6% decrease in the velocity while more reductions were noted on wave amplitudes during the saturation. Purcell et al. [31] did some laboratory measurements on reservoir core samples collected from the SACROC oil field and some other samples (shale and Berea sandstone). The laboratory measurements on monitoring of injected CO_2 movements was conducted at two temperatures (room temperature and 50^0C) with pore pressure ranging from 0 to 30 MPa at different constant confining pressures (30, 40, and 50 MPa). Their results showed large velocity fluctuations with phase changes.

Zemke et al. [32] studied the mechanical effects on sandstone while saturated with brine or supercritical CO_2. Siggins et al. [33] showed the acoustic responses on the brine, gaseous and liquid CO_2 saturated samples from CRC-1 well in the Otway Basin, Australia. Shei et al. [20] showed an extensive study of supercritical CO_2 saturated into brine saturated Tako sandstone through CT (Computer Tomography) methods.

Alemu et al. [34] used CT methods to monitor the CO_2 distribution into brine-saturated outcrop Rothbach sandstone through resistivity and acoustic velocity variations. Nakagawa et al. [35] showed the acoustic measurements on CO_2 saturated Berea sandstone and Tuscaloosa sandstone in seismic frequencies using a resonance bar technique. Lebedev et al. [36] investigated the acoustic responses of supercritical CO_2 saturated rock samples collected from CRC-2 well Otway basin, Australia. They noticed a 7% reduction in P-wave velocities with a increase of CO_2 saturation from 0% to 50%.

All of the studies above have provided interesting insights into the effects of CO_2 on seismic wave speeds. However, none of these have been under carefully controlled conditions of temperature, saturation, and pore and confining pressures and as such are of limited use in the development of rock physics templates useful to seismic interpretation.

To our knowledge, the only such controlled experiments have been carried out in our laboratory at the University of Alberta. Yam and Schmitt [37] presented a comprehensive study on the seismic effects relating with different phase states of CO_2 using ultrasonic measurements on fully CO_2 saturated Berea sandstone at different temperatures and pressures. Yam [4] described her initial tests on highly porous sintered alumina where the influence of the phase transitions of CO_2 are highly apparent in the observed wave speeds. She found, too, that she was able to theoretically predict the observations. Njiekak et al. [38] published an extensive report on the laboratory results on an extensive series of CO_2 saturated carbonates from Weyburn-Midale geologic project in different temperatures and temperatures.

Though a number of works are going on with different CO_2 sequestration projects, work on laboratory experiments involving CO_2 as a lone pore fluid, different phase state effects of CO_2 and pore fluid property changes with pore pressures remain rare. In this thesis work we will investigate these three seismic effects extensively and give an end member (i.e. pure research purpose without including any complication) results to detect any changes happening in the elastic responses of two sandstones saturated with CO_2.

1.5 Chapter description

In this thesis work I have presented a systematic study of P- and S- wave velocities in two types of Fontainebleau samples under in-situ conditions while the samples are fully saturated with CO_2 under the gas, liquid, or supercritical fluid phase states. An end-member approach is described here as the real situation is too complicated to reproduce in the lab environment now.

In chapter 2 I have given the related theoretical background to the conducted in this thesis. A brief description of theory of elasticity, viscoelastic effect on the material's behaviour, and wave propagation through the viscoelastic media were given. Two well-known fluid substitution formulations of Gassmann and Biot were discussed in detail with their assumptions,mathematical formulation, applicability and drawbacks. At the end of the chapter the ultrasonic pulse transmission method was introduced which will be used for our experiment in the later chapters.

Chapter 4 gives details on the experimental set up and the laboratory procedures we have used to obtain the experimental result for this thesis work. We have discussed about the piezoelectric transducer construction, the sample preparation steps, and the detailed experimental protocols and configuration for the measurements. The error analysis associated with the wave velocity measurements are also presented in this chapter.

In chapter 5 the experimental results and the discussion of the different findings of the two Fontainebleau samples were discussed with all related figures. The three fluid saturation cases namely nitrogen saturation, CO_2 saturation and water saturation cases were presented. The wave velocity change and phase transition occurrences were shown with the different pressure, temperature and fluid-type saturations.

Chapter 6 mainly focused on the comparison of our experimental findings and theoretical predictions. Theoretical scenarios for different conditions with pressure, temperature and fluid-type variation were given with color diagrams. Two well known fluid saturation models of Gassmann and Biot predictions were compared with our lab results with their similarities and differences for both types of Fontainebleau sandstone.
In chapter 7 we apply the results of the laboratory measurements to the seismic monitoring over a hypothetical reservoir where CO_2 is coexisting with other in situ fluids such as oil and brine in pore spaces Specifically the changes in the seismic reflectivity of the contact between zones saturated with CO_2 and with water with changing pore pressure are modelled.

With chapter 8 we conclude with an overview of the results, the implications for seismic monitoring, and suggestions for the directions of future research.

Chapter 2

Theoretical Background

Having clear understanding of the seismic wave behaviour with physical changes in the propagating medium and under the temperature and pressure is important to obtaining correct information about the subsurface conditions. Our work here examines the influence of different pore fluids (Nitrogen, CO_2 and H_2O) on the overall wave propagation. In this chapter I will briefly discuss the factors seismic waves in the case of geological CO_2 sequestration. In the beginning, I will give an overview of the basic theoretical concepts of stress and strain followed by the theory of elasticity. Viscoelasticity is also briefly discussed. Then I discuss the effects of pore fluids through the rock physics concept of fluid substitution using two widely used theories of Gassmann and Biot. Finally, the different lab methodologies are mentioned and the pulse transmission technique's fundamental ideas are presented.

2.1 Stress and Strain : Concepts

In rock physics and plate tectonics earth material deformation is a well discussed topic. Depending on factors such as the applied loading and the observed change behaviors, materials may be classified as elastic, plastic, or visco-elastic. To understand deformation behaviour we can start with the mathematical description of stress and strain. Many texts(e.g. Malvern)[39] define the stress with details in a mathematical approach where stress is considered as the limit of a force acting on an infinitesimal area. Here we will try to define it in a less complicated way. Let us consider an infinitesimal cube on which the stress will be applied. We start with the equilibrium state of the system where all the forces acting on that cube surface are in balance (body forces are ignored). In the Figure 2.1. we consider a cube whose surfaces we assume are aligned with a standard Cartesian Coordinate system X,Y and Z.

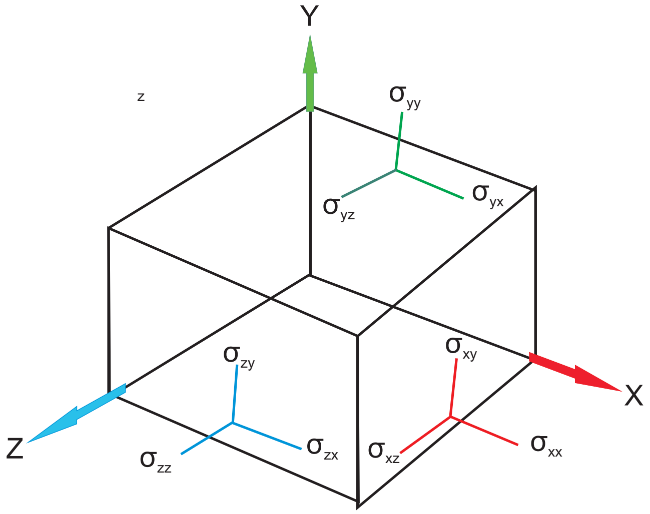

Figure 2.1: axial components of stress vectors.

The three stress tensors σ_{ij}, *(i,j = x,y,z)* are a really averaged force elements acting on the surfaces with the indices i = j indicating the normal to the plane upon which this stress acts. There are two types of stresses:

1. Normal stresses are those in which the stress is applied normal to the surface planes i.e. i=j.

2. Shear stresses are those in which the stress acts long the surfaces along the surfaces i.e. $i \neq j$.

The unit of stress is force by area which is actually the same unit as pressure. The SI unit for stress is the pascal (1 Pa= 1 N/m^2), in geophysics we also use bars (100 kPa) or $dyne/cm^2$ or psi(Ibs/in^2).

To fully describe a body under stress we need 9 stress elements and as such stress is a second order tensor. According to Lay and Wallace [40] the equilibrium condition for the system is:

$$\frac{\partial \sigma_{ij}}{\partial x_{ij}} = 0, \sigma_{ij} = \sigma_{ji}, \textit{i,j=1,2,3}. \tag{2.1}$$

Where *i,j=1,2,3* are same as *i,j=x,y,z* in the Figure 1, respectively.

These applied forces on the material result in lateral and angular distortions in the object. Infinitesimal change, according to Lay and Wallace [40] applies for strains of less than $10^{-5} - 10^{-4}$, and these are considered to be in the elastic range. To understand the deformation of the medium the strain tensor is introduced ϵ_{ij} which is the dimensionless normalized measure of the displacement

$$\epsilon_{ij} = \frac{1}{2}[\frac{\partial u_i}{\partial x_j} + \frac{\partial u_j}{\partial x_i}], \textit{i,j=1,2,3}. \tag{2.2}$$

Here u_i are the components of displacement(here *i=1,2,3* shows the components along x,y,z respectively) of the displacement vector and x_i represents the axes of the Cartesian coordinate system. Strain also is of two kinds-(1) normal strain(deformation in size) and (2) shear strain(deformation in shape). Strains are symmetric i.e. $\epsilon_{ij} = \epsilon_{ji}$ and this results in six independent strain components.

2.2 Theory of Elasticity:

In elastic materials when stress is removed the material's deformation follows along the same path returning to its initial state as just discussed. From Hooke's law's tensor form, the least symmetric triclinic solid needs 21 independent elastic parameters to fully describe its deformation behaviour. With this complexity, Hooke's law that simply relates stress and strain can be written as a 6 X 6 Voigt matrix form as [41, 40, 42]

$$\begin{bmatrix} \sigma_1 \\ \sigma_2 \\ \sigma_3 \\ \sigma_4 \\ \sigma_5 \\ \sigma_6 \end{bmatrix} = \begin{bmatrix} c_{11} & c_{12} & c_{13} & c_{14} & c_{15} & c_{16} \\ c_{21} & c_{22} & c_{23} & c_{24} & c_{25} & c_{26} \\ c_{31} & c_{32} & c_{33} & c_{34} & c_{35} & c_{36} \\ c_{41} & c_{42} & c_{43} & c_{44} & c_{45} & c_{46} \\ c_{51} & c_{52} & c_{53} & c_{54} & c_{55} & c_{56} \\ c_{61} & c_{62} & c_{63} & c_{64} & c_{65} & c_{66} \end{bmatrix} \begin{bmatrix} \epsilon_1 \\ \epsilon_2 \\ \epsilon_3 \\ \epsilon_4 \\ \epsilon_5 \\ \epsilon_6 \end{bmatrix} \tag{2.3}$$

Here σ_i's are the stresses, ϵ_i's are the strains, c_{ij}'s are the elastic stiffness, and $i, j = 1, 2, 3, 4, 5, 6$. The number of independent elastic stiffnesses required depends on the degree of symmetry of the material. It is important to note the definition of the components of strain in the Voigt form of Equation 2.3. The first three ϵ_1, ϵ_2, and ϵ_3 are equal to $\epsilon_{11}, \epsilon_{22}, \epsilon_{33}$ as directly defined in Equation 2.2. However, $\epsilon_4, \epsilon_5, and \epsilon_6$ represent $2\epsilon_{23}, 2\epsilon_{13}$, and $2\epsilon_{12}$, respectively.

An isotropic medium has infinite symmetry and its behaviour is independent of direction; consequently less information is needed to describe it. Only 2 independent elastic constants: c_{11} and c_{44} are enough for its full representation and the structure of the elastic stiffness matrix becomes:

$$c_{ij} = \begin{bmatrix} c_{11} & c_{11} - 2c_{44} & c_{11} - 2c_{44} & 0 & 0 & 0 \\ c_{11} - 2c_{44} & c_{11} & c_{11} - 2c_{44} & 0 & 0 & 0 \\ c_{11} - 2c_{44} & c_{11} - 2c_{44} & c_{11} & 0 & 0 & 0 \\ 0 & 0 & 0 & c_{44} & 0 & 0 \\ 0 & 0 & 0 & 0 & c_{44} & 0 \\ 0 & 0 & 0 & 0 & 0 & c_{44} \end{bmatrix} \tag{2.4}$$

These constants can be connected to the material's bulk modulus, K, and it's shear modulus,μ , or the material's Lame parameters, λ and μ as :

$$c_{11} = K + \frac{4}{3}\mu = \lambda + 2\mu, \tag{2.5}$$

$$c_{44} = \mu. \tag{2.6}$$

Using Hooke's law and equation of motion and strain expressed as displacement we get the scalar one dimension wave equation in elastic material with a displacement, u, as,

$$\rho \frac{\partial^2 u}{\partial t^2} = c\nabla^2 u. \tag{2.7}$$

here u is expressed as a function of time and space, u(x,t), ρ is the bulk density of the elastic medium and c is the elastic stiffness. The wave velocity for the most case governing with above wave equation is

$$V = \sqrt{\frac{c}{\rho}} \tag{2.8}$$

If we consider a homogenous and isotropic medium, there are two types of seismic waves namely a P-wave and an S-wave both of which are also referred as body waves as they travel through interior body of the rock. The velocities related with these two waves can be expressed as

$$V_P = \sqrt{\frac{c_{11}}{\rho}} = \sqrt{\frac{\lambda + 2\mu}{\rho}} = \sqrt{\frac{K + \frac{4}{3}\mu}{\rho}} = \sqrt{\frac{M}{\rho}}, \tag{2.9}$$

$$V_s = \sqrt{\frac{c_{44}}{\rho}} = \sqrt{\frac{\mu}{\rho}}. \tag{2.10}$$

As shear forces are zero in fluids only P-waves are allowed to propagate through fluid with a velocity

$$V_P = \sqrt{\frac{K}{\rho}}, \tag{2.11}$$

where K is the bulk modulus of the medium.

The bulk modulus , K, is defined as the measure of the medium's resistance to uniform compression(stiffness) , and expressed by,

$$K = -\frac{\sigma_0}{\theta}, \tag{2.12}$$

$$\sigma_0 = \frac{\sigma_1 + \sigma_2 + \sigma_3}{3}, \tag{2.13}$$

and

$$\theta = \epsilon_1 + \epsilon_2 + \epsilon_3. \tag{2.14}$$

where σ_0 is the hydrostatic stress and θ is the volumetric strain.$\frac{1}{K}$ is called the compressibility of the material. The shear modulus or modulus of rigidity or Lame's second parameter is defined as the measurement of the material's resistance to shear strain, and expressed by

$$\mu = \frac{\sigma_i}{2\epsilon_i}, i{=}4{,}5{,}6 \tag{2.15}$$

2.3 Viscoelasticity:

So far we have mentioned that there are two types of material deformation that will be discussed: (a) elastic which means when the applied stress is removed the strain can completely recovered and there is no energy loss, and (b) inelastic or viscous behaviour where the energy used to strain the medium is lost to the surroundings and the material become permanently deformed once the applied force is removed. In the case of a viscous fluid the behaviour is expressed by

$$\sigma_{ij} = \eta\frac{\delta\epsilon_{ij}}{\delta t}, i \neq j. \tag{2.16}$$

Here η is called the fluid viscosity. Real materials are often considered as viscoelastic if they display behaviour between that of a purely viscous material and of a purely elastic material. Some special phenomena in viscoelastic material are listed below:

1) Viscoelastic materials display a creep response in which strain increases with time under a constant applied stress: Figure 2.2 shows the creep and recovery of a medium experiencing a step in the applied stress. From the plot we can see that viscoelastic material shows a combined response between a perfectly elastic and a purely viscous material.

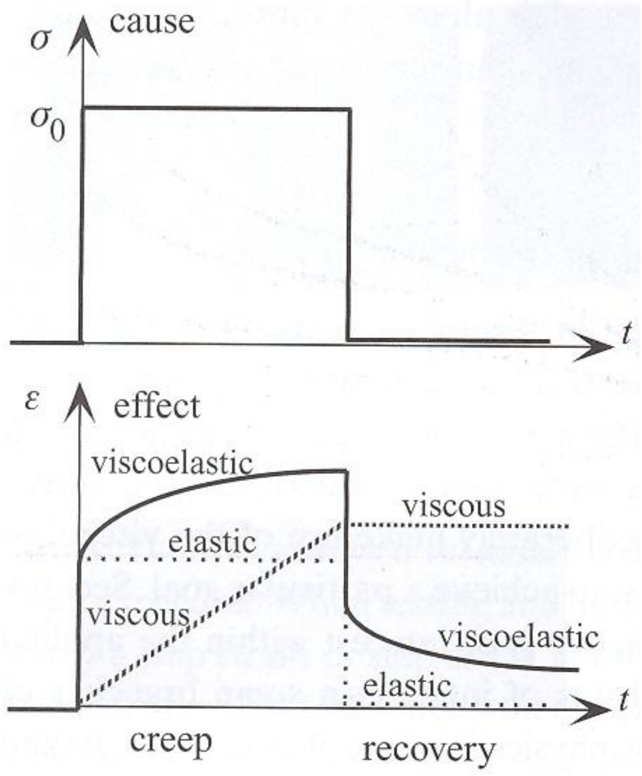

Figure 2.2: Viscoelastic medium's creep and recovery response plot. Original source: Viscoelastic material by Roderic Lakes[3] and Reprinted with the permission of Cambridge University Press.

2) Viscoelastic materials display stress relaxation. In this case the strain remains fixed while the stress decreases, or relaxes, with time Figure 2.3 represents the relaxation and recovery of a medium going through a step strain. As time increases stress must decreases to keep the strain constant.

3) Mechanical energy loss when cyclic stress is applied. If we consider one

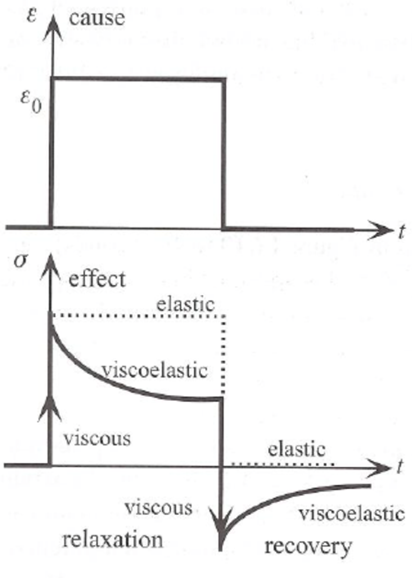

Figure 2.3: Viscoelastic material's relaxation and recovery response plot.Original source: Viscoelastic material by Roderic Lakes[3] and Reprinted with the permission of Cambridge University Press.

dimensional case, an applied stress which changes sinusoidally with time, t, and angular frequency, ω, is expressed as

$$\sigma(t) = \sigma_0 e^{i\omega t}, \tag{2.17}$$

the resulting strain shows a time delay where it varies sinusoidally at the same frequency for a viscoelastic material as:

$$\epsilon(t) = \epsilon_0 e^{i(\omega t - \delta)}. \tag{2.18}$$

This delay in strain to the applied strain results in phase lag. The phase lag δ is defined as

$$\delta = \frac{2\pi \Delta t}{T}. \tag{2.19}$$

Here T is the period for stress and strain variation, and Δt is time delay. δ is also called the loss angle and is the measure of the internal friction and the mechanical damping of a material. It also is sometimes used as the loss tangent where it is $\tan\delta$.

If $\delta = 0$, there is no phase lag between the stress and the strain of a given material, and in this case the medium is an elastic solid. For perfect elastic medium the stiffness constant c is a real number. But in the case of a viscoelastic material due to the phase lag between stress and strain the stiffness constant become a complex number given by

$$\frac{\sigma(t)}{\epsilon(t)} = \frac{\sigma_0}{\epsilon_0} = c^* = c' + ic''. \tag{2.20}$$

Where c' is the real part and is usually known as the storage modulus responsible for the material's elastic response and c" is the imaginary part known as loss modulus which is responsible for the viscous response of the material or the energy loss. When a wave propagates through a viscous medium the storage modulus helps its physical travel while the loss modulus is responsible for the attenuation or disappearance of the wave. Then the loss tangent is given by

$$\tan\delta = \frac{c^{"}}{c'}, \tag{2.21}$$

The physical understanding of the loss tangent is thus the ratio of energy loss to the stored energy.

2.3.1 Mathematical models for linear viscoelastic response

2.3.1.1 The Maxwell spring-dashpot model

We already have discussed that there is a time dependency in viscoelastic response. This can be consider analogous to the time dependency of reactive electric circuit. To give an visualization of molecular motions of these type of systems a 'spring-dashpot' model (Figure 2.4) is considered. Spring implies the response of 'Hookean' spring obeying Hook's law as

$$\sigma = \kappa\epsilon \tag{2.22}$$

where σ, ϵ, and κ are the spring force, displacement and spring constant which are analogous to stress, strain and Young's modulus E. This model gives the instantaneous material bond deformation and the mechanical energy stored reversibly as strain energy is given through its magnitude.

Figure 2.4: Hookean spring (left) and Newtonian dashpot (right)

The 'Newtonian dash-pot' part gives the viscous response of the viscoelastic materials where the stress produces not strain but a rate of strain as

$$\sigma = \eta\frac{d\epsilon}{dt} \tag{2.23}$$

where η is the viscosity.

When these two segments 'Hookean spring' and 'Newtonian dashpot' are connected in series the combination (Figure 2.5) is called 'Maxwell' solid. It implies that the stress on each element is the same as the applied stress, while the sum of the strain on each elements gives the total strain.

$$\sigma = \sigma_s = \sigma_d \tag{2.24}$$

$$\epsilon = \epsilon_s + \epsilon_d \tag{2.25}$$

where the subscripts s and d stands for spring and dashpot, respectively. As

Figure 2.5: The Maxwell viscoelastic model

the system is in series we can write

$$\frac{d\epsilon}{dt} = \frac{d\epsilon_s}{dt} + \frac{d\epsilon_d}{dt} = \frac{1}{\kappa}\frac{d\sigma}{dt} + \frac{\sigma}{\eta} \tag{2.26}$$

introducing τ which is the ratio of viscosity to stiffness we can write

$$\frac{d\sigma}{dt} + \frac{\sigma}{\tau} = \kappa\frac{d\epsilon}{dt} \tag{2.27}$$

This expression is the governing equation of the Maxwell model. Here we are having not just simple stress or strain but the time derivatives of them which introducing more complicated behaviour than the simple Hook's law [43]. One of the limitation of Maxwell model is that does not predict creep properly.

2.3.1.2 The Kelvin or Voigt model

In the Kelvin or Voigt model the Hookean spring and Newtonian dashpot are considered to connected in parallel(Figure 2.6). This model can explain properly the creep behaviour of polymers. The constitutive relation is given as

$$\sigma(t) = E\epsilon(t) + \eta\frac{d\epsilon(t)}{dt}. \tag{2.28}$$

Here E is the Young's modulus. This model gives a solid undergoing reversible, viscoelastic strain. For a constant stress loading the material deforms at a decreasing rate approaching asymptotically to a steady-state strain. The model is good in explaining the creep behaviour of the material but for relax-

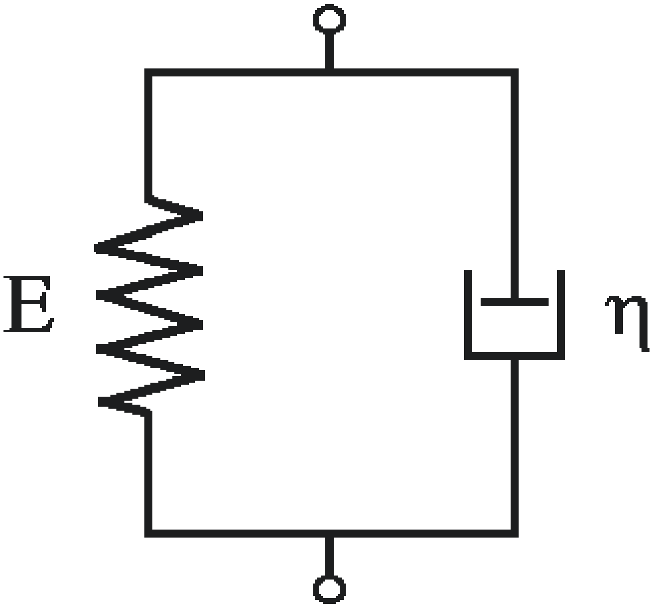

Figure 2.6: The Maxwell viscoelastic model

ation prediction this model is less accurate.

2.4 Wave propagation in viscoelastic media:

When waves propagate through a high viscosity fluid they are referred as viscous waves by Bhatia [41]. Let us consider a transverse harmonic wave propagation in x_1 direction , with particle velocity S_2 in x_2 direction as

$$S_2 = S_2^0 \exp i(\omega t - kx_1), \mathbf{S} = (0, S_2, 0) \tag{2.29}$$

From the Navier-Stokes equation of motion [44] we have:

$$\rho \frac{Du_i}{Dt} = -\rho g \frac{\partial h}{\partial x_i} - \frac{\partial p}{\partial x_i} + \frac{1}{3}\eta \frac{\partial}{\partial x_i}\frac{\partial u_j}{\partial x_j} + \eta \frac{\partial^2 u_j}{\partial x_j \partial x_j}. \tag{2.30}$$

Here $\frac{D}{Dt}$ is the material derivative [39], h is height and g is the acceleration of gravity.

From equation (2.30), the equation of motion for S_2 may be written as

$$\rho\frac{\partial^2 S_2}{\partial t^2} = \eta\frac{\partial}{\partial t}(\frac{\partial^2 S_2}{\partial x_1^2}) \tag{2.31}$$

Substituting (2.29) into (2.31) we get

$$\rho\omega = i\eta k^2 \tag{2.32}$$

where

$$k = k_1 - ik_2. \tag{2.33}$$

From (2.32) we found that $k_1 = k_2 = \sqrt{\frac{\rho\omega}{2\eta}}$. The shear wave velocity is then:

$$V^2 = \frac{\omega^2}{k_1^2} = \frac{2\eta\omega}{\rho}, \tag{2.34}$$

the amplitude attenuation per wavelength(λ) denoted as α:

$$\alpha_\lambda = k_2\lambda = 2\pi(\frac{k_2}{k_1}) = 2\pi \tag{2.35}$$

and with the quality factor is simply Q → 0 showing a high level of over damping. Practically it would be almost impossible to detect the wave. Using reflectivity techniques various groups are trying to measure the shear wave properties of complex fluids such as heavy oils [45].

From the above equation you can note some important things:
1) If viscosity vanishes a shear wave cannot propagate through liquids.
2)Shear velocity increases as the value of viscosity rises.
3)High frequency waves propagate faster than low frequency waves and that indicates a natural dependency between the wave velocity and frequency.

Using the bulk viscosity in compressible fluid, $\zeta = \eta^0 + \frac{2}{3}\eta$, where η is the shear viscosity and putting the Navier-Stokes equation we get:

$$\frac{\partial^2 u_i}{\partial t^2} = \frac{\delta P}{\delta \rho}\frac{\partial}{\partial x_i}(\frac{\partial u_j}{\partial x_j}) + \frac{1}{\rho_0}\frac{\partial}{\partial t}\eta \nabla^2 u_i + (\frac{1}{3}\eta + \zeta)\frac{\partial}{\partial x_i}(\frac{\partial u_j}{\partial x_j}). \tag{2.36}$$

With the introduction of the bulk viscosity ζ , the equation includes the volumetric change due to attenuation and we get a Navier-Stokes equation for the compressible fluids case.

When considering viscosities in the compressible fluid version of wave equation and a harmonic plane wave solution $e^{i(\omega t - kx)}$, an attenuation-desperation relation can be established with a reference frequency ω_ν [41] :

$$\omega_\nu = \frac{K_s}{\zeta + \frac{4}{3}\eta}, \tag{2.37}$$

where K_s is adiabatic the bulk modulus under isentropic conditions (i.e., the entropy of the system remains constant).

The phase velocity and attenuation coefficient can be derived as:

$$v^2(\omega) = \frac{2K_s}{\rho}\frac{1 + (\frac{\omega}{\omega_\nu})^2}{1 + \sqrt{1 + (\frac{\omega}{\omega_\nu})^2}}, \tag{2.38}$$

$$\alpha_\lambda(\omega) = \frac{\rho\pi}{K_s}\frac{\frac{\omega}{\omega_\nu}}{1 + (\frac{\omega}{\omega_\nu})^2}\nu^2, \tag{2.39}$$

here ρ is the medium density without any wave presence and ω_ν is the reference frequency. These equations are known as Bhatia's attenuation and dispersion relations.

2.5 Rock Physics and Viscoelastic and Poroelastic Theories:

Earth materials and normal rocks usually contain pores; they are made up of a solid matrix (mineral grain) and a void volume that may contain fluid inside. Consequently when we consider wave propagation through a real rock we need to consider the influence of both the solid matrix and the pore fluid residing inside the void space. To understand these properties one needs to know how the system responds when the seismic waves physically induce particle motions of the fluid and solid as the wave passes. The characteristics that are important in this case are the compressibilities of the solid minerals, the rock frame, and the pore fluid; the rigidities of the solid minerals and the rock frame, the porosity, and the mass density of the rock. Here we will discuss some of the theoretical rock-fluid interaction models: the 'static' Gassmann's formula and the frequency dependent Biot formulation that allow us to predict the elastic properties of the fluid saturated rock that are necessary to determine seismic wave speeds.

2.5.1 Gassmann's equation:

Gassmann's equation is simple and widely used in applied geophysics to calculate the bulk and shear moduli of a fluid saturated porous rock. However, it is strictly only applicable under static conditions (i.e. zero frequency) but it is commonly assumed that it can be used the seismic frequency region $\sim 100Hz$. Gassmann considered the elementary elasticity of the pore fluid and mineral grains of the sample which is saturated. The assumptions are:

1) The material is microscopically homogeneous and isotropic,

2) All minerals that constitute the rock sample have similar bulk and shear moduli,

3) The fluid is inviscid and is allowed to freely move through the interconnected pore network,

4) The pore space is completely saturated with the fluid at all times,

5) There are no chemical interactions between the pore fluid and the solid minerals, i.e. the rock's frame is not changed by the fluids,

6) Quasi-static conditions are maintained.

In this Gassmann's formulation the medium's saturated bulk modulus depends on a number of factors that include the rock's frame modulus, K_{dry}, the bulk moduli of the mineral grains, K_s; the bulk modulus of the fluid K_f, and the porosity of the rock medium, ϕ through the following:

$$\frac{K_{sat}}{K_s - K_{sat}} = \frac{K_{dry}}{K_s - K_{dry}} + \frac{K_f}{\phi(K_S - K_f)}, \tag{2.40}$$

that after some algebraic steps we get the saturated bulk modulus as:

$$K_{sat} = K_{dry} + \frac{(1 - \frac{K_{dry}}{K_s})^2}{\frac{\phi}{K_f} + \frac{1-\phi}{K_s} + \frac{K_{dry}}{K_s^2}}. \tag{2.41}$$

The saturated shear modulus μ_{sat} is assumed to remain the same as the dry shear modulus i.e. $\mu_{sat} = \mu_{dry}$.

By measuring the saturated bulk or shear moduli we can in principle calculate the saturated P- or S-wave velocities using Equations (2.7) and (2.8). The bulk density of the rock in this case can be written as

$$\rho_{sat} = (1 - \phi)\rho_s + \phi\rho_f. \tag{2.42}$$

where ρ_s is the mineral (or solid) density and ρ_f is the fluid density. Now in order to know K_{sat}, we need 1) the bulk modulus of the mineral K_s, 2) bulk modulus of the pore fluid K_f, 3) the bulk modulus of the frame K_{dry}, and 4) the porosity ϕ of the rock. The determination of the moduli are described below.

2.5.1.1 The bulk modulus of the mineral grain

The mineral grain means the minerals that make up the solid component. We need to know the mineralogy of in the rock to determine its grain modulus, K_s. If the medium is made up of more than one dominant mineral then we must determine the volume fraction of each of the various mineral constituents. By using microscopic imaging we can determined the type of the mineral and volume fractions. Using Hill's average [46], if we know about the mineral composition, the bulk modulus can be calculated as:

$$K_s = \frac{1}{2}(K_V + K_R), \tag{2.43}$$

here K_V is the Voigt's average (upper bound on the effective elastic modulus M), K_V, [47] and K_R is Reuss (lower bound on the effective elastic modulus M)' average [48]. The two extreme values for the modulus are given by the following the averages for a mixture:

$$K_V = \sum_{i=1}^{n} \phi_i K_i, \tag{2.44}$$

$$\frac{1}{K_R} = \sum_{i=1}^{n} \frac{\phi_i}{K_i}. \tag{2.45}$$

Here ϕ_i gives the volume fraction value of the i^{th} mineral, and K_i gives the bulk modulus of the corresponding mineral.

In the lab the modulus can be determined without having the information about the exact mineral composition of the rock matrix using Biot and Willis' [49] unjacketed test if there is no occluded pores in the sample. In this method the rock is fully saturated with a fluid and then placed in a pressure vessel without sealing. The change in the sample volume after equilibrium of pressure between the inside and the outside of the rock is obtained. This type of tests were done by Bakorji [50] on carbonate rocks and Schmitt and Zoback [51] using low porosity metamorphic gneiss..

2.5.1.2 Pore fluid elastic moduli determination

The pore fluid means the fluid in void space of the sample the fluid can be of hydrocarbon, of water, of CO_2, of a fluid mixture or even of a vacuum. These fluids can be in gaseous, liquid, or supercritical phases as will be seen in later chapters. If the fluid density, ρ_f, and the speed of sound through the pore fluid, V_{Pf} are known we can easily find the modulus using equation(2.11):

$$K_f = \rho_f V_{Pf}^2. \tag{2.46}$$

Unfortunately usually one does not have access to the fluid directly and one must estimate the fluid bulk modulus. It is usually assumed that Wood's formula adequately describes this (Equation 2.47). If the pore space is filled with a mixture of n fluids, the bulk modulus K_f of the fluid mixture is given by Woods formula [52]

$$\frac{1}{K_f} = \sum_{i=1}^{n} \frac{x_i}{K_i} \tag{2.47}$$

where x_i and K_i are the volume fractions and bulk moduli of the individual fluid phases, respectively.

Here, however, we are concerned with only a single CO_2 phase and in this case we must also consider the effects of phase, temperature, and pressure. For the fluid mixture Voigt's or Reuss' average formula is used to find out the overall pore fluid modulus. The overall fluid density if we consider a mixture of immiscible fluids is given by

$$\rho_f = \sum_{i=1}^{n} x_i \rho_{xi}. \tag{2.48}$$

2.5.1.3 Dry frame moduli determination:

The frame means here the solid rock sample with empty void space or pores. If we are able to measure the saturated bulk modulus K_{sat} by, for example well log values of density, porosity, and P- and S-wave speeds and with knowledge of the mineralogy and fluid content we are then able to estimate an is situ value of K_{dry} by rearranging the Gassmann's equation as:

$$K_{dry} = \frac{K_{sat}(\phi \frac{K_s}{K_f} + 1 - \phi) - K_s}{\phi \frac{K_s}{K_f} + \frac{K_{sat}}{K_s - 1 - \phi}}. \tag{2.49}$$

There are also theoretical and empirical relations to estimate the dry frame modulus such as:
1) The semi-theoretical expression:

$$K_{dry} = K_s(1 - \beta). \tag{2.50}$$

as given by Bourbie [53] and Mavko et al [54]]. Here β is called the Biot's coefficient defined as the fraction of the pore volume change to the bulk rock volume under unchanged pore pressure.
2) Nur's [55] critical porosity expression: Using the critical porosity term,ϕ_c the dry bulk and shear moduli are estimated as:

$$K_{dry} = K_s(1 - \frac{\phi}{\phi_c}), \tag{2.51}$$

$$\mu_{dry} = \mu_s(1 - \frac{\phi}{\phi_c}) \tag{2.52}$$

3)For porosity $0 < \phi < 0.3$ Geertsma[56] made an empirical relation for determination for dry modulus as:

$$\frac{1}{K_{dry}} = \frac{1}{K_s}(1 + 50\phi), \tag{2.53}$$

In the laboratory measurements here we obtain K_{dry} from the ultrasonic P-wave and S-wave velocities through dry rock is measured to find the dry modulus with the following equation:

$$K_{dry} = \rho(V_P^2 - \frac{4}{3}V_s^2) \tag{2.54}$$

$$\mu_{dry} = \rho V_s^2. \tag{2.55}$$

2.5.1.4 Limitation of Gassmann's theory

Gassmann's equation only works in the low frequency range (seismic frequencies). It also has problem in estimating the observed quantities when rock shows to have low aspect ratio pores, or highly viscous pore fluid is present in the frame [57]. For higher frequency data as the laboratory data ($\sim MHz$) the Biot formula is the best choice [54]

2.5.2 Biot's Formula

Biot's formulation is a good approach to find the frequency-dependence of wave velocities for rocks that are saturated with fluid, particularly rocks with highly open pore structures and relatively high porosity. Biot published the theory for wave travel through fluid saturated porous solid in both the high frequency range [58] and low frequency range [59]. As frequency approaches zero, Biot's equation is identical to Gassmann's equation, this duality is often referred to the Biot-Gassmann equation although authors are often not clear if they are referring to the use of the Gassmann expression direction or applying the full Biot theory. In the case for the high frequency limit the theory is valid until the grain scattering is influential and the rock become inhomogeneous. Biot's theory too has problems in rocks that contain mainy microcracks. The assumptions of the formula are that:

1) The rock is microscopically homogeneous and isotropic,

2) The bulk and shear moduli for all rock minerals are similar,

3) The fluid is allowed to move freely through the interconnected pores,

4) The pore space is always completely saturated,

5) The pore fluid has Newtonian rheology , and

6) No chemical reactions occur between the pore fluids and the rock minerals.

Biot included the frequency dependence of wave characteristics through viscous and inertial interactions in between the solid matrix and pore fluid of the rock. In the case of low frequency the rate of the oscillating stress of the propagating seismic waves is slow enough so that the pore fluid is able to be at nearly constant pressure and to be in the equilibrium with the solid matrix. The good coupling between the pore fluid and the pore wall results in almost zero relative differential motion. The viscosity of the pore fluid is the main factor in this case; so in the low frequency case viscosity (internal resistance of the fluid flow) dominates.

On the contrary for the case of high frequencies, the high rate of the oscillating stress of the seismic wave does not allow sufficient time for the pore fluid to adjust; the fluid resists the quick change from its current state of motion. Therefore, in at sufficiently high frequencies the fluid inertia dominates the behaviour.

In the high frequency regime the pore fluid and the solid minerals are no longer coupled and some relative motion between them occurs. Consequently, at high frequencies the saturated rock is stiffer than at lower frequencies. Additionally the relative motion results between the pore wall and pore fluid will produce greater wave attenuation. The variation in the stiffness between the high and low frequencies is called modulus dispersion.

Biot suggested that the transition from low to high frequency behavior occured at a critical frequency f_c defined as:

$$f_c = \frac{\phi\eta}{2\pi\rho_f\kappa} \tag{2.56}$$

where η is the pore fluid viscosity and κ represents the absolute permeability of the medium.

If the propagating wave has a frequency, $f << f_c$, the it is consider at low frequency range and for high frequency range the frequency should be $f >> f_c$.

The relative motion between the solid and the pore fluid gives rise to three types of different body waves inside a porous material : one shear wave and two compressional waves named the 'fast' P-wave and 'slow' P-wave. If the pore fluid and the rock frame are in phase it produces 'fast' P-wave. Otherwise, the slow P wave consists of a differential motion between the solid and the pore fluid. In the laboratory and in the field we can easily identified the 'fast' P-wave. On the other hand the 'slow' P-wave is so much attenuating that it is only detected in the laboratory [60, 61].

We take the rock to be saturated with a single fluid and a wave is propagating through the medium. We assume that the total force is due to stress acting on the solid part and the pore fluid. The other things we also consider are:
1) Taking account the potential energy effects to get the stress-strain relations;
2) The solid's kinetic energy, the fluid's kinetic energy and mass induced from the solid-fluid coupling;
and
3) The dissipation function.
Considering all these we have a general wave equations of motion with the displacement vectors $\overrightarrow{u_s}$ for solid and $\overrightarrow{u_f}$ for fluid as (Bouzidi [62]):

$$(1-\phi)\rho_s\frac{\partial^2}{\partial t^2}\overrightarrow{u_s}-\rho_{12}\frac{\partial^2}{\partial t^2}(\overrightarrow{u_s}-\overrightarrow{u_f})+F(\omega)\frac{\eta\phi^2}{\kappa}\frac{\partial}{\partial t}(\overrightarrow{u_s}-\overrightarrow{u_f})$$
$$=\mu_{dry}\nabla^2\overrightarrow{u_s}+(A+\mu_{dry})\overrightarrow{\nabla}\overrightarrow{\nabla}(\overline{\nabla}.\overrightarrow{u_s})+Q\overrightarrow{\nabla}(\overrightarrow{\nabla}.\overrightarrow{u_f}), \quad (2.57)$$

$$\phi\rho_f\frac{\partial^2}{\partial t^2}\overrightarrow{u_f}+\rho_{12}\frac{\partial^2}{\partial t^2}(\overrightarrow{u_s}-\overrightarrow{u_f})-F(\omega)\frac{\eta\phi^2}{\kappa}\frac{\partial}{\partial t}(\overrightarrow{u_s}-\overrightarrow{u_f})=Q\overrightarrow{\nabla}(\overrightarrow{\nabla}.\overrightarrow{u_s})+R\overrightarrow{\nabla}(\overrightarrow{\nabla}.\overrightarrow{u_f}), \quad (2.58)$$

where, ρ_{12} is the coupling mass density, $F(\omega)$ is correction factor for viscosity depending on frequency, ω, and A,Q, and R are the Biot parameters with

$$\rho_{12}=(1-\alpha)\phi\rho_f, \quad (2.59)$$

where α is called the tortuosity that accounts for complexity of the pore network

$$F(\omega)=\frac{1}{4}(\frac{\xi T(\xi)}{1+2i\frac{T(\xi)}{\xi}}), \quad (2.60)$$

where ξ is given by

$$\xi=(\frac{\omega g^2\rho_f}{\eta})^{1/2}, \quad (2.61)$$

and $T(\xi)$ is given by

$$T(\xi)=\frac{ber'(\xi)+ibei'(xi)}{ber(xi)+ibei(\xi)}=\frac{e^{i\frac{3\pi}{4}}J_1(\xi e^{-i\frac{\pi}{4}})}{J_0(\xi e^{-i\frac{\pi}{4}})}. \quad (2.62)$$

where g is a pore-size parameter which is a characteristic dimension and the geometry of the pore space. The *ber* and *bei* represent the real and imaginary parts of the Kelvin function and ' indicates the first derivative with respect to ξ. J_0 and J_1 gives the Bessel functions of 0^{th} and 1^{th} order respectively.

Biot's paramaters are given by:

$$A = \frac{(K_s - K_s\phi - K_{dry})^2}{K_s + \gamma K_s^2 - K_{dry}} + K_{dry} - \frac{2}{3}\mu_{dry}, \tag{2.63}$$

$$Q = \frac{\phi K_s(K_s - K_s\phi - K_{dry})}{K_s + \gamma K_s^2 - K_{dry}}, \tag{2.64}$$

$$R = \frac{\phi^2 K_{dry}^2}{K_s + \gamma K_s^2 - K_{dry}}, \tag{2.65}$$

where γ is known as the fluid content coefficient and given by

$$\gamma = \phi(\frac{1}{K_f} - \frac{1}{K_s}). \tag{2.66}$$

The parameters $K_s, K_f, K_{dry}, \mu_{dry}, \phi$, and ρ_f are the same as Gassmann's equation parameters. They can be determined as it mentioned before. Biot's formula requires permeability, κ, tortuosity, α, of the porous medium, and viscosity, η, of the porous fluid in addition.

2.6 Laboratory Methods to measure the elastic wave velocity and attenuation:

Several laboratory methods can be used to determine out the elastic properties of rock sample including:
1) Stress-strain curves [63, 64, 50],
2) Forced oscillation/resonant bar e.g. [65, 66, 67, 68, 35],
3) Pulse-echo [69, 70, 71], and
4) Pulse transmission.
The pulse transmission method is the most used method so far in the case of CO_2 sequestration analysis in the laboratory.

2.6.1 The pulse transmission method

In the pulse transmission method the sample is placed between a source and receiver which are usually piezoelectric ceramic transducers. As the source is excited it produces an ultrasonic pulse with a resonant frequency of 1 MHz that traverses through the sample. The receiver detects the arrival of the wave and records the full ultrasonic waveform which after appropriate corrections gives the time required for the wave to travel. If the length of the sample is known we can easily determine the velocity of the ultrasonic wave using the traverse time and length of the sample.

There are two types of wave velocities:phase velocities and group velocities. Phase velocity is defined as:

$$V_{phase} = \frac{\omega}{k} \tag{2.67}$$

where ω is the angular frequency and k is the wave number. The group velocity is that of the envelope of a wave packet propagating through space with different frequencies and phase velocities, and defined as,

$$V_{group} = \frac{d\omega}{dk}. \tag{2.68}$$

For a non-attenuating system the two velocities are same but in reality most of mediums are attenuating. In this transmission method we used the method proposed by Molyneux and Schmitt[72] to determine the first arrival of a signal through picking the signal's first extremum.

2.7 Summary

To have an idea about the seismic wave behaviors during the geological CO_2 sequestration we have reviewed the different influential factors of subsurface wave propagation. At first, the theory of elasticity was developed to get clear understanding of the elastic behavior of the wave travelling through the samples.

Rock physics was discussed with two fluid substitution models of Gassmann (1951) and Biot (1956b). Biot's formulation is comparatively more complicated to apply then Gassmann's equation, though Gassmann's formulation is restricted to only low frequency applications. Biot's model considers a wide range of frequencies and also includes the wave attenuation.

At the end of the chapter the basic understanding of the ultrasonic pulse transmission method was given with the mentioning of the first arrival picking method we used in this work.

Chapter 3

Experimental set-up, protocol, and error analysis

This chapter focusses on our experimental methods including the preparation of the sample, the protocol used for the experiments, and the analysis of errors.

3.1 Ultrasonic pulse transmission method

In this thesis we determine the wave velocities of CO_2 saturated samples using the ultrasonic pulse transmission method. Conceptually the method is quite simple. We measure the travel time required for the ultrasonic waves to traverse the known length of the sample and with this information simply calculate the P- and S-wave velocities. These velocities are what we can measure, but they in turn give us an idea about the dynamic elastic properties of the sample. For using the ultrasonic method we need a measurement system with several functional units that include source/receiver transducers, signal recording, and data displaying devices. PZT (Piezoelectric Transducers) provide the active source and receiver components and they are placed on the two ends of the sample. The source transducer generates high frequency ultrasonic waves once it is subject to a fast-rising high voltage electrical pulse. The resulting mechanical wave travels through the sample where it is received by the second PZT and transduced to a voltage that represents the waveform. This signal is digitally recorded and finally displayed on the digital oscilloscope and transferred to a computer for further analysis.

3.1.1 Ultrasonic Transducers

In the ultrasonic pulse transmission method the source and the receiver PZTs are the primary components. Aluminum buffer caps, P- and S-wave piezoelectric ceramics, copper foil electrodes and damping materials are the main parts of our ultrasonic transducers. These are manufactured in our laboratory.

A piezoelectric material displays a special behaviour when subject to a mechanical force (and hence a change in the length due to elastic deformation): it becomes electrically polarized with a voltage difference generated across the polarization direction. Conversely, application of a voltage across the material results in a change in the length; and this response is called the inverse piezoelectric effect. Piezoelectric materials' crystal structure does not have any centre of symmetry [73] and hence deformations result in polarization and *vice-versa* .

The PZT ceramic material used in the construction of our transducers is lead zirconate titanate ($Pb[Zr_xTi_{1-x}]O_3$). These ceramics are commercially provided as small ceramic plates, the thickness of which gives resonant frequencies centered of 1 MHz. Our ceramics were manufactured by APC International, Ltd. For source PZT the inverse piezoelectric phenomenon is used where P-waves are generated through producing axial polarization that compress/expand axially and S-waves are generated through lateral polarization that allow shear motion to occur. For the receivers, the converse corresponding piezoelectric behavior provides the ultrasonic wave displacement sensitive voltage that when recorded is the waveform.

Here, we stack the P and the S-wave piezoelectric ceramics on top of one another. This allows the area of the ceramic to be maximized as much as possible, this is important to allow for a stronger signal. This also allows for nearly simultaneous P- and S-wave measurements [74]. The different vibration mode ceramics were mounted on the polished and flattened surface of aluminum cylinder that we refer to as the transducer buffer. The square S-wave piezoelectric ceramic was first mounted followed by the circular P-wave piezoelectric ceramic. The two are separated by a common electrode of copper foil. Highly conductive silver epoxy is used to glue the components together. For the P-wave ceramic this foil works as a negative terminal while for S-wave ceramics it acts as the positive terminal. During construction, any excess epoxy had to be removed from the edges of the ceramics in order to avoid any short-circuiting. Insulated electrical wires were then soldered to the short extended copper foils of the stacked ceramics. We allow the stack to dry up for 24 hours then a small film of non-conductive general epoxy was applied to seal the apparatus.

The final component to the transducer is mechanical damping. This is necessary to stop, as quickly as possible, the resonant ringing of the piezoelectric ceramic with the goal of having a shorter (in time) waveform. The dampling material is a mixture of urethane rubber (Flexane®80 Liquid epoxy, ITW Devcon) and tungsten metal powder. The idea behind this is to have a material that has as high an elastic impedance as possible to match the impedance of the piezoelectric ceramics and to further allow for the waves entering it to be absorbed (so they cannot reverberate to cause further complications to the waveforms). This mixture can nearly be poured and during construction it was placed in a mold to ensure that it fully covered the end of the buffer containing the piezoelectric ceramics. Experience has also taught us that this mixture seals the ceramics further from the high pressure fluids in the pressure vessel and helps to ensure that the final transducer can be reused many times. The transducer is then left alone for at least 7 days to allow for the buffer mixture to fully cure prior to use. The diameter of these final transducer buffers is 3.51

cm in order to match the dimensions of our cylindrical samples.

Another key aspect of the buffers is that they must allow the pore fluids to communicate with the pore space of the rock. For pore pressure control and sample saturation, a pore fluid inlet was included on the top of one transducer end cap. The final geometry and a photograph of the transducer buffers are shown in Figure 3.1.

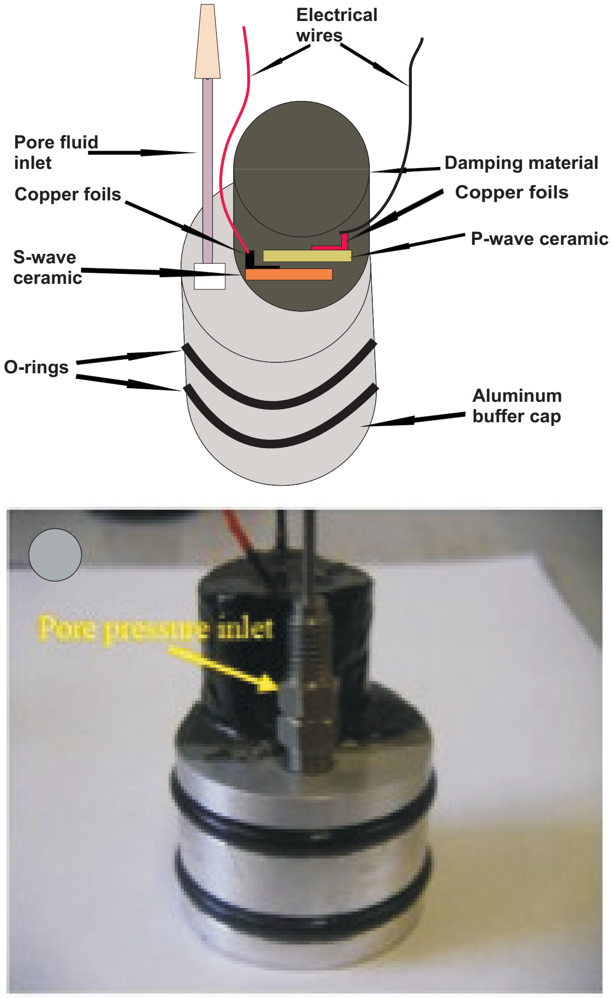

Figure 3.1: (Left) Cartoon showing the different components in a ultrasonic transducer. (right) A picture of a complete transducer with the pore pressure inlet.

3.2 Experimental set-up

The experimental set up we used in our measurements consists of several functional units including a pressure vessel, a pore fluid source, mechanical and electronic pressure gauges, a thermocouple, an electrical resistance tape heater, a pulse generator and a digital oscilloscope. A simplified schematic diagram is shown in Figure 3.2.

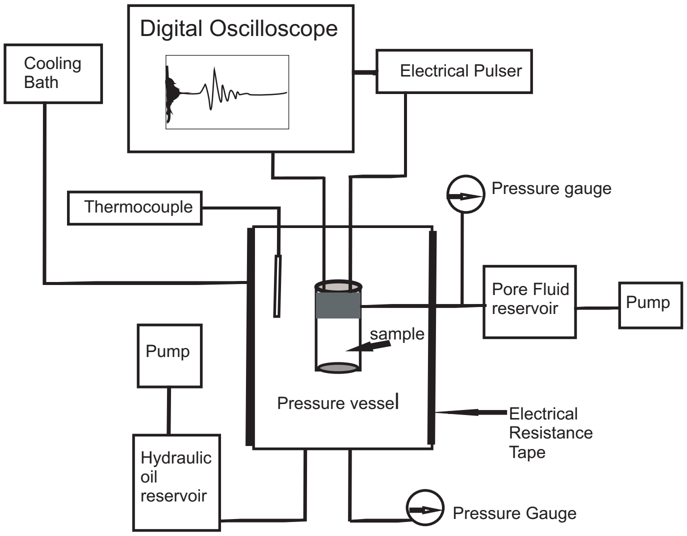

Figure 3.2: Schematic diagram for the experimental apparatus.

The pressure vessel is a heavy steel cylinder containing a cylindrical cavity with a diameter of 10 cm and a depth of 10 cm. This pressure vessel provides a confining or total pressure to the sample to simulate the in-situ overburden and tectonic stresses. A stainless steel tube is used to let pore fluid enter to the sample through the pore fluid inlet of the end cap. The reservoir for the pore fluid (whether it be vacuum, N_2, CO_2, or H_2O) is located near the vessel and connected through high pressure tubing through the pressure vessel cap. The confining and pore pressure systems function independently of one another; thus we can set different confining and pore pressure using the corresponding pumps. A QuizixTM Q5000 pump system is used to control these pressures. However, the Quizix pumps are limited to only a maximum of 68.9 MPa. Up to 200 MPa confining pressure is possible to if a separate air pump is instead connected with the pressure vessel. An electrical resistance tape is wrapped around the pressure vessel's outer wall to allow the temperature of the vessel to be raised from ambient to that desired. A K-type thermocouple (can measure temperature from 200 ^{0}C to +1250 ^{0}C) is located in the pressures vessel and near where the sample will be placed. A refrigerator bath circulator NESLAB RTE 8DD is used to control the rate of temperature raising and cooling more efficiently. It allows us to cool down below room temperature. The temperature range is 30 ^{0}C to + 100 ^{0}C. We use this refrigerator to assist in the cooling of the samples. The receiver and source transducers are connected to the electrical feed of the vessel system by soldering with the transducer wires. The inlet of the end cap is also joined with a stainless steel tube which allows pore fluid to saturate the sample.

A JSR-PR35 pulse generator is used to trigger the transmitting transducer to a quick rise of 200 V square wave and produce the transmitted signal. A digital oscilloscope used to record the traversing signal that has a sample rate of 10 ns. For noise reduction the received waveform is stacked over 500 traces and then recorded. A switchbox is used to switch from P-wave and S-wave at a given conditions.

3.3 Sample preparation

Two Fontainebleau samples were used in our ultrasonic pulse transmission measurements. Both of the samples have 3.50 cm diameters when cored with the drill bit. The 1st sample (Franc type) was little bit shorter than the second, sample 1 was 4.65 cm in length while the sample 2 (Vif type) was 6.10 cm long. The porosities of these samples were 6.28% and 12.5% as determined by using mercury porosimeter (details in chapter 4), respectively. To obtain parallel end surfaces we first used a wet saw then a wet surface grinder. The parallelism of both end faces was checked with a dial gauge where the acceptable range was kept within 1/2000 th of an inch (within 0.025 mm). This check is necessary as the smooth and parallel end faces increase the signal transmission strength and also minimizes the velocity measurements inaccuracy.

Both samples were dried in a oven at 70 ^0C temperature under a vacuum at least 24 hours before the measurements started.The sample was then ready for assembling together with the transducers. The sample is first pushed into flexible Tygon®tube of 3.5 cm internal diameter cut to an appropriate length such that the transducers too can later be inserted at each end. The two ends of this tube were smoothed with a sharp blade. The tube was then immersed under hot water, this heating allowed the tube to expand and made it easier to insert the sample. The sample and both of the end-cap transducers were then pushed into the tube after drying it. Care was made to ensure that the transducers were appropriately aligned so as not to introduce any additional errors to the travel-time. This was particularly important for the S-wave ceramics that are highly directional and whose polarizations must be well aligned with one another across the sample.

We used two rubber O-rings, one around the Al buffers and another underneath the tube, to further prevent hydraulic oil contamination in the sample and also prevent any seeping in between the ultrasonic transducers. For further precautions, two metal clamps were placed just above the rubber O-rings that are nearer to the samples, and were tightened to seal against the O-rings. The sample and assembly were then ready for measurements

3.4 Experimental procedure

As noted from the theoretical sections, we need to measure a variety of differing moduli. To do this we carry through a series of measurements with the pore space first subject to vacuum, then saturated with N_2 gas, CO_2 under gas, liquid, and supercritical phases, and finally liquid H_2O. The behavior of most rocks are highly pressure dependent and because of this we must also carefully consider what combination of confining P_c and pore P_p. The confining pressure is the external pressure applied to the sample's surface, it is comparable to the overburden and tectonic stresses that rock in situ is subject to. The pore pressure is the fluid pressure in the pore space itself. The grains of sample are pushed together by confining pressure while pore pressure acts contrarily to push the grains apart. The resultant of the difference between these two pressures is defined as the differential pressure or the effective pressure, P_d, as

$$P_d = P_c - P_p, \tag{3.1}$$

Where P_c is denoted for confining pressure and P_p is the pore pressure. Generally $P_c < P_p$ in-situ as otherwise the condition $P_p > P_c$ would result hydraulic fracture in the rock mass.

3.4.1 Experimental Protocols

A detailed flow chart depicting our experimental procedure is shown in Figure 2.3. The arrows indicate the sequences of tasks in our experiment.

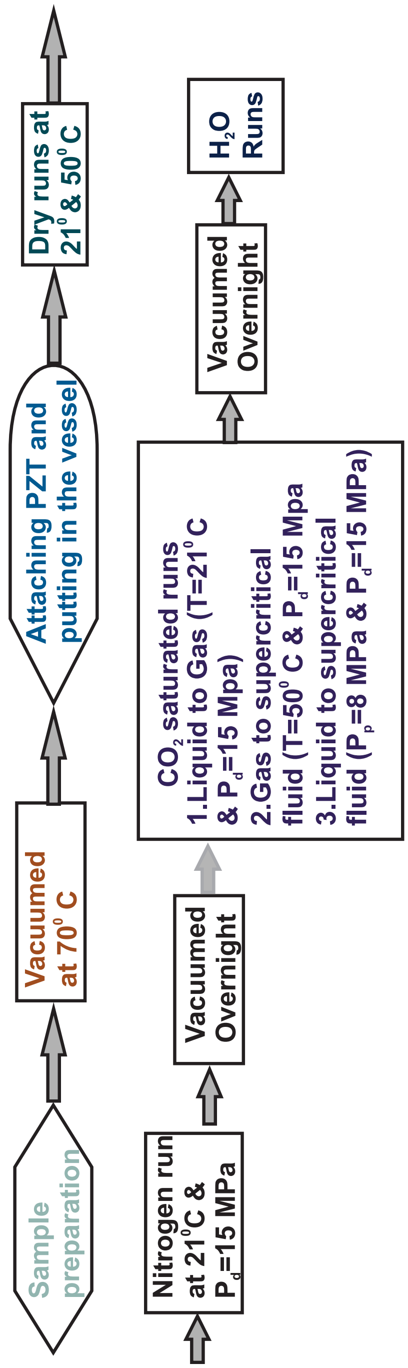

Figure 3.3: Experimental protocol.

3.4.2 Dry measurements

The first suite of P- and S-wave measurements are carried out on a completely dry sample with no fluid within the pore spaces but with the sample subject to varying confining pressures and temperatures. This data is collected in order to be able to determine the dry, or drained, frame modulus K_{dry} (see Chapter 2 on the theoretical background) which is prerequisite to being able to predict the values of the wave speeds. In this set the samples' pore spaces are empty and P_p should be zero. This is accomplished after placing the sample in the pressure vessel by evacuating the pore space with a vacuum pump for at least 12 hours. The pressure drop by the vacuum follows an exponential curve with a rapid drop during the initial hours and become steadily change to lower pressure at later times. Last several hours the vacuum shows a constant pressure drop. At the beginning the pressure showing a pressure of about 101.3 KPa while after 12 hours it become 0.0024 KPa which is only 0.002% of the original atmospheric pressure. Though the pore pressure is zero after the 12 hour vacuum, the pores in sample are essentially empty for the experiments. This is because the mass and the gaseous compressibility are negligible to account.

As temperature is also expected to influence the frame properties, the suites of measurements are repeated at the ambient room temperature and at 50 ^0C. In both cases we change the confining pressure from 1 MPa to 55 MPa; at low pressures where the waves speeds change most rapidly the pressure increments are small (∼2 MPa) but these are adjusted to larger increments at higher pressures. Several dry runs were cycled up and down in pressure 4 times in order to achieve consistency of the results, this is referred to as seasoning the sample in order to ensure the results are repeatable as possible. Consequently, the moduli obtained from the observe wave speeds from the last cycle are the ones used for later theoretical predictions. For the high temperature measurements we allow the sample to heat-up around 2-3 hours and during this time temperature increases. In the experimental set-up control panel there is an option to set up to a fixed temperature.

3.4.3 Nitrogen saturated measurements

The second set of measurements on each sample was carried with nitrogen in the pore space. This suite has two purposes: i) to test the validity of the effective pressure assumption, and ii) to make measurements using a fluid that remains as a gas over the entire range of pressures. Nitrogen is mostly an inert gas at standard conditions. Its triple point is at $T = 210^0C$ and P = 12.53 kPa. The critical point is at P=3.3978 MPa and T = -146.96 ^0C; this means that N_2 is in the supercritical regime in these measurements and does not undergo any phase transformation. Using NIST webBook [75] for constant room temperature (T = 21 ^0C) we see the sound velocity is a linear function of pressure. For our measurements we want to see if our ultrasonic wave velocities (P-wave and S-wave) also show this with the variation of pore pressure. In the tests we maintain an effective pressure of 15 MPa while increasing the pore pressure from 1 to 12 MPa. A pressurizing cycle and de-pressurizing cycle were also done to see some velocity hysteresis due to opening and closing of pores and microcrakes of the sample. After the nitrogen measurements were completed we again evacuated the pore space overnight to remove all of the nitrogen from the sample and made it ready for the CO_2 saturated runs.

3.4.4 CO_2 saturated Measurements

These are the key measurements of the project and are intended to provide information that could be useful for seismic monitoring of CO_2 saturated reservoirs. A series of CO_2 runs were carried out in to see the effect of the transformation of the CO_2 on the P- and S-waves speeds in the sample. After evacuation, the sample is then saturated with CO_2 for more than 3 hours at 20

MPa pore pressure and 35 MPa confining pressure maintaining a differential pressure of 15 MPa. Maintaining this constant differential pressure is important as it means that the properties of the frame should remain essentially constant leaving any variations in the observed wave speeds to be dependent on the pore fluid. From our experimental set up it is almost impossible to ensure that the sample is 100% saturated with the fluid during this time. When we put our sample in these conditions ($P_p = 20$ MPa, $P_c = 35$ MPa and $P_d = 15$ MPa)we noticed an unstable pore pressure during the first hour after than it gradually stabilized and become almost unchanged in the last (3rd) hour which implied that pore fluid is already settled in the connected pores of the sample and saturated the sample well enough to start our measurements. The measurements begin once we have ensured that the pore pressure has stabilized. A rather extensive series of measurements are made at varying pressures and temperatures that follow a protocol of:

- At constant room temperature we change the pore pressure from 20 to 1 MPa maintaining a differential pressure 15 MPa. This set is intended to cross the liquid-vapour phase transition.
- The temperature is raised to 50 ^0C and stabilized, usually after a period of about 2 hours. Again, the pore and confining pressures are cycled at the same constant differential pressure of 15 MPa with the pore pressure changing from 1 MPa to 20 MPa. This path in P-T space crosses the gas-supercritical fluid transition.
- Finally, the pore pressure was kept constant at 8 MPa with the confining pressure at 23 MPa for the same constant differential pressure of 15 MPa, but the temperature was slowly decreased from 50 ^0C to as low as 18 ^0C. Through these measurements we check the transition of supercritical fluid to liquid.

Upon completion of this suite of measurements the sample was then again evacuated to remove any CO_2 from the pore space prior to the water saturated measurements.

3.4.4.1 Influence of heating and cooling rate during CO_2 saturated run

During the liquid to supercritical transition measurements we do an isobaric measurement ($P_p = 8MPa$ constant) with temperature changing from 18^0 C to 50^0 C and cooling again to 18^0 C. From the observation we saw that the cooling and heating rate has a strong influence on the specific temperature where the expected phase change would occur. There are mainly two main reason of this effect

1. the transport of CO_2 into the sample during condensation and out of the sample while precipitation happens when the phase transition occurs, and

2. the time dependency of heat transfer during condensation and evaporation of the CO_2 in the sample.

The temperature reading we get is actually the temperature of the confining fluid measured within the $\sim$ 5 cm vicinity of the sample assembly which necessarily not represent the temperature through the sample; unless it gives time to equilibrate. Using a lumped capacitance method [76] Kofman et al. [77]calculated for our experimental set up with a synthetic sample and showed that it takes almost 2 hours to get a full equilibrium temperature with the cooling bath (Figure 3.2)and within the sample it roughly needs 10 mins to heat up in a specific temperature. They also found that the slower rate of temperature rate always gives a good equilibrium condition with more precise transition happening on expected temperature. To get a reliable result we heat up our sample on a fixed high temperature (50^0 C)for 3 hours to reached equilibrium with cooling bath and the sample. Then we wait 10 mins between two measurements to ensure moderate cooling rate to get a more precise transition.

3.4.5 H_2O saturated runs

The final measurements with the samples were water saturated runs. Distilled water was used for this purpose. After evacuation, the sample was left over night to saturate with water at a constant pore pressure of 10 MPa. We did the measurements the next day at room temperature by changing the pore pressure from 1 MPa to 20 MPa with a constant differential pressure of 15 MPa.

For all measurements we mentioned above include the acquisition of both P- and S- waveforms. We usually waited 5 minutes while changing pore pressures that allowing the fluid pressure to reach equilibrium conditions in the pressure vessel and then recorded the information. We have summarized the measurements for samples depending on saturation type, temperature, and pressure conditions in Table 3.1.

Type of measurements (saturation)	Temperature (^0C)	Confining Pressure (MPa)	Pore Pressure (MPa)	Differential Pressure (MPa)
Dry	21	6-55	0	6-55
	50	6-55	0	6-55
Nitrogen	21	16-27	1-12	15
CO_2	21	16-35	1-20	15
	50	16-35	1-20	15
	18-50	23	8	15
H_2O	21	16-35	1-25	15

Table 3.1: Measurement Summary for different conditions used.

3.4.6 Velocity analysis and error calculation

The time we are measuring from the recorded waveforms includes the time needed to travel through both the sample and the aluminum buffer caps. In order to determine the wave speed of the sample we need to subtract the travel time through the end caps from the total observed travel time. The travel time of end caps, called the delay time, is determined before the measurements with the sample are carried out. The calibration measurements were done by performing ultrasonic pulse transmission through the pair of buffers without the sample. We carried out the calibration measurements with the same set of confining pressures that we will use with the sample and end caps combinations in our experiments. Using the first extremum of the trace we determine the arrival times. If the delay time is t_b and the arrival times for the combination of sample and buffer is t_{bs}, we can determine the travel time of the signal through the sample by the subtraction of $t_{bs} t_b$. If the length of the sample is L_s, the material's wave speed will be:

$$V = \frac{L_s}{t_s} = \frac{L_s}{t_{bs} - t_b} \tag{3.2}$$

.

3.5 Error analysis

In any experimental measurement, error is inevitable. There may be several reasons for this but usually it comes from the lack of precision and uncertainties in the measurements. As our goal is to obtain the material's pressure and temperature dependent wave speed we are expecting two major sources of potential errors: i) the sample length due to measurements errors themselves together with changes induced by variations in confining pressure and temperature, and ii) picking first arrival times from both the end-cap calibrations and the sample itself.

3.5.0.1 Sample length

There are two components to the errors associated with the sample length: the errors in flattening of the sample faces for parallelism ($\sim 20\ \mu m$) and in the change of the sample length due to pressure during the tests. The sample shortening is crudely determined by

$$\frac{\Delta L}{L} = \frac{1}{3}\frac{\Delta P}{K} \tag{3.3}$$

where ΔL is the length shortening, L is the sample length at room temperature, K is the bulk modulus and ΔP is the pressure change. Using the bulk's modulus of the Fontainebleau sandstone's dry runs we took K $\sim$ 7.15 GPa and the maximum pressure exerted on our measurements (55 MPa) gives a sample shortening of

$$\Delta L = 2.56 \times 10^{-5} \times L_s \tag{3.4}$$

depending on the samples length in room temperatures and atmospheric pressure, we calculated the sample shortening for each samples. So the length corrections for sample 1($L_s = 4.65cm$) and sample 2 ($L_s = 6.10cm$):

$$\begin{aligned} \delta L_{s1} &= 15.6 \times 10^{-5} m \\ \delta L_{s2} &= 11.9 \times 10^{-5} m. \end{aligned} \tag{3.5}$$

3.5.0.2 Delay time increment

The distance that the waves must propagate is also affected by the temperature of both the end-caps and the sample. The end-caps are made from aluminium that has a relatively large co-efficient of thermal expansion of about $22.2 \times 10^{-6}/^0C$. However, because we have calibrated the end caps directly this change in length is already implicitly accounted for. We do not know the thermal expansively of our samples. However, as will be shown in the next chapter they are nearly pure crystal quartz. The thermal expansion of pure quartz is highly anisotropic with the co-efficients being $13.71 \times 10^{-6}/^0C$ and $7.48 \times 10^{-6}/^0C$ parallel and perpendicular to the c-axis, respectively with a density temperature co-efficient of -34.92 $\times$ $10^{-6}/^0C$ [78, 79]. Using the coefficient a length increment is found as 18.5 μm which is not significant.

3.5.0.3 Time Picking Errors

The errors in our ability to accurately pick the transit time come from two major sources: the limits of the digitization sampling period of 10 ns and ambiguities in properly interpreting the observed waveforms. The sampling rate of the acquisition system is 10 ns, so we have a minimum error of 10 ns for high quality signal and for low quality signal there is a maximum error of 30 ns [37]. So the error in time:

$$\begin{aligned} \delta t_p &= 30 \times 10^{-9} s \\ \delta t_s &= 30 \times 10^{-9} s \end{aligned} \tag{3.6}$$

3.5.0.4 Total estimated error

Using all possibilities of sources of error in velocity , we use the following equation to find out the error in velocity,

$$\frac{\delta V_s}{V_s} = \sqrt{(\frac{\delta L_s}{L_s})^2 + (\frac{\delta t_s}{t_s})^2} \tag{3.7}$$

here δ stands for the error of the corresponding parameters. We use this relation in our experimental data to find out the error bars for each measurement.

Chapter 4

Sample Characterization

In order to best interpret our wave speed measurements it is crucial that we carry out a detailed characterization of the two Fontainebleau sandstone samples. In this chapter, we describe a variety of petrophysical parameters including mineralogy, grain and bulk density, porosity, air permeability, pore throat dimensions, and pore network tortuosity. These values are important inputs to modelling of the behaviour later. Moreover, we image the samples using scanning electron microscopy (SEM) and X-ray microcomputed tomography in order to analyze their micro-structure. All characterization work was carried out at University of Alberta facilities. In this chapter we will briefly discuss the methodologies used and provide a summary table of these the important petrophysical properties.

4.1 Fontainebleau Sandstone samples

The experimental measurements are carried out on two Fontainebleau sandstone samples. Fontainebleau sandstone is collected from the Paris basin (France). It is clean sandstone of Oligocene age deposited in the Stampian period as dunes bordering the shore of Paris basin about 28.1-33.9 Ma. It consists of nearly pure quartz grains ($\sim$ 99.8% pure quartz), which are wellrounded (surface roughness 1), and well-sorted [80, 81]. The porosity of this sandstone is predominantly intergranular and ranges widely from 2% to 28% being controlled by the degree of cementation by silica precipitation [82, 83]. The Fontainebleau sandstone shows a relatively homogeneous grain size distribution with an average grain diameter range 150-300 μm and 250 μm is mean grain diameter as determined by a number of scientists [84, 85]. Fontainebleau sandstone is widely used to provide and test permeability and porosity relationships [84, 53, 86, 87, 81] and electrical conductivity under saturated and unsaturated conditions [88, 89, 90, 91, 92]. In the case of CO_2 saturated measurements not much work is done on the Fontainebleau. We will study this specific saturated measurement in this thesis work.

(a) (b)

Figure 4.1: Photographs of the Fontainebleau samples a) Vif (hard) types and b) Franc type.

The particular materials used in this thesis were obtained from the quarry operated by Ets Les Gres de Fontainebleau & Cie, approximately 1.2 km west of the commune of Moigny sur Ecole and about 60 km south of Paris, operated by F. de Oliveira (http://gresdefontainebleau.free.fr/). The Fontainebleau sandstone is a clean white sandstone composed primarily of fine to medium sized quartz grains (Wentworths grain size scale. Monsieur de Oliveira provides three types of Fontainebleau sandstones depending on their cementation strength that they call Maigre (friable), Franc (semi-solid), and Vif (hard). These classifications mostly arise from the practical usage of the stone in construction. In this study one of the samples is semi-solid and the other is solid. The friable sample, already damaged heavily during transport to Edmonton, was not able to be machined to make a suitable test piece. The characterization of these samples is described in detail below.

4.2 Density and Porosity

In this section we will characterise the samples with some of their intrinsic properties including grain density, bulk density, porosity, and pore size. We used a helium pycnometer to determine the sample's grain volume from which we can also calculate the grain density and the porosity. Using the mass of the sample and measured dimensions we found out the bulk density of the sample. Pore size distribution is determined through mercury injection porosimeter.

4.2.1 Grain Volume and density

The grain volume of the sample is determined using helium pyncnometry. We used Quantachorme Instruments MVP-D160-E helium pycnometer whose governing principle is Boyle's gas law. Here we will briefly discuss the working principle

For a constant mass of a 'perfect' gas, Boyle's gas law says that

$$P_1V_1 = P_2V_2, \tag{4.1}$$

where P_1 and V_1 are initial gas pressure and volume, and P_2 and V_2 are the final gas pressure and volume, respectively. There are two compartments in the pycnometer: one for reference and the other for the sample. The sample compartment can be opened by removing the lid. The pycnometer essentially allows the volume of the solid portion of the sample to be calculated according to

$$P_1 V_R = P_2(V_R + V_s - V_g), \tag{4.2}$$

Here P_1 is the pressure resulting from helium gas inside the reference compartment only when the sample compartment subject to vacuum is disconnected and P_2 is the pressure in both compartments after they are connected and He gas flows from the reference volume V_R into the sample compartment volume V_s. V_g is the volume of the solid portion of the sample. The sample compartment (sample cell) was at atmospheric pressure during measurements. Figure 4.2 shows the image of the pycnometer.

Figure 4.2: Multipycnometer from Quantachrome Instruments [http://www.quantachrome.com/density/multipycnometer.html].

The pyncnometer volumes $V_R = 88.5cm^3$ and $V_s = 147.903cm^3$ were predetermined during calibration. Using this information and the original P_1 and final P_2 measured pressures allows the solid, or grain, volumes V_g of our samples to be calculated from equation 4.2. We can then easily determine the grain density ρ_g as the ratio of the dry sample mass m to the grain volume V_g through the following equation:

$$\rho_g = \frac{m}{V_g}. \tag{4.3}$$

The mass of the dry sample was found from weighing the sample using a sensitive balance (My Weigh iM01). We show the value for each sample in table 4.2.

4.2.2 Bulk Density and Porosity

The bulk density of the sample is determined from the ratio of the dry mass of the sample m to its envelope volume, V_e. Here, we found V_e from the measured sample lengths and diameters using a Vernier calliper,

$$\rho_b = \frac{m}{V_e}. \tag{4.4}$$

The values are enlisted in the table 4.1. This simple calculation of bulk density does not necessarily give the best answer primarily because of the uncertainties associated with the measurement of the dimensions of the sample even for the simple geometry of a cylinder. Porosity is one of the most important properties of any porous medium. We determine this parameter using He pycnometry and Hg porosimetry. In the case of He pycnometer the porosity ϕ of a sample is determined by

$$\phi = 1 - \frac{V_g}{V_e}. \tag{4.5}$$

Where V_g is the grain volume and V_e is the envelope volume.

Fontainebleau sample type	Diameter (cm) $\pm 2.5 \times 10^{-8}$	Length (cm) $\pm 2.5 \times 10^{-8}$	Envelope Volume (cm^3)
Franc	3.5	4.65	44.74
Vif	3.5	6.1	58.68

Table 4.1: The measured dimensions and envelope volume of the samples.

4.2.3 Pore Size Distribution: Hg porosimetry

Mercury injection porosimetry is used to find out the pore size and their distribution. The methodology of Hg-porosimetry includes injecting liquid mercury, which is a non-wetting fluid with a contact angle, θ , of about 140^0 inside the pore space of the porous sample. An external pressure is required to force the liquid mercury into the pores and the smaller the pore throat through which the Hg must pass the greater the pressure. From the Washburn equation [93] we get the relationship between the pressure applied and pore throat diameter normally employed in mercury intrusion studies,

$$D_{pore} = -\frac{4\gamma cos\theta}{P}. \tag{4.6}$$

where D_{pore} represents the pore throat diameter, P is the applied pressure to inject the mercury inside the pore, γ is the mercury's surface tension ($0.485Nm^{-1}$ at 25^0), and θ is the contact angle. In our instrument the maximum pressure is 423 MPa and this, in principle, allows pore throats as small as 3.5 nm to be probed. The pore size actually measures the size of the pore throat not the size of the pores' inside dimension. Therefore, we measure the pore throat size distribution. The pores which are not connected with the outer pores cannot be measured by this method.

An Autopore IV 9510 mercury injection porosimeter manufactured by Micrometrics was used for the pore throat size distribution. The essential measurement is a precise tracking of the volume of the Hg injected to the sample with pressure. The equation used in the measurements is

$$\delta V_{Hg} = \frac{dV_{Hg}}{dP}\Delta P, \tag{4.7}$$

where V_{Hg} is the volume of the mercury imbibed and P is the pressure applied. The Equation (4.7) indicates the volume change due to the mercury that has intruded into the pore space from the last pressure to the new pressure. Using this equation we can quantify the relative distribution of the porosity of the sample among the porosity. From the graphical representation we expect to see a sharpen increase in the cumulative intrusion curve with a peak in the incremental intrusion curve. Figures 4.3a) and 4.4a) give plots of incremental and cumulative intrusion with pressure for the Franc type and Vif type Fontainebleau samples, respectively. Using Washburns' equation we converted pressure to pore size, Figures 4.3b) and 4.4b) give the graphical presentations of incremental and cumulative intrusion with pore size. The dominating pore throat radius is found at the largest peak of plot of incremental intrusion curve with pore size. The soft Fontainebleau sandstone shows a single large peak in the incremental intrusion curves and the dominant pore size is $7.23\mu m$ from the figure 4.3b). The Vif type sample of Fontainebleau sandstone shows a significant peak with a few numbers of minor peaks in the incremental intrusion curves. This less smooth in incremental intrusion curves signifies that Franc Fontainebleau sandstone sample pore size distribution may be more than the Vif type samples. From the largest pick (Figure 4.4b)) we consider the dominant pore size of this sample to be $17.25\mu m$.

4.2.4 Permeability

Permeability is one of the important petrophysical properties of a porous material, it quantifies the ease with which a fluid can flow through the pores of the medium given a pressure gradient. Interconnected and open pores influence the

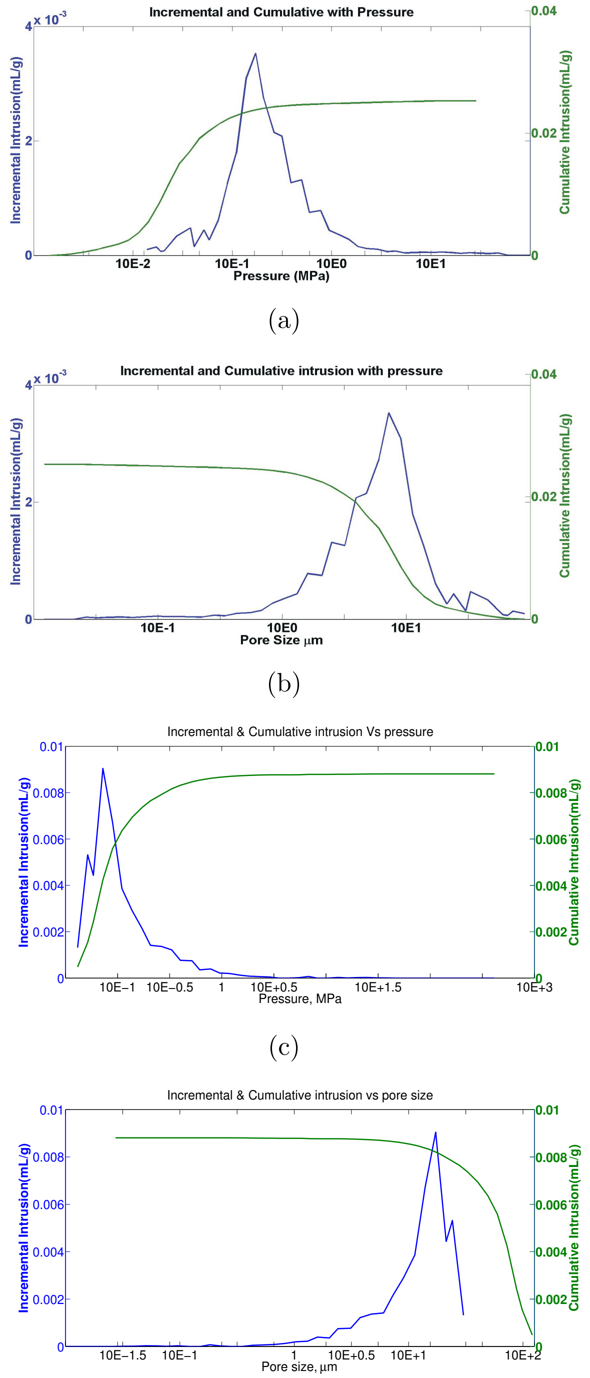

(a)

(b)

(c)

(d)

Figure 4.3: Incremental and Cumulative intrusion curves for the Vif type of Fontainebleau sandstone a) and c) with pressure b) and d) with pore size for Franc and Vif sample, respectively.

permeability. Permeability κ relates fluid flow per second per area (Darcy Velocity q), and fluid physical properties (i.e viscosity η) to the pressure gradient, dP/dx applied to the porus media:

$$\kappa = \frac{q\eta}{\left(\frac{dP}{dx}\right)}. \tag{4.8}$$

A portable air permeameter, the Tiny Perm II made by New England Research Inc., was used to measure the permeability of the samples. This device does not give a precise measurement of the permeability. Professor David Potter at the department of physics at the University of Alberta provided this device. The device consists of a plunger connected to a vacuum cylinder with an attached pressure transducer, which is connected to a microprocessor and control unit by an electrical cable. Figure 4.5 gives a picture of the device we used. When we used the device we obtained an instrument dependent response function that relates to the amount of time it takes for the air pressure induced by a plunger placed on top of the sample surface to depressurize. If the response function is T, the permeability of the sample is related through the following instrument dependent calibration relationship,

$$T = -0.8206 \times log_{10}(\kappa) + 12.8737. \tag{4.9}$$

An average value of T was taken from several permeability readings on a sample. The average permeability values are listed in table 4.2. It must be noted that the permeability we have measured is actually the air permeability, which is generally higher than their liquid permeability [94, 95, 96, 97] for rocks having low permeability.

4.2.5 Tortuosity

Tortuosity is a factor that describes the complexity of the transport pathways through the pore space of the media. It essentially provides a measure of the

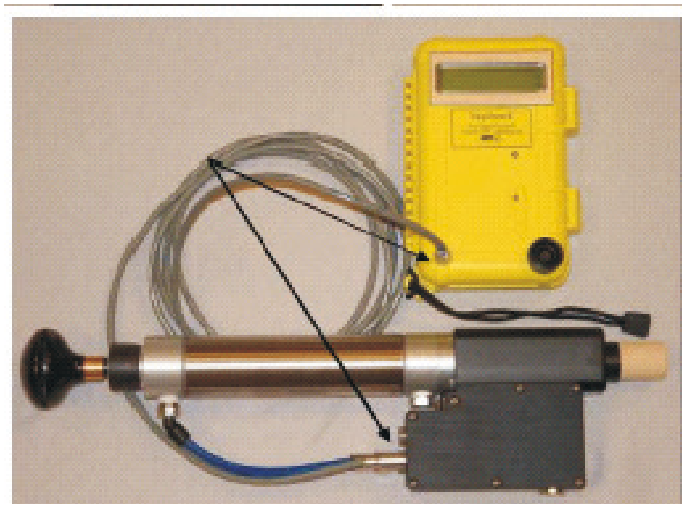

Figure 4.4: Tiny Perm II, the portable air perameameter system we used for permeability measurements of our samples. The two black arrows indicate the connection between the pressure transducer in the black rectangular shape black box to the yellow microprocessor unit [4].

average length of the path fluid molecules must take to pass from one side of a sample to the other. It could also be considered as a retardation factor which measures the resistance of a porous medium to the flow [5]. Figure 4.6 depicts a sketch of streamlines of fluid flowing through an arbitrary model with porosity 0.6 and tortousity 1.15. By definition tortousity, τ, is the ratio of the distances of the actual path taken, L_c, through the network of channels to the straight path length, L_0 between the same initial and final points on the sample,

$$\tau = \frac{L_c}{L_0} \geq 1. \tag{4.10}$$

The tortousity of our samples used in this work was calculated by introducing a percolation porosity (representing the minimum value of the connected porosity) in the Archies law. This modified version of Archies law proposed by Sen et al. [98] gives the formation factor, F, as

$$F = (\phi - \phi_p)^{-m}, \tag{4.11}$$

where ϕ is the porosity of the sample, ϕ_p denotes a porosity at the percolation threshold and m is the cementation factor which is taken to be 1.5 from the literature [98, 99]. The bulk tortousity, τ, of the pore space can also be defined using formation factor, F, and porosity, ϕ, as

$$\tau = F\phi = (\phi - \phi_p)^{-m}\phi. \tag{4.12}$$

For our calculation we use the value of percolation porosity and cementation factor from Revil et al.[100] as he determined these values from an extensive set of measurements on Fontainebleau sandstone samples. The values are, $m = 1.46 \pm 0.05$ and $\phi_p = 0.019 \pm 0.04$. The tortousity of our samples calculated through this equation are given in the table 4.2.

Properties	Franc Fontainebleau	Vif Fontainebleau
Mass (g)	137.16	167.2
Bulk Density (kg/m^{-3})	2487.3	2314
Grain Density (kg/m^{-3})	2640	2647
Porosity (%)	6.28 (Hg porosimeter) 8 (Helium Pycnometer)	12.5 (Hg porosimeter) 10 (Helium Pycnometer)
Modal Pore Size (μm)	7.23	17.25
Air Permeability (mD)	16.58	16.56
Tortousity (unit less)	7.09	3.673

Table 4.2: Petrophysical properties of the samples.

4.2.6 Scanning Electron Microscopy (SEM)

For testing the grain structures and micro-features qualitatively we carried out a scanning electron microscopy (SEM) survey of our two samples. A SEM is a microscope where electrons are used instead of light to form an image. We used the Zeiss EVO MA 15 SEM for imaging our samples with magnifications to 100,000 X. When we put our sample inside the SEM, a beam of electrons is emitted from an electron gun that interacts with the surface of the sample,

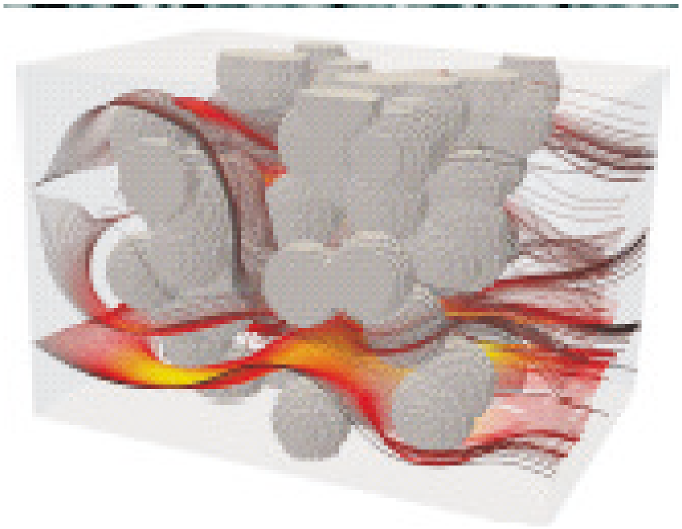

Figure 4.5: Colourful streamlines shows the fluid flow through a 3D random model porous sample with a porosity of 0.06 and tortousity 1.15. Reproduced with permission from [5]. Copyright [2012], AIP Publishing LLC.

dislodging secondary electrons from the specimen. Through a strong magnetic field the electron beam is manipulated. The scattered secondary electrons are attracted by an electron detector and additional sensors detect backscattered electrons (reflected off from the sample surfaces) and X-rays emitted from the beneath the sample surface. Using these sensors and scanning coils, which are used to move the beam precisely as desired, we get a scanned detail image of the sample onto a monitor to view. Before our scanning, samples are coated with gold to provide conductivity on the sample surface to prevent electron traps which might make an overly bright image. The SEM imaging was done at the Earth and Atmospheric Science department at the University of Alberta [4].

Figure 4.6 and figure 4.7 show the SEM image of two Fontainebleau sandstone samples of a) Franc type and b) Vif type, respectively, with two different magnifications. The first magnification of X150 shows the quartz crystals pretty clearly where we noticed that crystals are interlocked with each other with little cementation apparent. For Franc sample in Figure 4.7 a) shows a magnified portion of the sample where we see the clean quartz crystals, b) shows one of the micro-cracks and c) give the picture of healing happening inside the rock.

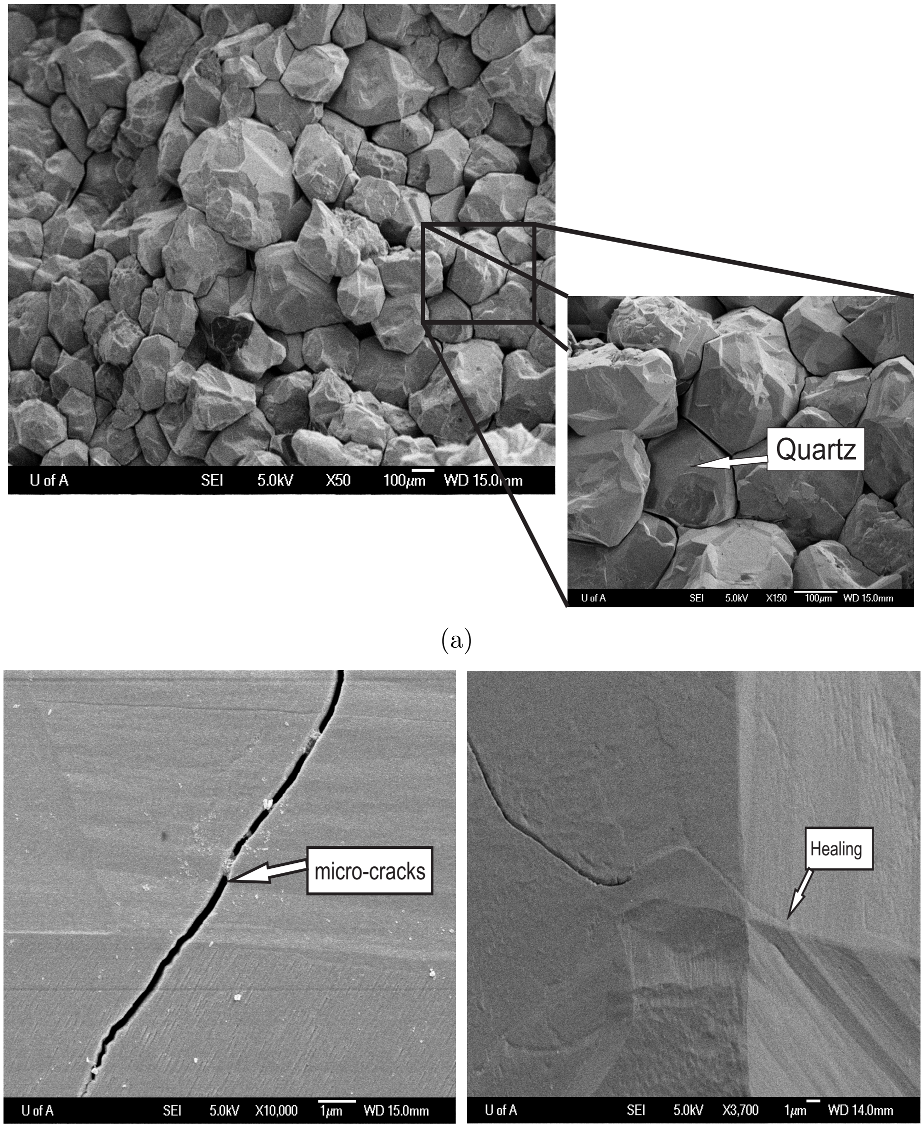

(a)

(b)

(c)

Figure 4.6: SEM images of Franc type sample of Fontainebleau sandstone a) a zoomed portion of the sample with X150 magnification b) presence of microcracks and c) occurring of healing process inside the sample.

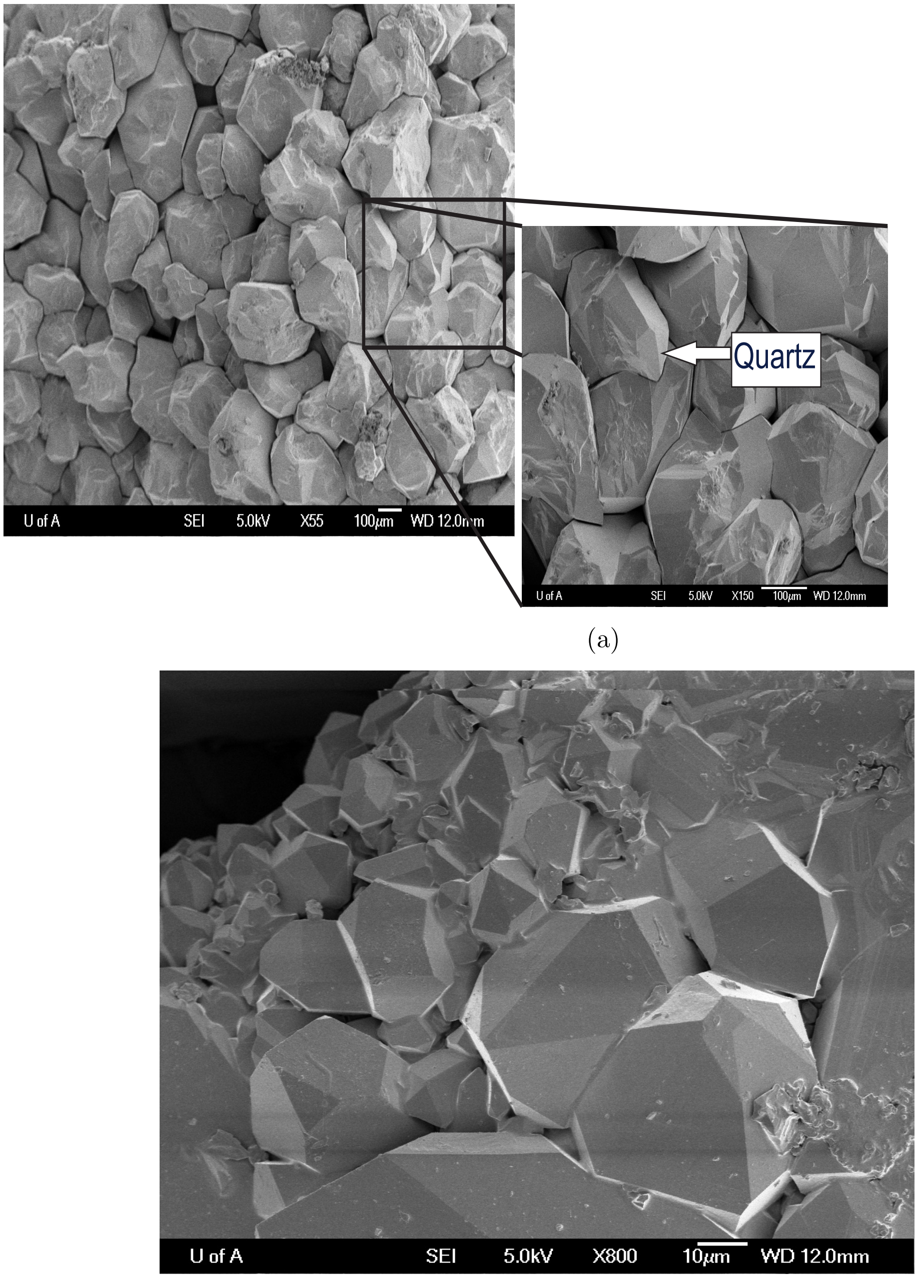

(a)

(b)

Figure 4.7: SEM images of Vif type sample of Fontainebleau sandstone a) zoomed portion with a X150 magnification b) a larger magnification of X800 shows how the crystals are cemented with each other.

4.2.7 micro-Computer Tomography (μ -CT)

We have done a number of $\mu - CT$ images to construct a 3D representation of one of our samples. Micro-CT is non-destructive technique that gives a direct way to image the pore space as a volumetric (3D) represtation of the structure. In a $\mu - CT$ scanner X-ray s illuminate the small object from a variety of directions, and in each direction a shadow image is produced. This shadow image essentially maps the attenuation of the x-rays that are largely related to the density of the material through whcih the x-rays pass. These data are then inverted to a series of layered 2D scans using a filtered back projection algorithm [101] that does not alter the original model [102]. We used a SkyScan1172 high-resolution micro-CT which is a 11 MP (Mega Pixels) X-ray $\mu - CT$ with a resolution of max. 0.7 μm. In our image we used a fine resolution of 5.03 μm to have good look in our pore network.

In Figure 4.8 a) we see a 3D block representation of our Vif sample with a dimension of $\sim 3.456mm \times 3.456mm \times 4.485mm$. Anything less than 100 voxels (voxel is the 3D pictorial unit) are filtered out. We made another fine filter in a smaller 3D block where anything less than 400 voxels are removed. The net like structure represents the largest and longest pore network in the volume which are connected with each other.

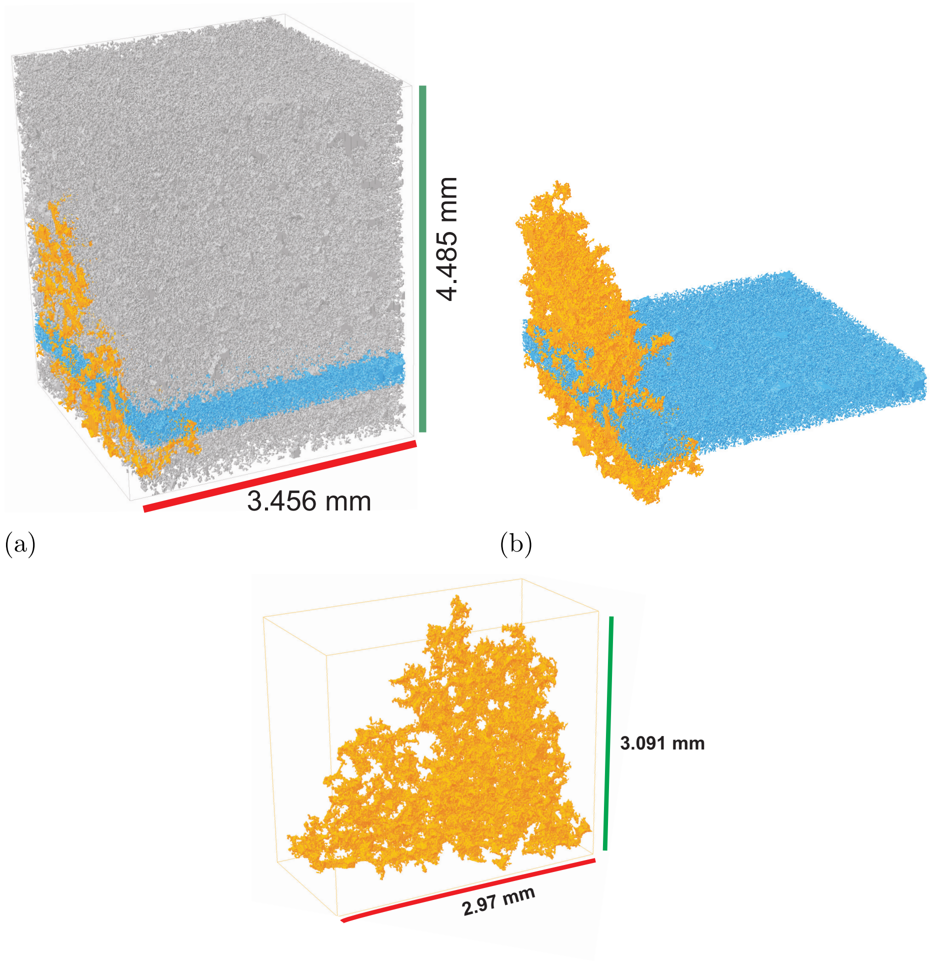

(a) (b)

(c)

Figure 4.8: a) a block of the sample of a dimesion of $3.46mm \times 3.456mm \times 4.485mm$ showing a blue small portion and the connected pores, b) a slice from the block which is finely filtered for the pores c) largest connected pore network which is extended out from the blue slice.

4.3 Summary

We have discussed about the petrophysical characterizations of our two Fontainebleau samples. For bulk volume, grain density and porosity we have utilized the helium porosimeter. We have noticed that two samples show a porosity of 6.28% and 12.5% for soft type and medium hard type of Fontainebleau, respectively. For determining the pore size distribution and pore throat diameter we used mercury porosimetry, which shows a modal pore distribution with a dominant pore diameter for soft one but two significant peaks for other sample where we only considered the largest one for our dominant pore diameter. A portable air permeameter was used to determine the air permeability of the samples. Both of the samples show almost same permeability in these measurements. For tortousity measurements we used the modified Archie's law where we used the information of porosity, percolation porosity threshold and cementation in consideration. Then we presented the SEM images for both samples in two magnifications. Both samples were clean and mostly consisted of quartz crystal interlocked with each other. We saw some micro-cracks presence in the soft one while the other sample seems have less micro fractures in it. At the end, three μCT images of the sample were presented. We see how the pore network is connecting with each other through out the sample.

Chapter 5

Experimental Results and Discussions

In this chapter we will give the experimental results and discussions on the wave behaviours of the two types of Fontainebleau sandstone with variation of temperatures, pressures and fluid saturations. The discussion on the transverse and longitudinal waveforms and the corresponding wave velocities will be presented for all four cases of saturation: dry, N_2 saturation, CO_2 saturation and H_2O saturation.The ultrasonic pulse transmission technique is employed as has already been presented in Chapters 2 and 3. We will start with dry runs which are the measurements when the samples are in vacuum conditions, there is no fluid presence inside the sample, then we will represent the measurements done with N_2 saturations (plotted along with dry measurements) to see the effects of a fluid which shows almost inert behaviours in its normal conditions (room temperature), the next section will give three different phase transition measurements when the samples are saturated with CO_2, and at the end we will see how the samples behave when saturated with water. With these three scenarios we can compare the changes happening in the samples due to different fluids depending on various fluid properties.

To get the clear understanding about my experimental results I have summarized the measurement schedule for samples depending on saturation type, temperature, and pressure conditions in the table 5.1.

Type of measurements (saturation)	Temperature (^0C)	Confining Pressure (MPa)	Pore Pressure (MPa)	Differential Pressure (MPa)
Dry	21	6-55	0	6-55
	50	6-55	0	6-55
Nitrogen	21	16-27	1-12	15
CO_2	21	16-35	1-20	15
	50	16-35	1-20	15
	18-50	23	8	15
H_2O	21	16-35	1-25	15

Table 5.1: Measurement Summary for different conditions used in samples

5.1 Dry Observations

Under dry conditions (no fluid presents in the sample) P-and S-waveforms are obtained at two different temperatures: 1) at room temperature (21^0 C), and 2) high temperature (50^0 C) over a range of confining pressures from 6 to 55 MPa. In each test measurements continued during both pressurization and depressurization of the sample in order to examine its degree of hysteresis. These runs are carried out in order that we understand the effects of temperature on the rock's frame allowing the proper, possibly temperature dependent, frame properties to be determined. This is necessary for the later theoretical calculations.

5.1.1 Dry Waveforms

Figures 5.1 to 5.8 display four sets of observed (the sample pore space is vacuum during these measurements) normalised P-and S-waveforms with their corresponding colored amplitude diagrams. Figure 5.1, 5.2, 5.5 and 5.6 shows the measurements for the Franc sample and Figures 5.3, 5.4, 5.7 and 5.8 shows the measurements done on the Vif sample Fontainebleau. We have normalized the signals with respect to the largest amplitude within the given set of waveforms. The waveform plots show well the nonlinear decrease in travel times with increasing confining pressure due to the progressive closure of microcracks.

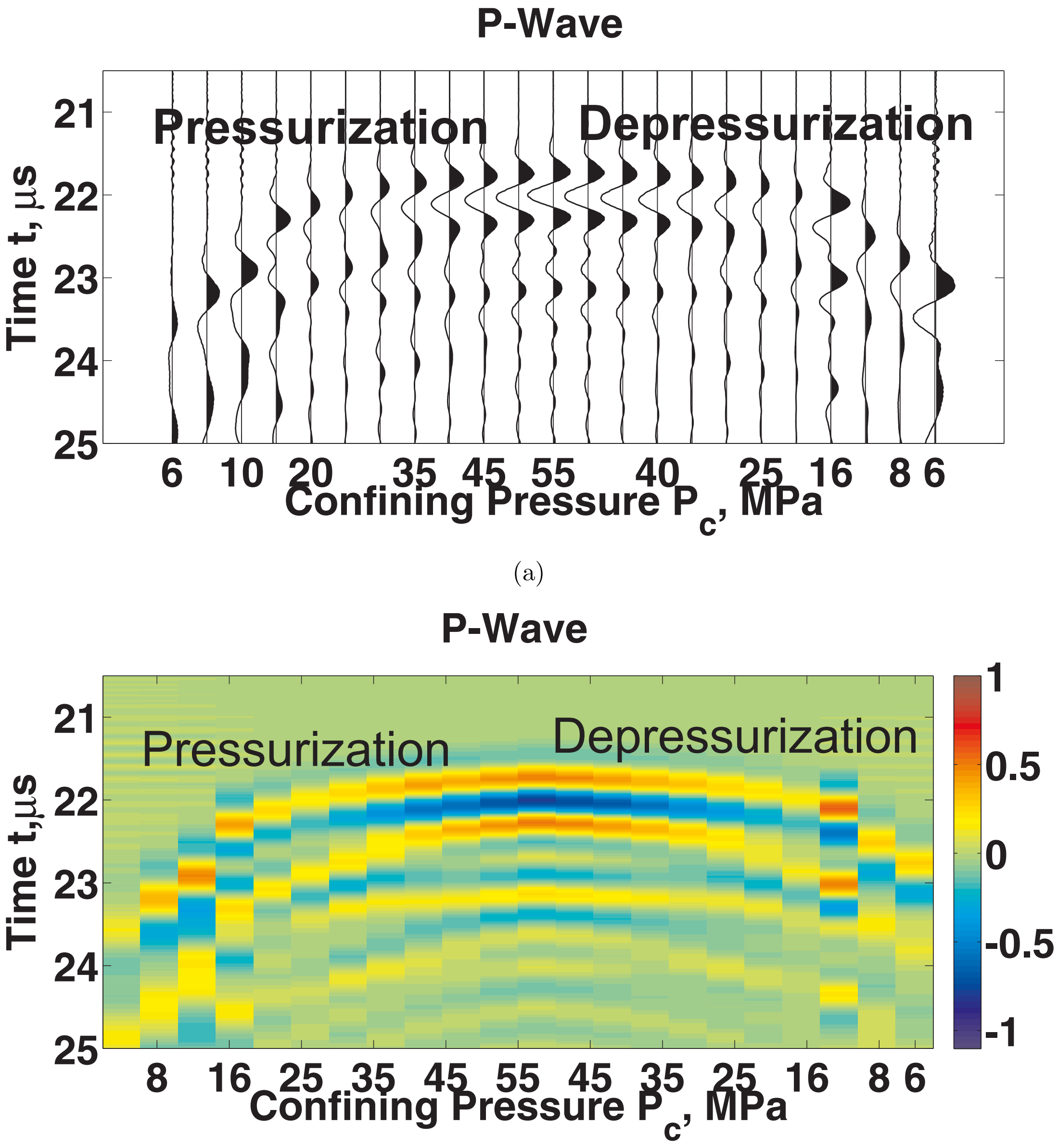

(a)

(b)

Figure 5.1: Normalized (a) P -wave obtained under dry conditions at room temperature as a function of confining pressure and (b) is the colored amplitude plot for P- waveform for Franc type of Fontainebleau sandstone.

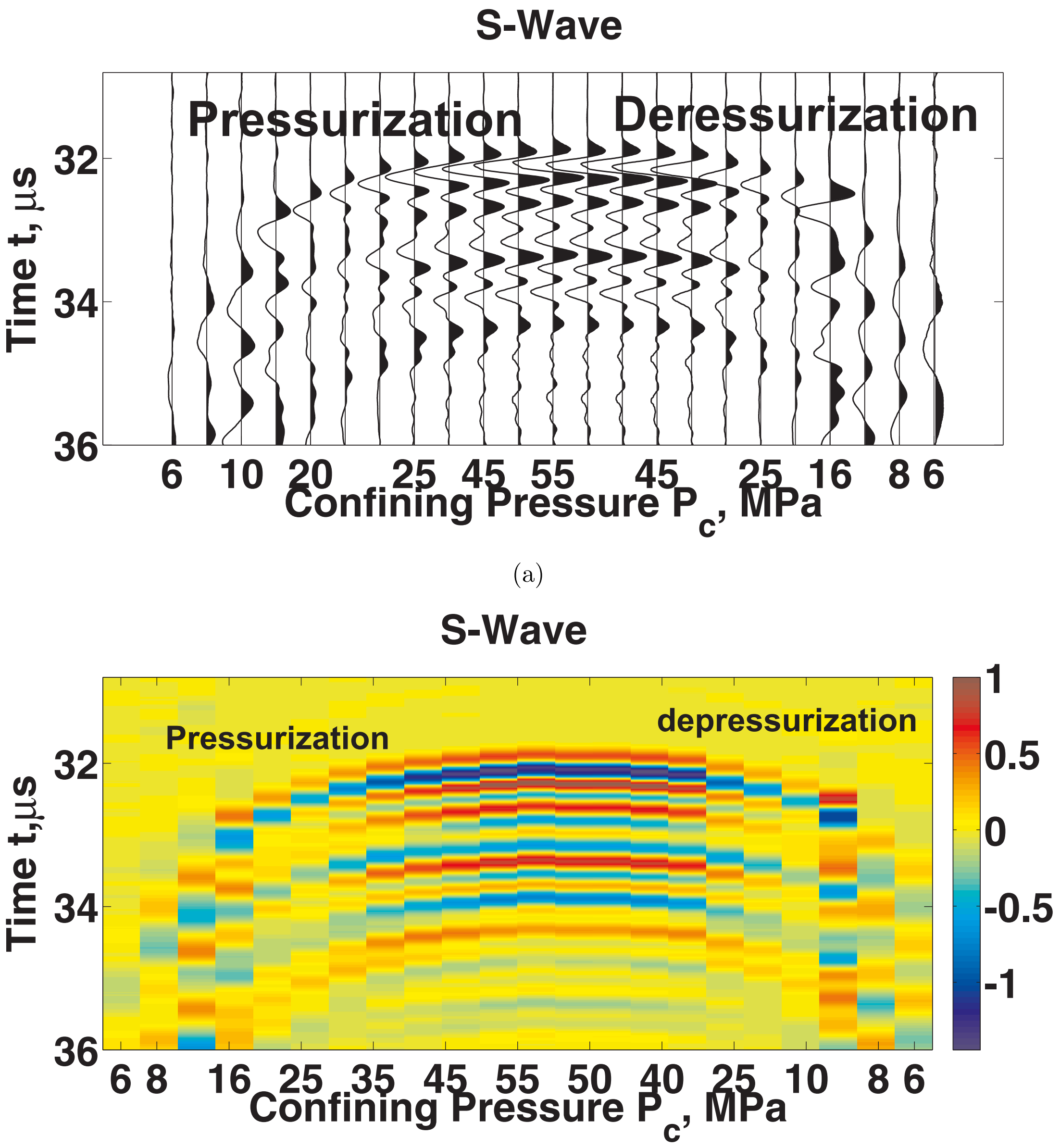

(a)

(b)

Figure 5.2: Normalized a) S-wave obtained under dry conditions at room temperature as a function of confining pressure) and b) is the colored amplitude plot for S-waveform, for Franc type of Fontainebleau sandstone.

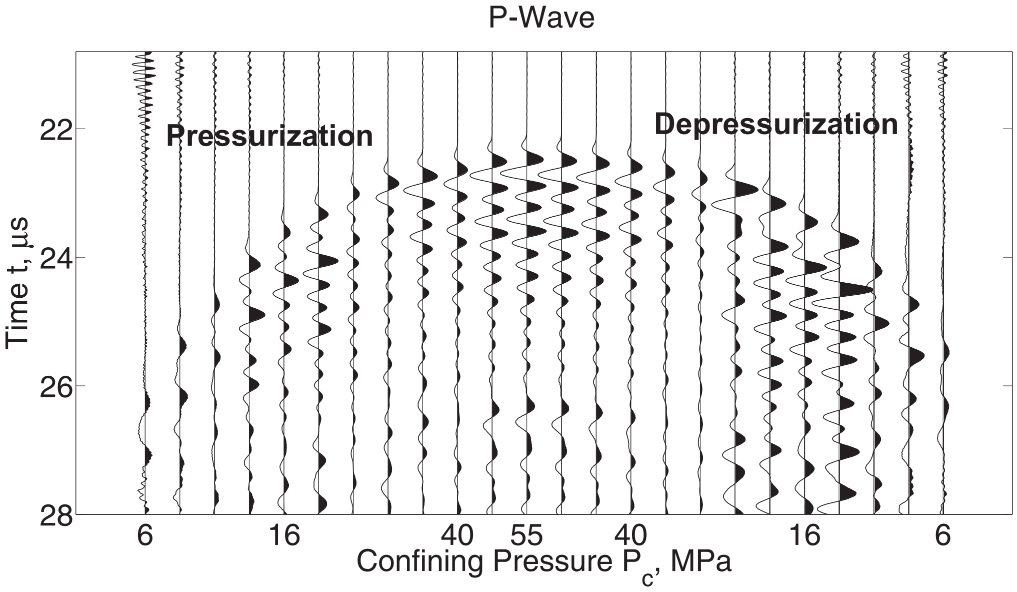

(a)

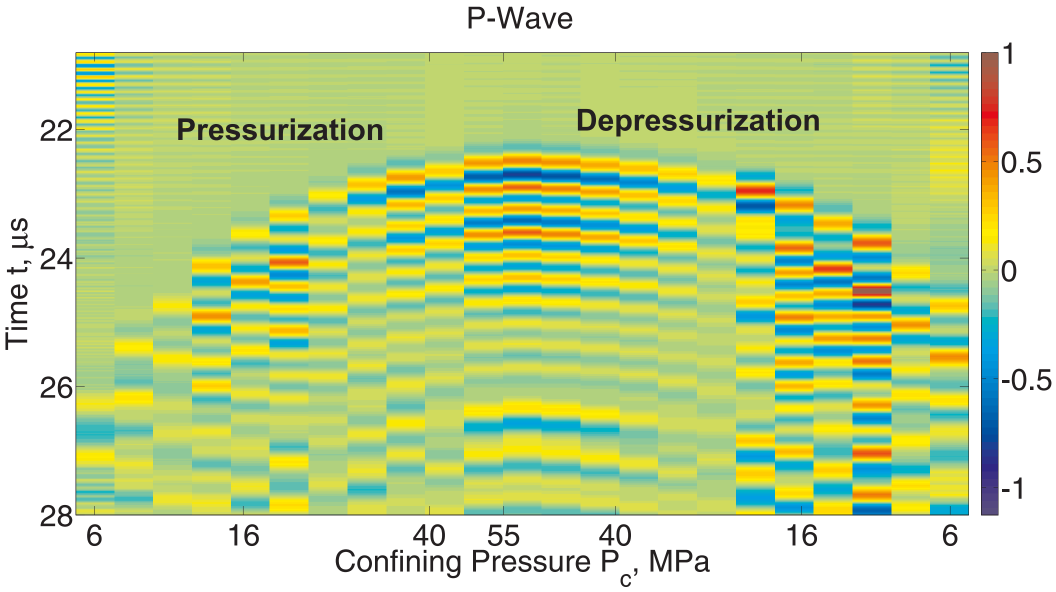

(b)

Figure 5.3: Normalized (a) P -wave obtained under dry conditions at room temperature as a function of confining pressure and (b) is the colored amplitude plot for P- waveform for Vif type of Fontainebleau sandstone.

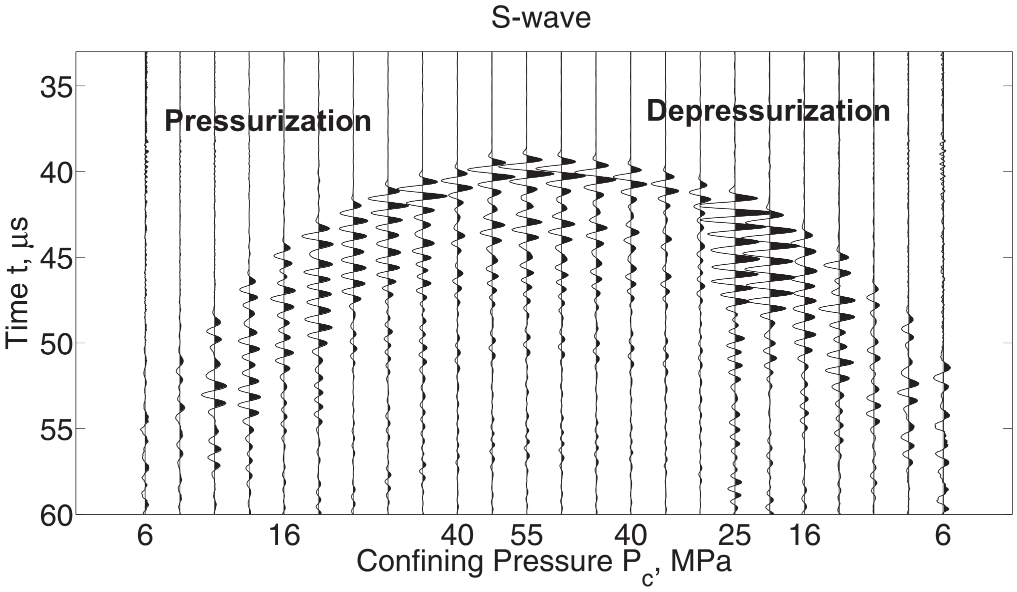

(a)

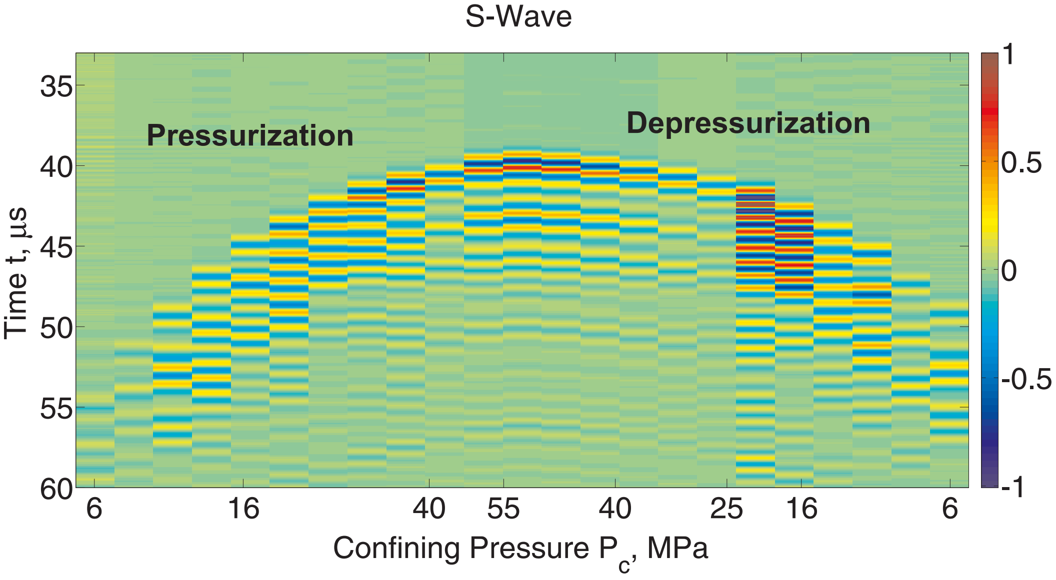

(b)

Figure 5.4: Normalized a) S-wave obtained under dry conditions at room temperature as a function of confining pressure and b) is the colored amplitude plot for S-waveform for Vif type of Fontainebleau sandstone.

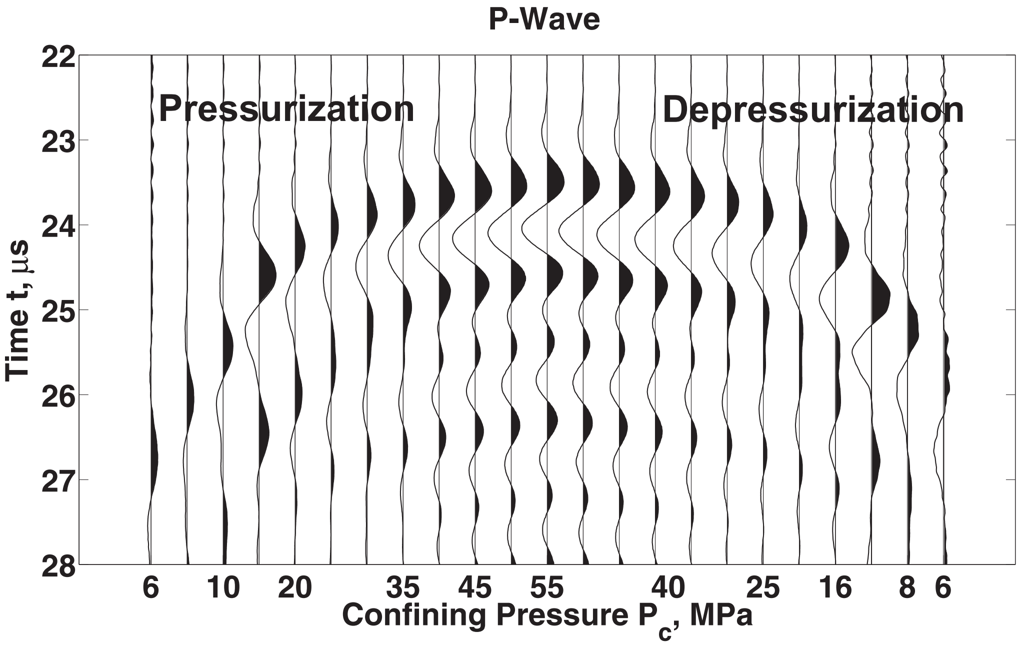

(a)

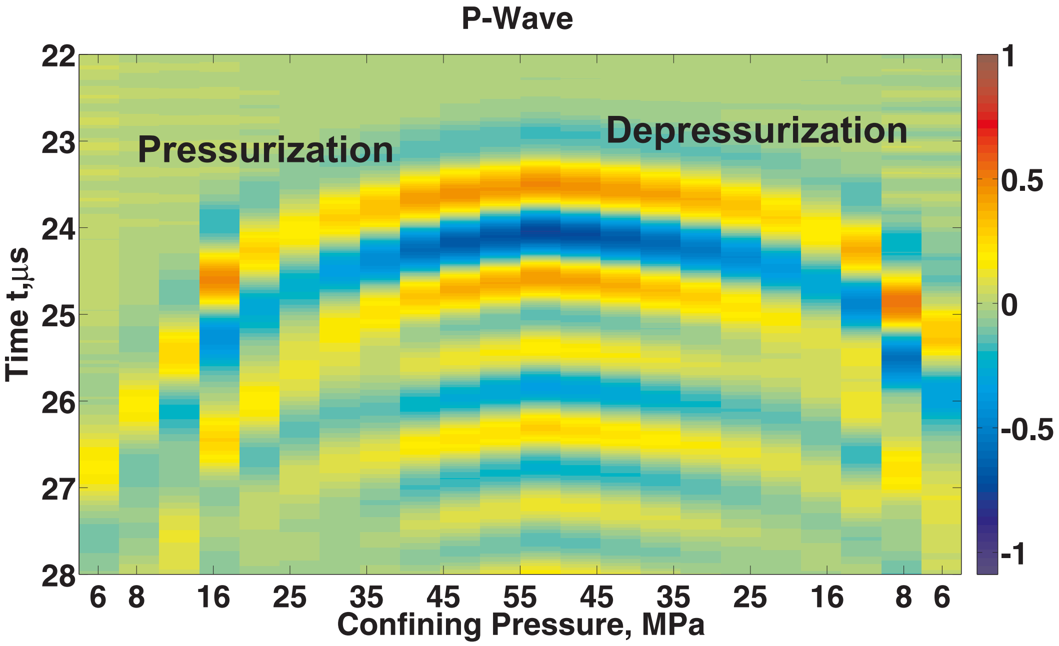

(b)

Figure 5.5: Normalized (a) P -wave obtained under dry conditions at high temperature as a function of confining pressure and (b) is the colored amplitude plot for P- waveform for Franc type of Fontainebleau sandstone.

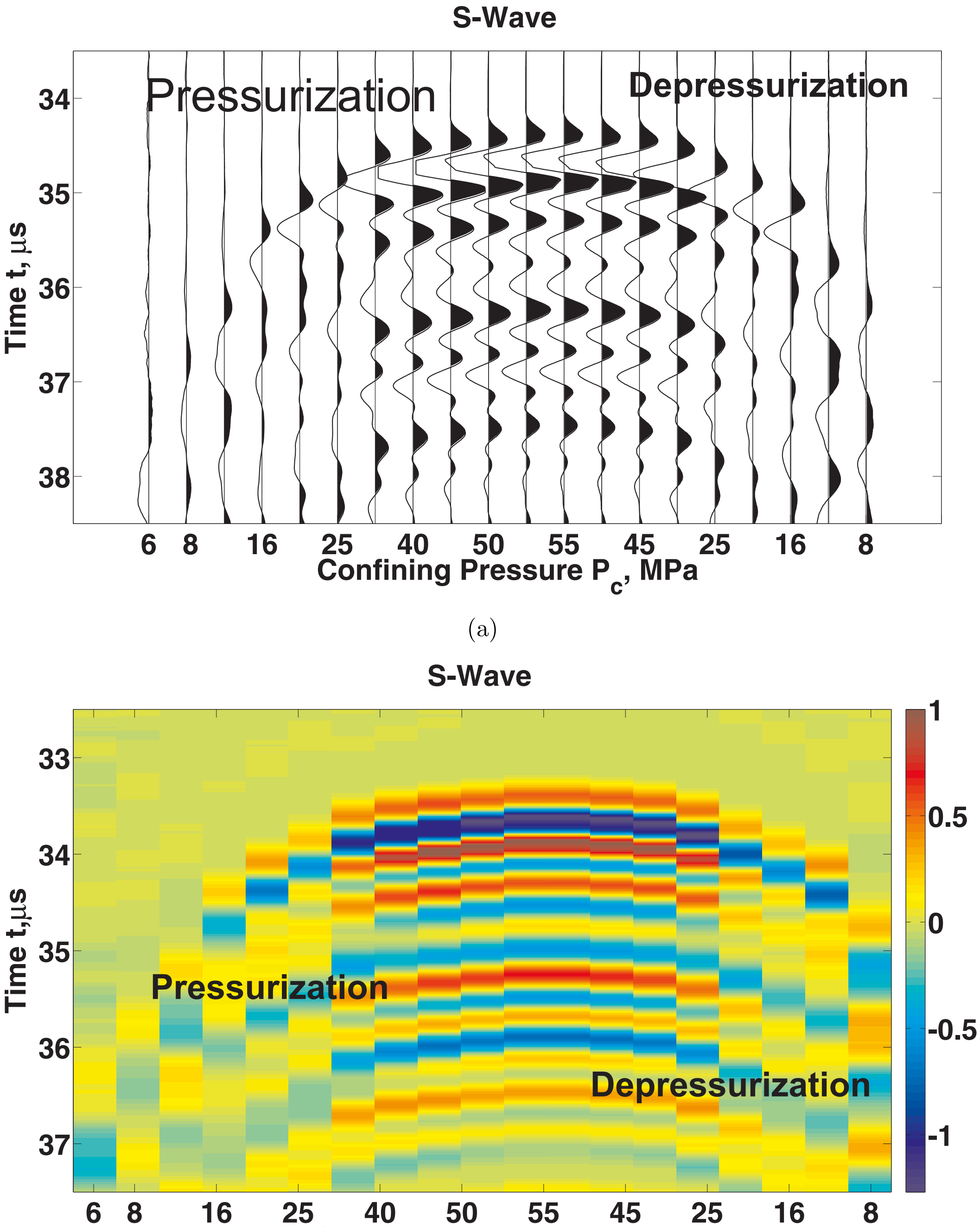

(a)

(b)

Figure 5.6: Normalized a) S-wave obtained under dry conditions at high temperature as a function of confining pressure) and b) is the colored amplitude plot for S-waveform for Franc type of Fontainebleau sandstone.

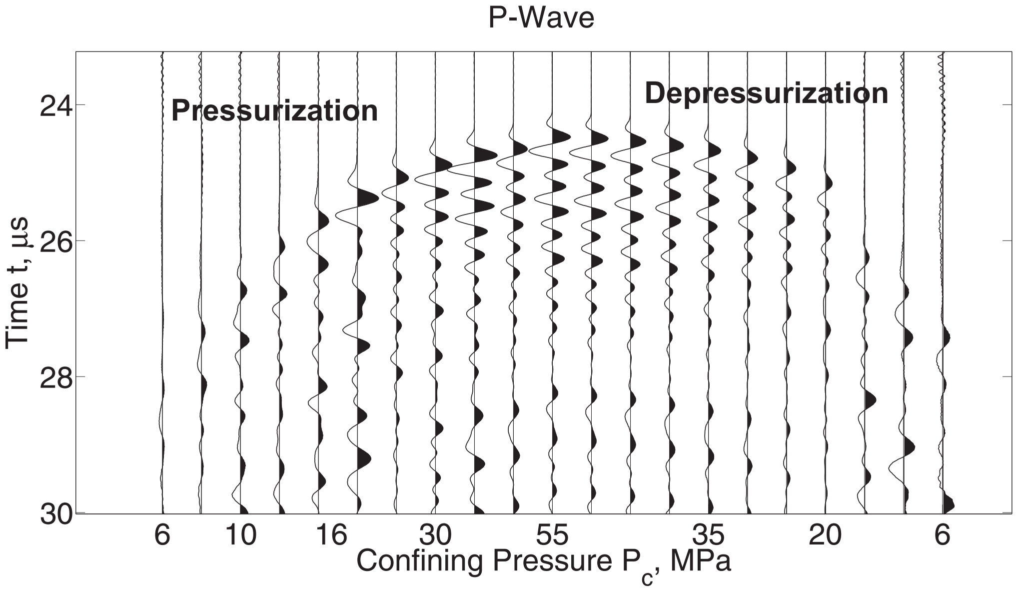

(a)

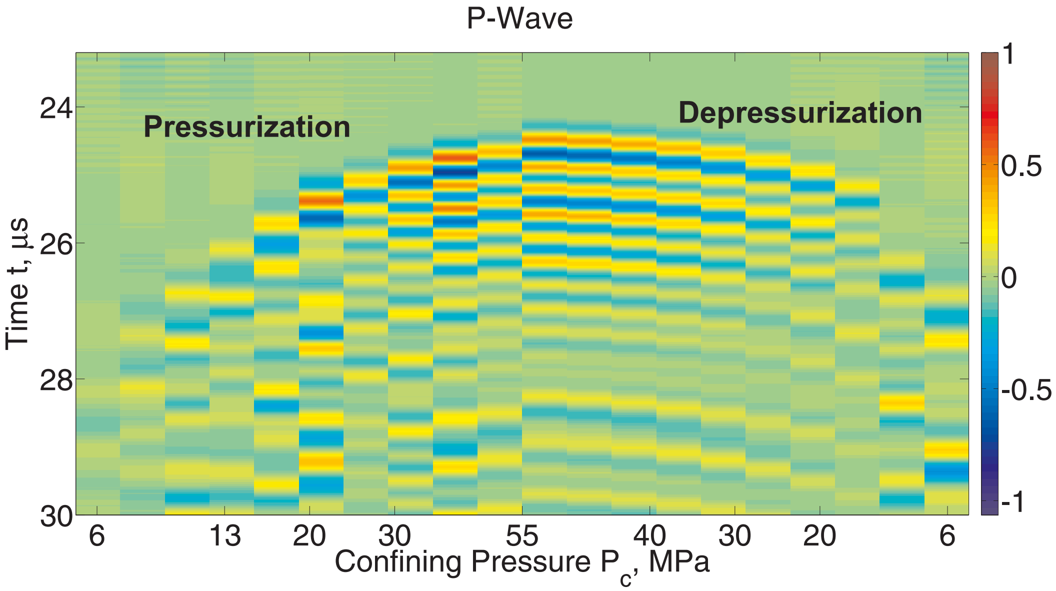

(b)

Figure 5.7: Normalized (a) P -wave obtained under dry conditions at high temperature as a function of confining pressure and (b) is the colored amplitude plot for P- waveform for Vif type of Fontainebleau sandstone.

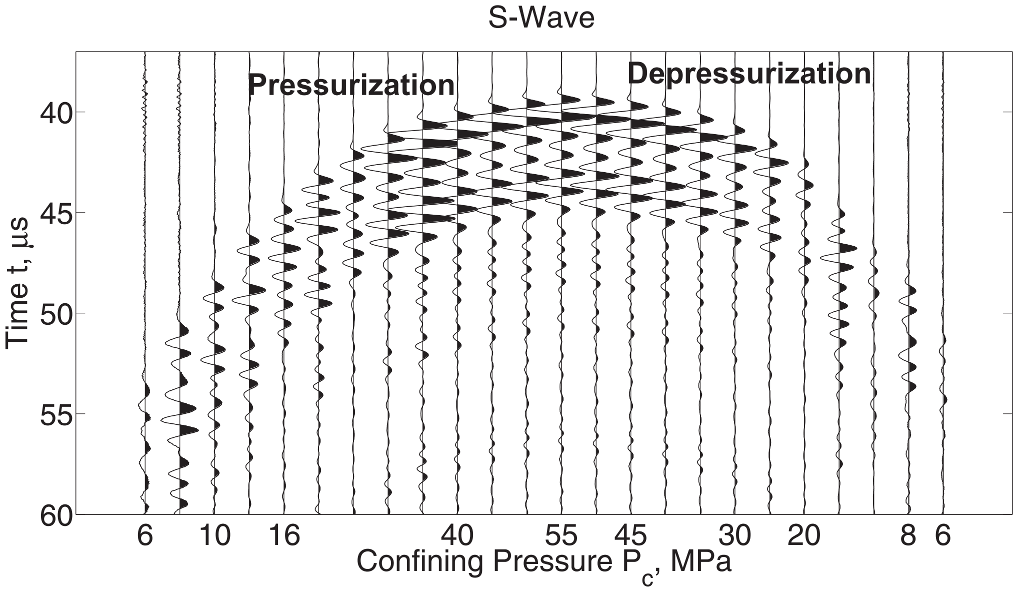

(a)

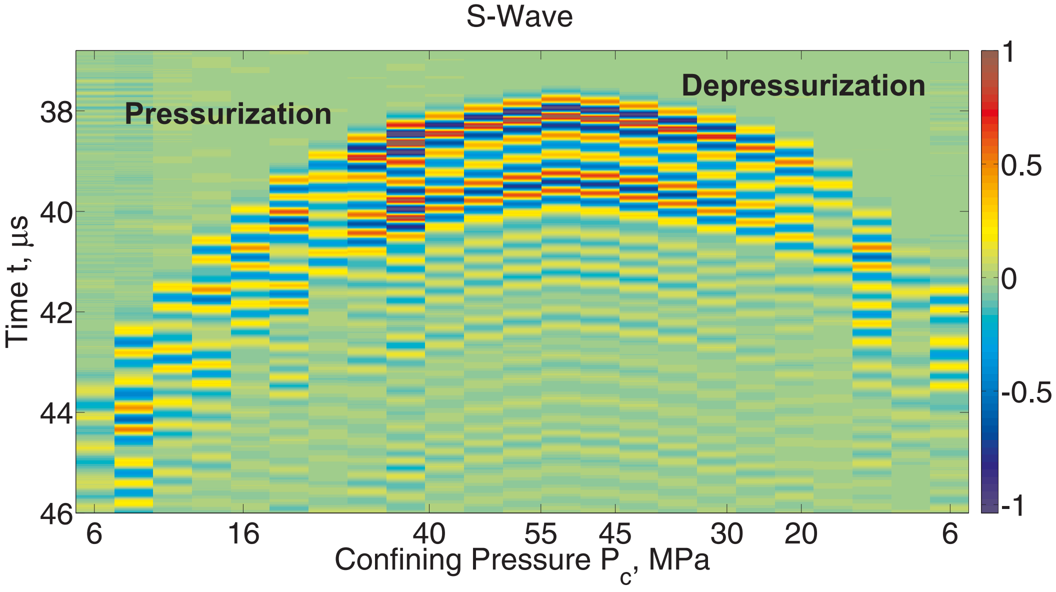

(b)

Figure 5.8: Normalized a) S-wave obtained under dry conditions at high temperature as a function of confining pressure) and b) is the colored amplitude plot for S-waveform of Vif type of Fontainebleau sandstone.

Moreover, we see some asymmetry of the first arrival for both P-and S-waves; the first arrivals are earlier during the depressurisation cycle than the pressurisation cycle for the same pressure. In terms of amplitude strength, we see comparatively stronger amplitudes during the depressurisation than the pressurisation cycle. Because of the opening rate of pores and micro-cracks are slower than the closing rate, the strength of signal increases in the time of down-cycle of the pressure.

5.1.2 Dry Wave Velocities with Nitrogen saturated case

Figures 5.9 and 5.11 show the P-and S-wave velocities for Franc and Vif type Fontainebleau sandstone, respectively, with their corresponding error for dry conditions where P- and S-wave velocities under the nitrogen saturation condition in room temperature are also included to see the relative change in wave velocities for both cases. With pressure change we see a nonlinear variations in wave velocities for dry room temperature measurements while nitrogen saturation situation gives almost linear changes in P- and S- wave velocities with the change of confining pressures. But at high pressure ($>$ 40 MPa) in the case of room temperature dry condition the change in wave velocities become linear. We see a less than 1% increment of wave velocities in the range of 40 MPa to 55 MPa confining pressure for both pressurized and depressurized cycle. Moreover, P- and S-wave velocities during the depressurization cycle are always higher than the pressurization period for the dry run conditions. From the SEM images of both samples (Chapter 4) we noticed the presence of micro-cracks. So this hysteresis behaviour can be attributed to the different rate of change of closing and reopening of compliant pores or micro-cracks during the up and down cycle of the confining pressure.

In the conditions of this experiment, Nitrogen gas (N_2) is essentially chemically inert to the minerals in the sample although at the room temperature of 21 ^0C it does become supercritical at 3.52 MPa. However, over the P-T conditions here this supercritical fluid retains low density and bulk modulus and as such retains much the same behaviour as the N_2 gas. Unfortunately, all of the safe and inert gases that might be used, even the noble gases, become supercritical over much the same range of pressures and temperatures, it is difficult to avoid the gas-supercritical phase transition in this zone. That said, the purpose of these tests was, again, to test the validity of the differential effective pressure relations and to evaluate the changes in the wave speeds and waveform character for a gas-like material only.

Figures 5.9 and 5.11 show the P- and S-waveforms observed for these tests conducted at the constant differential pressure of 15 MPa with pore pressures varying from 1 to 12 MPa in concert with the confining pressures of 16 to 27 MPa. The derived wave speeds are compared to the dry runs in Figures 5.9 and 5.11. For the most part the N_2-saturated wave speeds do not vary much as the confining and tracking pore pressure increase, this is expected as the effective confining pressure on the material remains constant. Further, there is little if any hysteresis seen for this case upon depressurization. However, it is interesting to note that there is a detectable decrease of ~0.4% in the P-wave speed with increasing pressure for Franc sample. Njiekak and Schmitt (in preparation) have demonstrated that this decrease can be entirely attributed to the changes in the fluid properties, primarily the density, over this range of pressures. In all, this shows that we do not anticipate the rocks frame properties to substantially vary when the effective (differential) pressure remains constant. This is an important point that is critical to the interpretation of the CO_2 saturated samples.

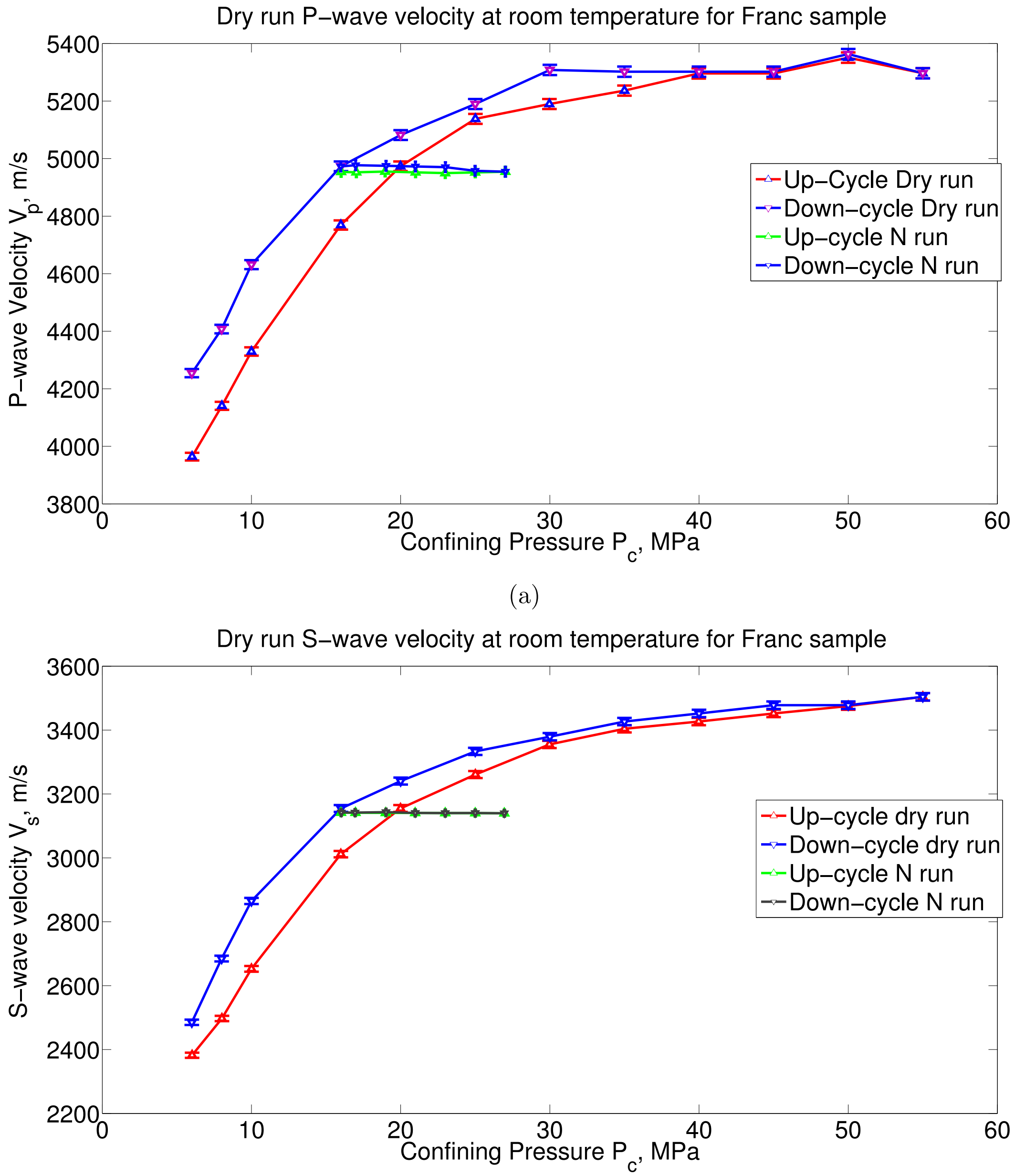

(a)

(b)

Figure 5.9: (a) P -wave velocity and b) S-wave velocity obtained under dry conditions at room temperature along with nitrogen saturated measurements as a function of confining pressure for Franc type of Fontainebleau sandstone.

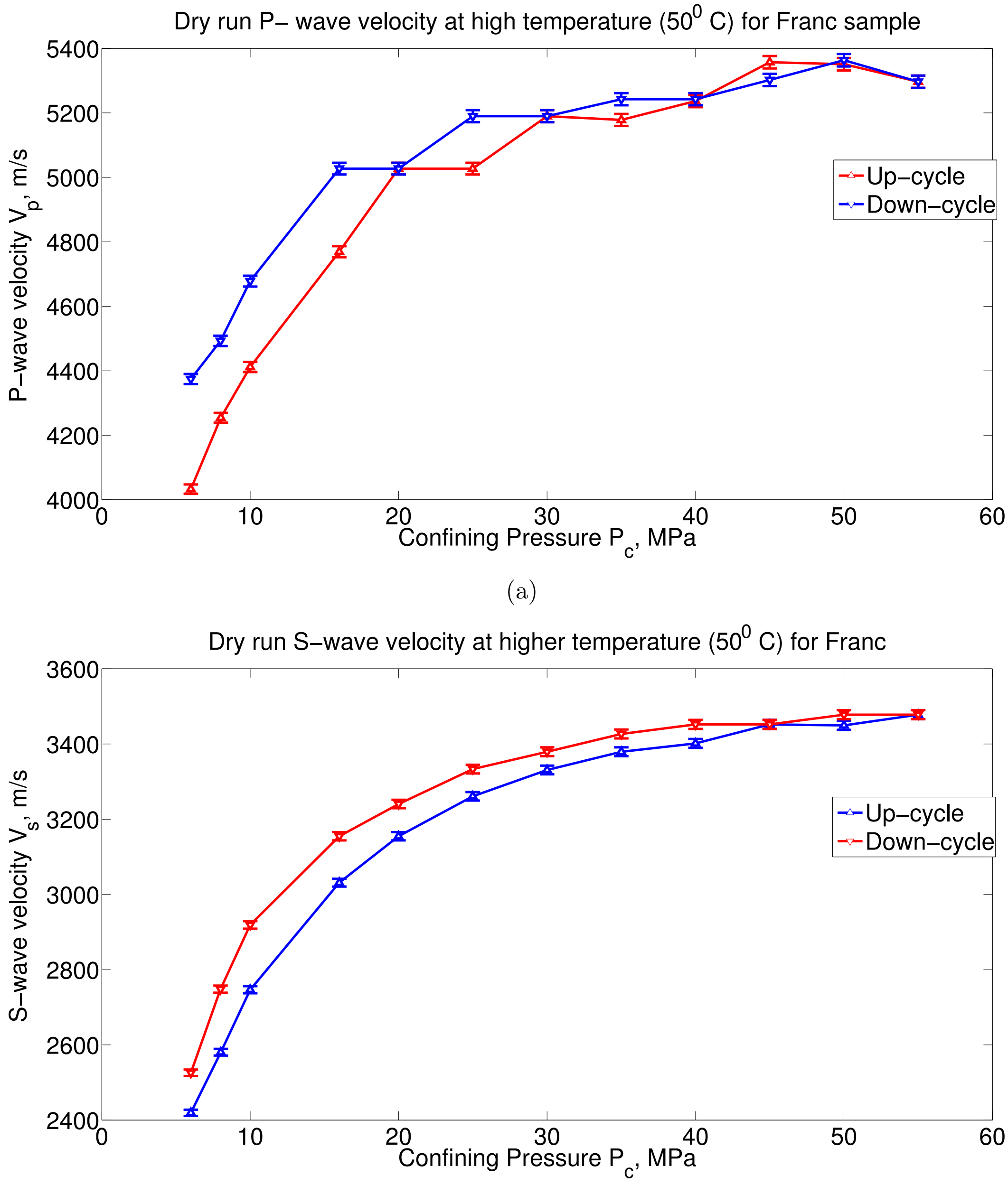

(a)

(b)

Figure 5.10: (a) P -wave velocity and b) S-wave velocity obtained under dry conditions at high (50^0 C) temperature measurements as a function of confining pressure for Franc type of Fontainebleau sandstone.

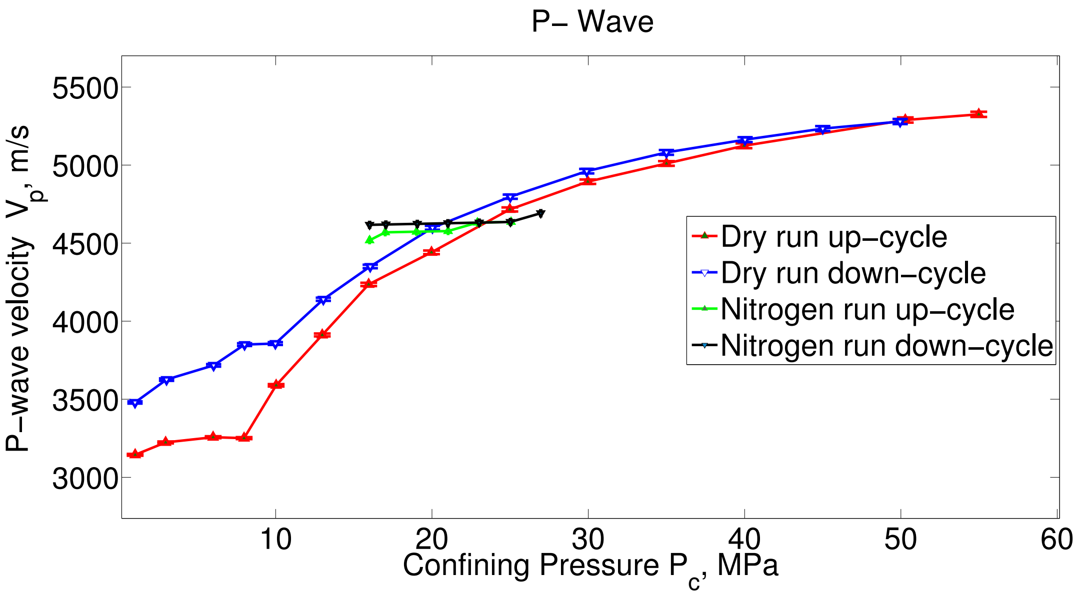

(a)

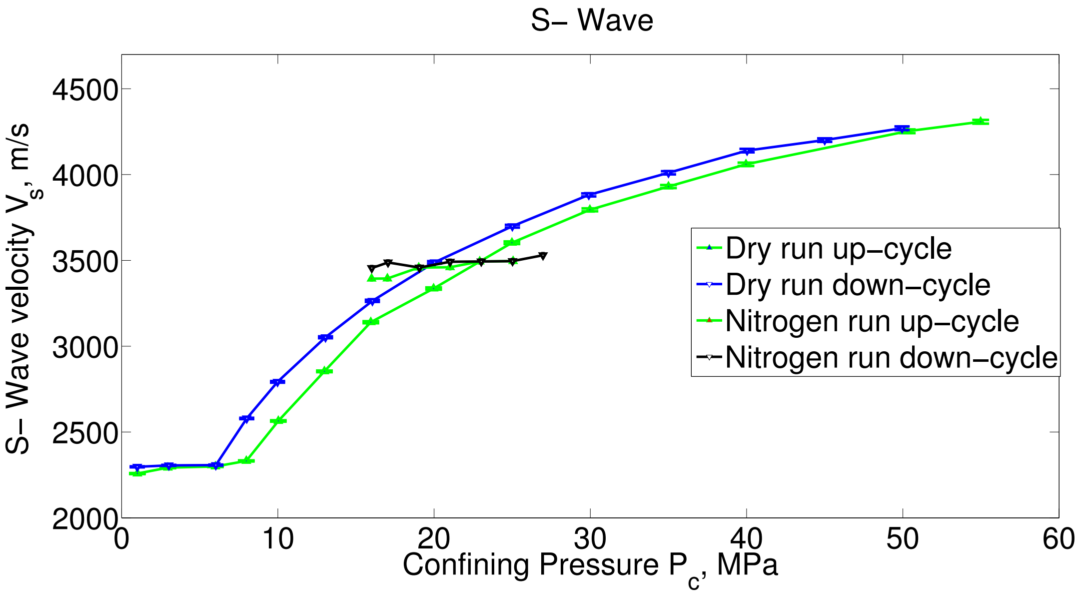

(b)

Figure 5.11: (a) P -wave velocity and b) S-wave velocity obtained under dry conditions at room temperature along with nitrogen saturated measurements as a function of confining pressure for Vif type of Fontainebleau sandstone.

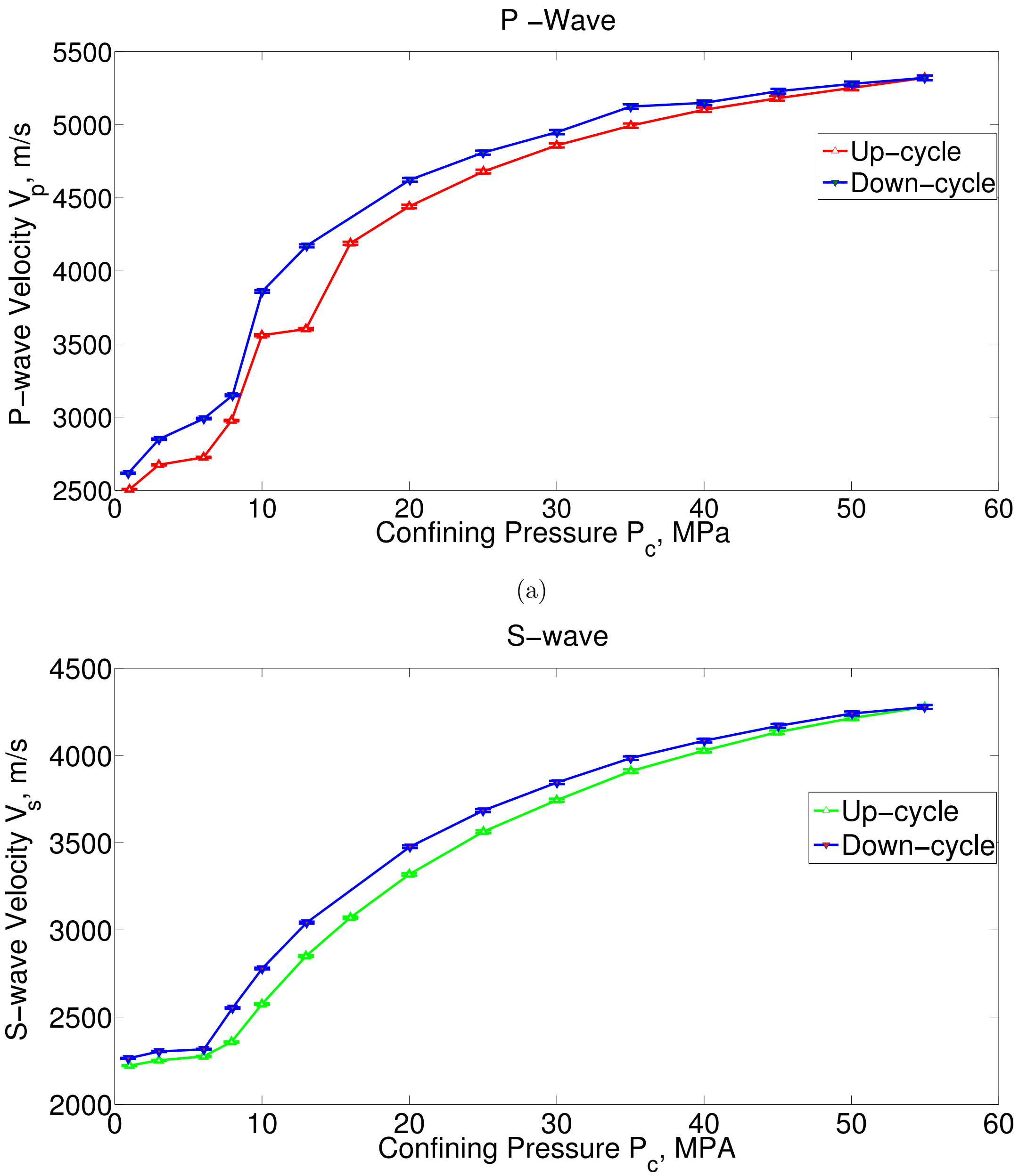

(a)

(b)

Figure 5.12: (a) P -wave velocity and b) S-wave velocity obtained under dry conditions at high (50^0 C) temperature measurements as a function of confining pressure for Vif type of Fontainebleau sandstone.

Figures 5.10 (a) and (b) and 5.12 (a) and (b) represent the P- and S- wave velocity change with the variation of confining pressures in the case of dry runs at the high temperature (50^0 C). Exponential increases of velocities were noted during the up-cycle at lower pressure but at higher pressure the increment become insignificant for both pressurized and depressurized periods. For high temperature measurements we see a slight decrease in velocities for both samples. This effect is not so significant as the thermal expansion coefficient for the Fontainebleau sandstone is very low ($0.55 \times 10^{-6}/^0C$).

5.2 CO_2 saturated measurements

Three different suites of measurements were made under CO_2 saturation: i) constant T = 21^0 C with pore pressure varied, ii) constant T = 50^0 C with pore pressure varied, and iii) constant pore pressure Pp = 8 MPa with temperature varying. As with the N_2 saturated measurements just discussed, these runs are conducted at a constant differential pressure (15 MPa) to minimize any changes in the elastic properties of the rock and maximize any changes in the waveforms due to the pore fluid effects. Figure 5.13 shows the P-T paths for each of these three measurement conditions. These three paths were selected to cross i) the liquid-vapour transition, ii) the vapour-supercritical fluid transition, and iii) the liquid-supercritical fluid transition, respectively. We set the conditions in such a way that the phase transitions for each case would easily be distinguished.

From the dry runs we noted that that confining pressure change influences the waveforms significantly. For this reason we needed to maintain our differential pressure constant during the CO_2 saturated runs. For both low and high temperature runs at low pore pressures CO_2 is in gas state and as pressure in-

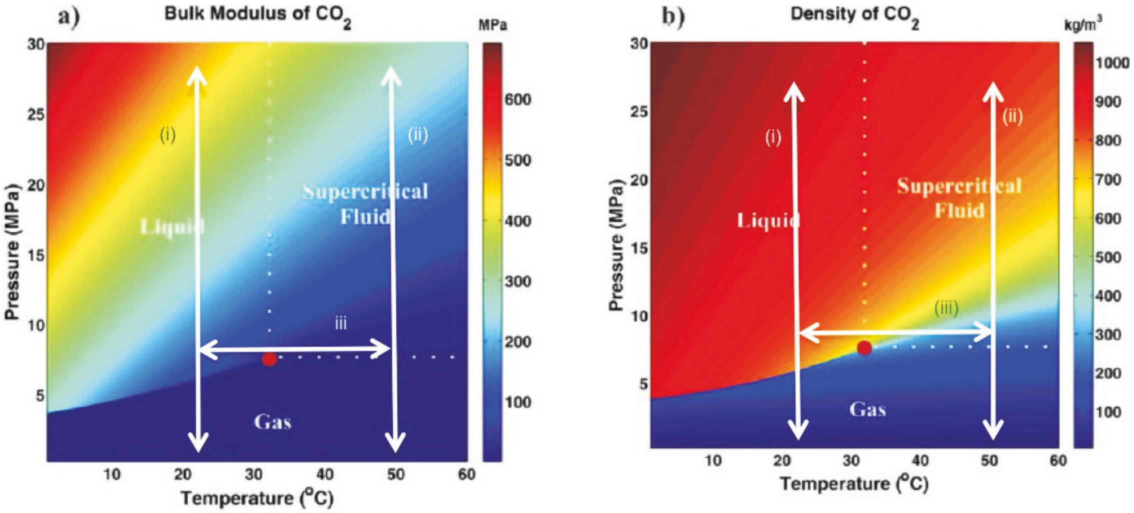

Figure 5.13: Phase diagram of CO_2 a) bulk modulus and b) density. The pressure and temperature conditions applied for the CO_2 saturated Fontainebleau sandstone using the ultrasonic pulse transmission method are shown with the white arrows.

creases CO_2 eventually transforms into a liquid or supercritical fluid state. In the case of constant pore pressure, at low temperatures CO_2 is in liquid and as temperature increases CO_2 eventually transforms into supercritical fluid state.

5.2.1 Waveforms for CO_2 saturated measurements

The three different runs that cross the different phase boundaries are all described separately.

5.2.1.1 Liquid to Gas transition

Figures 5.14 and 5.16 a) and b) show the observed P-wave and S-wave waveforms in a false-color image display. These data were acquired at the constant T= 21^0 C and differential pressure = 15 MPa. The pore pressure was cycled up and down from 1 MPa to 20 MPa during this test for Franc sample but for Vif sample we went one way (high to low pore pressure) in Figure 5.16. The resulting waveforms are plotted as a function of pore pressure and at this temperature they cross the liquid-gas phase transition at 5.868 MPa. There is clear discontinuity in both traveltimes and amplitudes between 5 MPa and 6 MPa as is expected by sharp jump in both the CO_2 density and bulk modulus across this transition. The sharp drop in wave speeds upon the transformation from gas to liquid indicates that the increase in the fluid density is more influential than that of the fluid bulk modulus as has been seen in earlier work [4, 38]. Above the phase transition when the liquid CO_2 saturates the pore space the wave speeds again increase as the fluid bulk modulus rises.

There is an interesting asymmetry to the observed amplitudes that is not completely understood. A large increase in the amplitude is observed across the gas-liquid phase transition on the initial pressurization. The increase is normally what is expected between a gas and a liquid saturated medium. However, the sample retains considerable amplitude through the reversal of this phase transformation upon depressurization. There are differences, too, between the characters of the waveforms for the P-waves and the S-waves. The S-waves show a much larger discontinuous change in amplitude upon reversal (for Franc sample).

5.2.1.2 Gas to supercritical fluid transition

For the gas to supercritical fluid transition investigation, the run was carried out at the constant high temperature (50^0 C) and the same differential pressure of 15 MPa while the pore pressure varied from 1 MPa to 20 MPa. At this temperature CO_2 gas transforms to a supercritical fluid at a pressure of 7.40 MPa. As noted earlier, the gas-supercritical fluid transition is at least a 2nd order phase transition with no discontinuous change in the fluid properties. This lack of variation is apparent in the character of the waveforms in Figures 5.15(a) and (b) and 5.17(a) and (b). In contrast to liquid to gas transition, for the gas to supercritical fluid transition the elastic waves responses to CO_2 's phase transitions are gradual and we do not see any abrupt change. The waveform travel times do increase (i.e. the wave speed goes down) with increasing pore pressure. There appear to be variations in the amplitudes also and, aside from changes at the lowest pressures that may be related to coupling of the transducers, the amplitudes weakly decrease with pore pressure particularly for the shear wave.

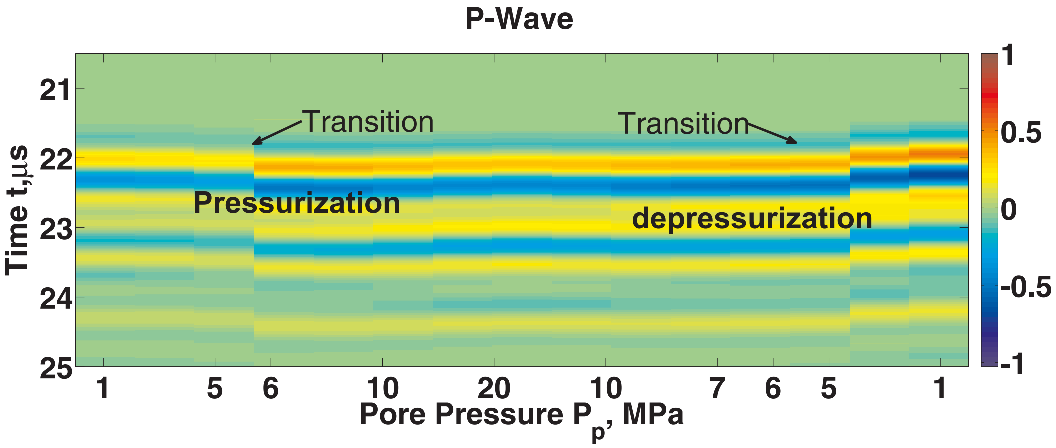

(a)

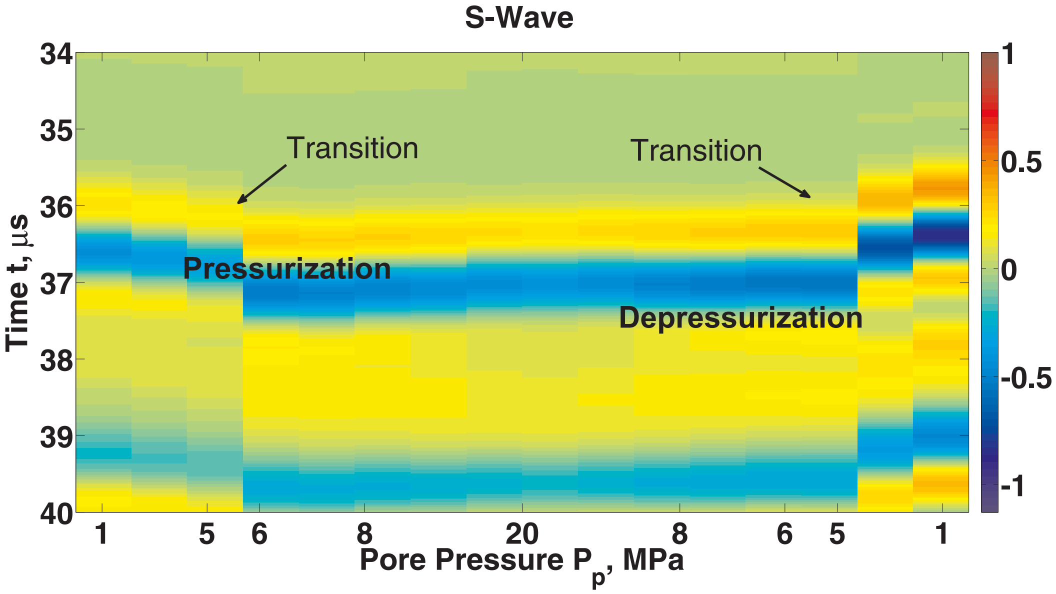

(b)

Figure 5.14: Franc sample normalized (a) P -wave and b) S-waveforms obtained under CO_2 saturation for liquid to gas transition as a function of pore pressure at a $T = 21^0C$.

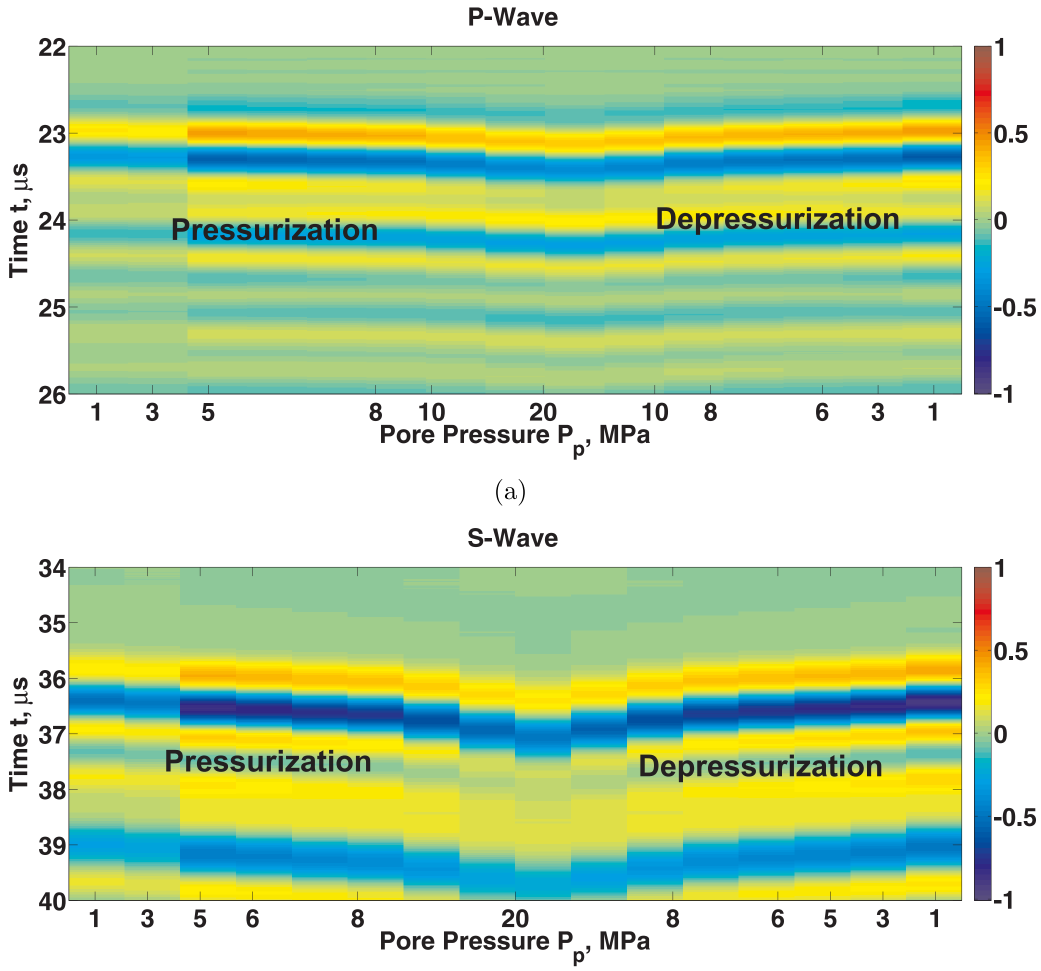

(a)

(b)

Figure 5.15: Franc sample normalized (a) and (b) are the colored amplitude plot for P- and S-waveform for the case gas to supercritical fluid at $T = 50^0C$, respectively.

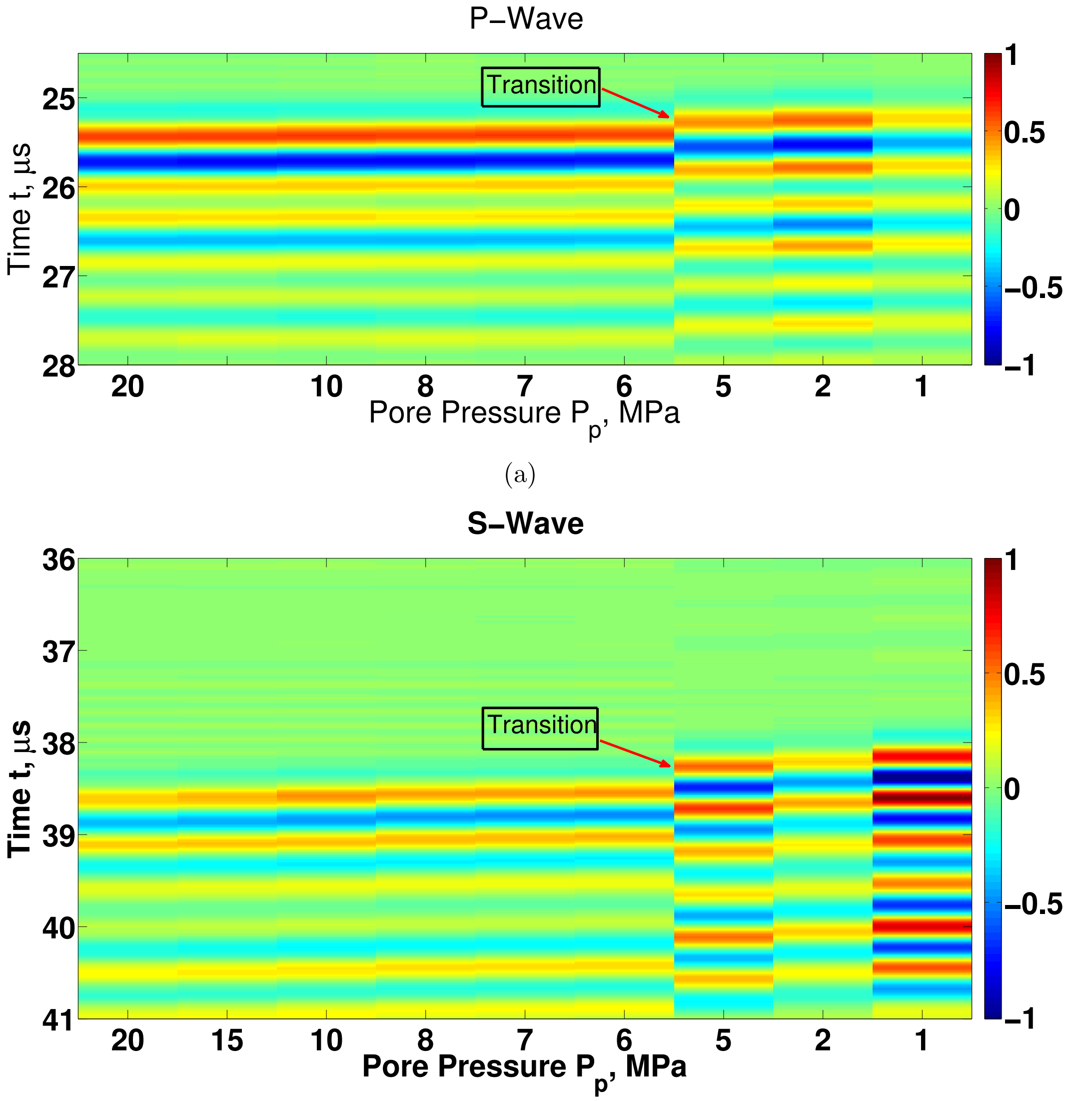

(a)

(b)

Figure 5.16: Vif sample normalized (a) P -wave and b) S-waveforms obtained under CO_2 saturation for liquid to gas transition as a function of pore pressure at a $T = 21^0C$.

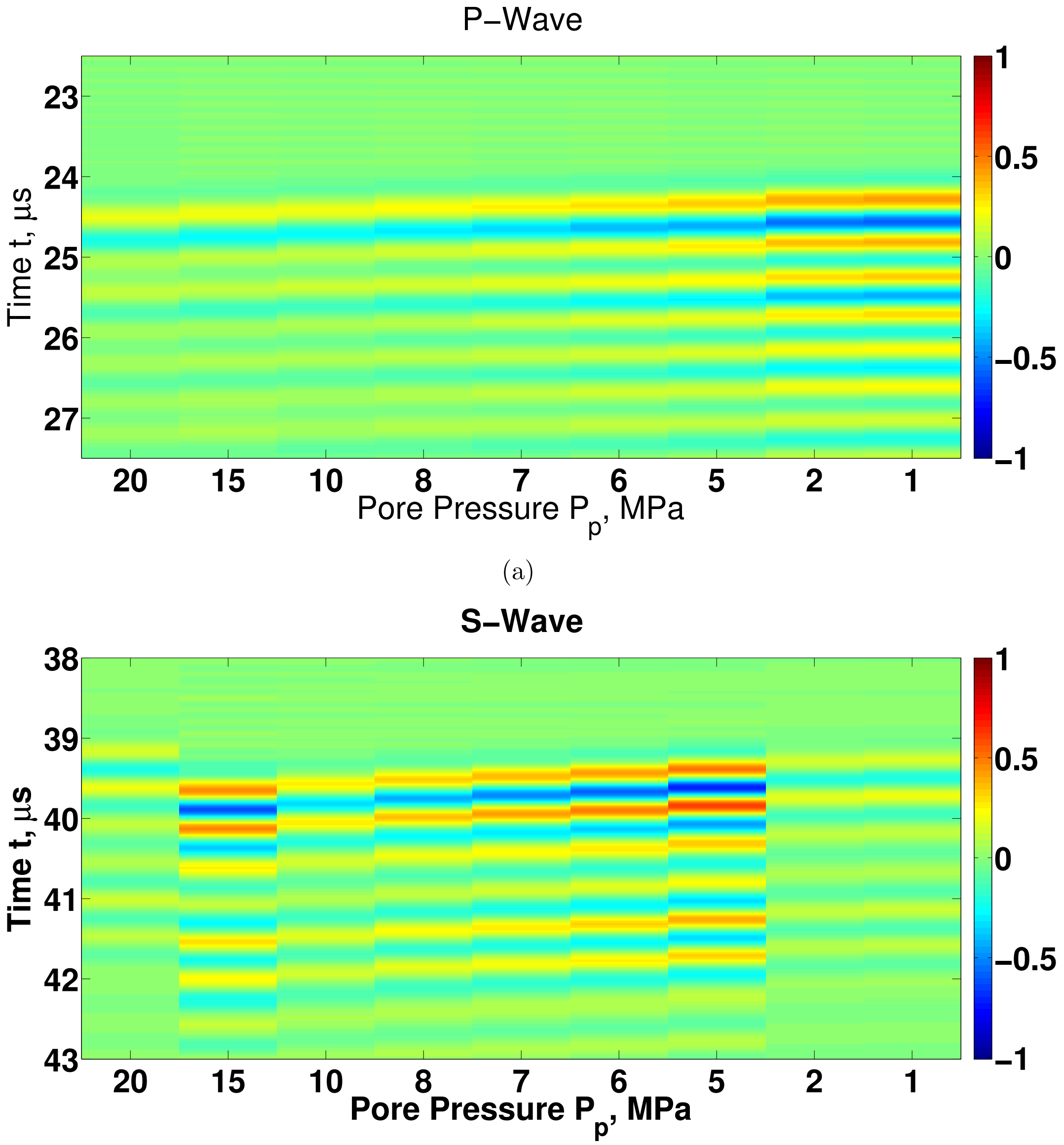

(a)

(b)

Figure 5.17: Vif sample normalized (a) and (b) are the colored amplitude plot for P- and S-waveform for the case gas to supercritical fluid at $T = 50^0C$, respectively.

5.2.1.3 Liquid to supercritical fluid transition

For the transition of liquid to supercritical fluid the pore pressure is kept constant at 8 MPa, which is just above the critical pressures of 7.40 MPa, and consistent with all of our measurements the differential pressure is held constant at 15 MPa, The temperature was varied from 18^0 C to 50^0 C for Franc sample and 21^0 C to 50^0 C for Vif sample with the transition expected at 31^0 C. Figures 5.18 and 5.19 shos the elastic wave responses to CO_2's phase transition. In this case the the variations in the waveforms are are gentle with no sudden changes seen around the transition temperature (31^0 C). Here only the measurements for cooling case only because heating and cooling cycles give almost the same result. Both P-wave and S-wave gives the same kind of phenomenon. There is almost no change in the early arrival times for traces as the temperature increases from the low to high. The change in the strength of the signals is also minor.

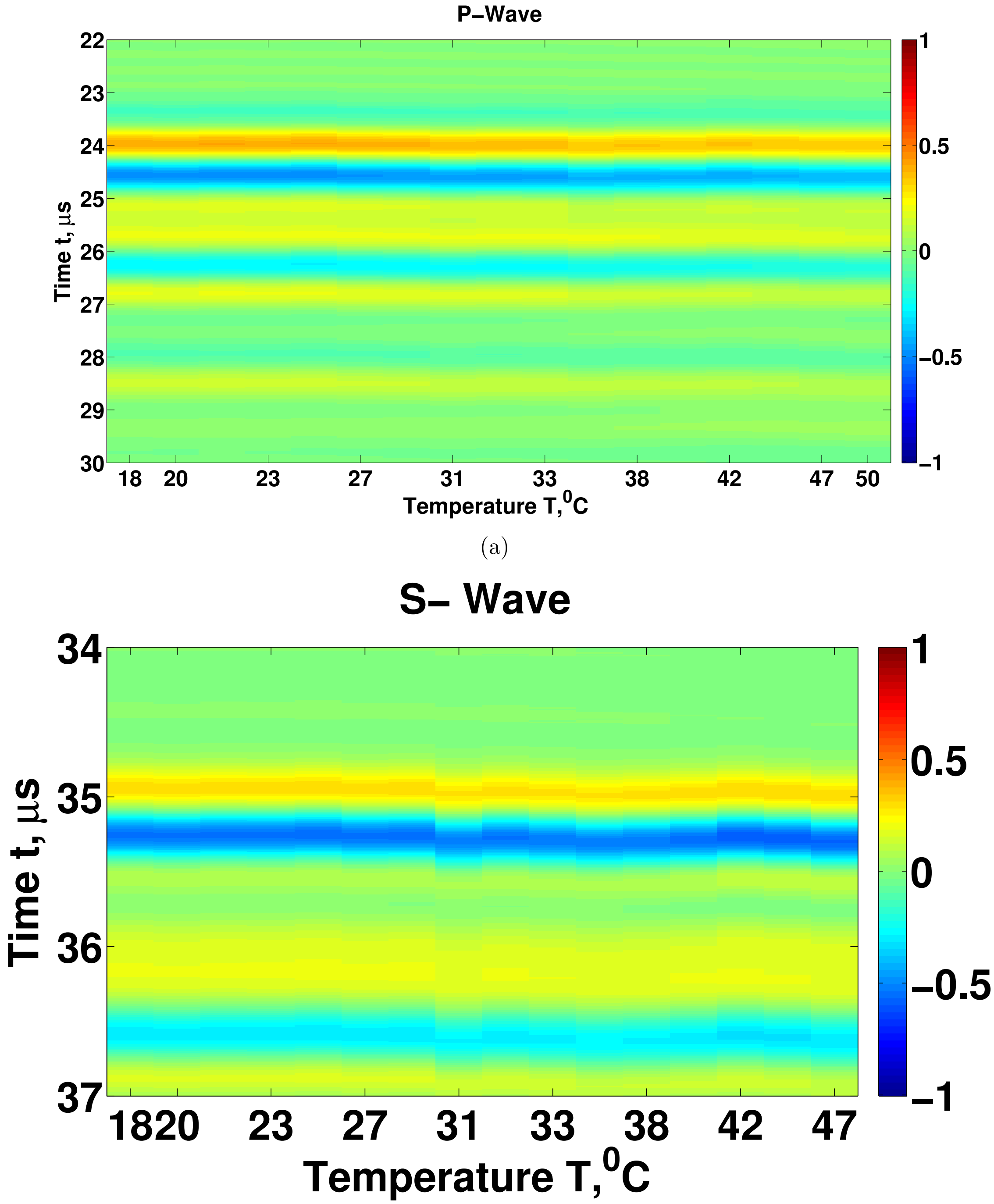

(a)

(b)

Figure 5.18: Franc sample normalized (a) and (b) are the colored amplitude plot for P- and S-waveform for the case liquid to supercritical fluid as a function of temperature with constant pore pressure at 8 MPa, respectively.

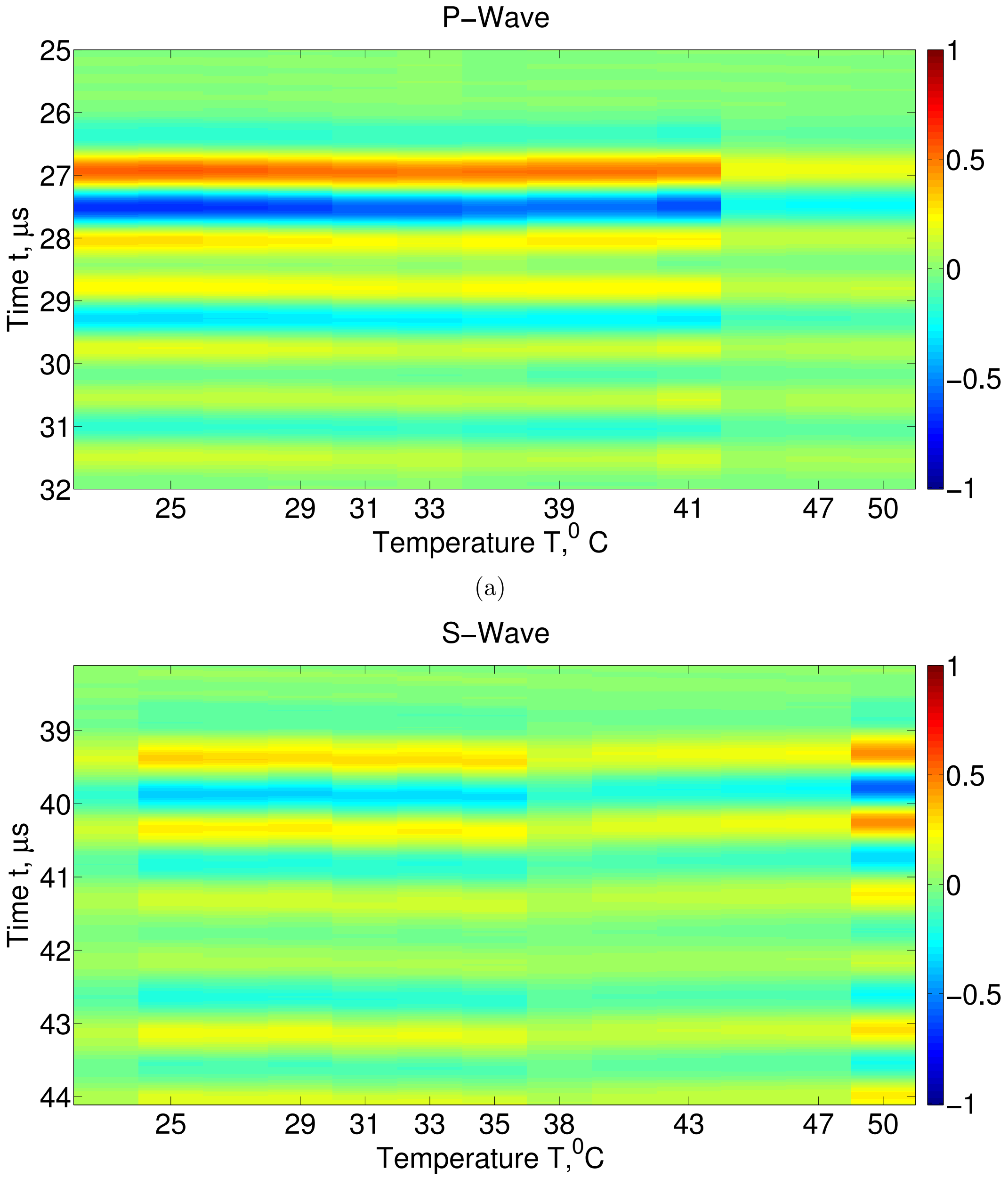

(a)

(b)

Figure 5.19: Vif sample normalized (a) and (b) are the colored amplitude plot for P- and S-waveform for the case liquid to supercritical fluid as a function of temperature with constant pore pressure at 8 MPa, respectively.

5.2.2 Wave velocity of CO_2 saturated cases

The wave speeds obtained from the observed suites of waveforms above are determined using the procedures described in Chapter 2. Here we present and discuss these on a case by case basis. The section following this will then compare the observations to different theoretical models.

5.2.2.1 Liquid to Gas transition

Figures 5.20 a) and b) and 5.21 a) and b) give the P-wave and S-wave velocity of Franc and Vif sample, respectively, with their estimated errors for constant low temperature (21^0 C) CO_2 saturated run in the case of liquid to gas transition at constant 15 MPa differential pressure. The dry run velocities for the same condition and confining pressure are lower than the both P-wave and S-wave velocities of liquid to gas transition scenario.

Both the bulk modulus and the bulk density of CO_2 affects the P-wave velocity. The S-wave velocity is only affected by the variation of bulk density which increases with pressure and consequently results in a decrease in the wave speed. Contrarily the S-wave velocities at low pore pressures show higher velocity than the dry run that implying that the sample has changed in between the measurements. A behavioural hysteresis is also presents for the pressurization and depressurization cycles for the both P-wave and S-wave velocities.

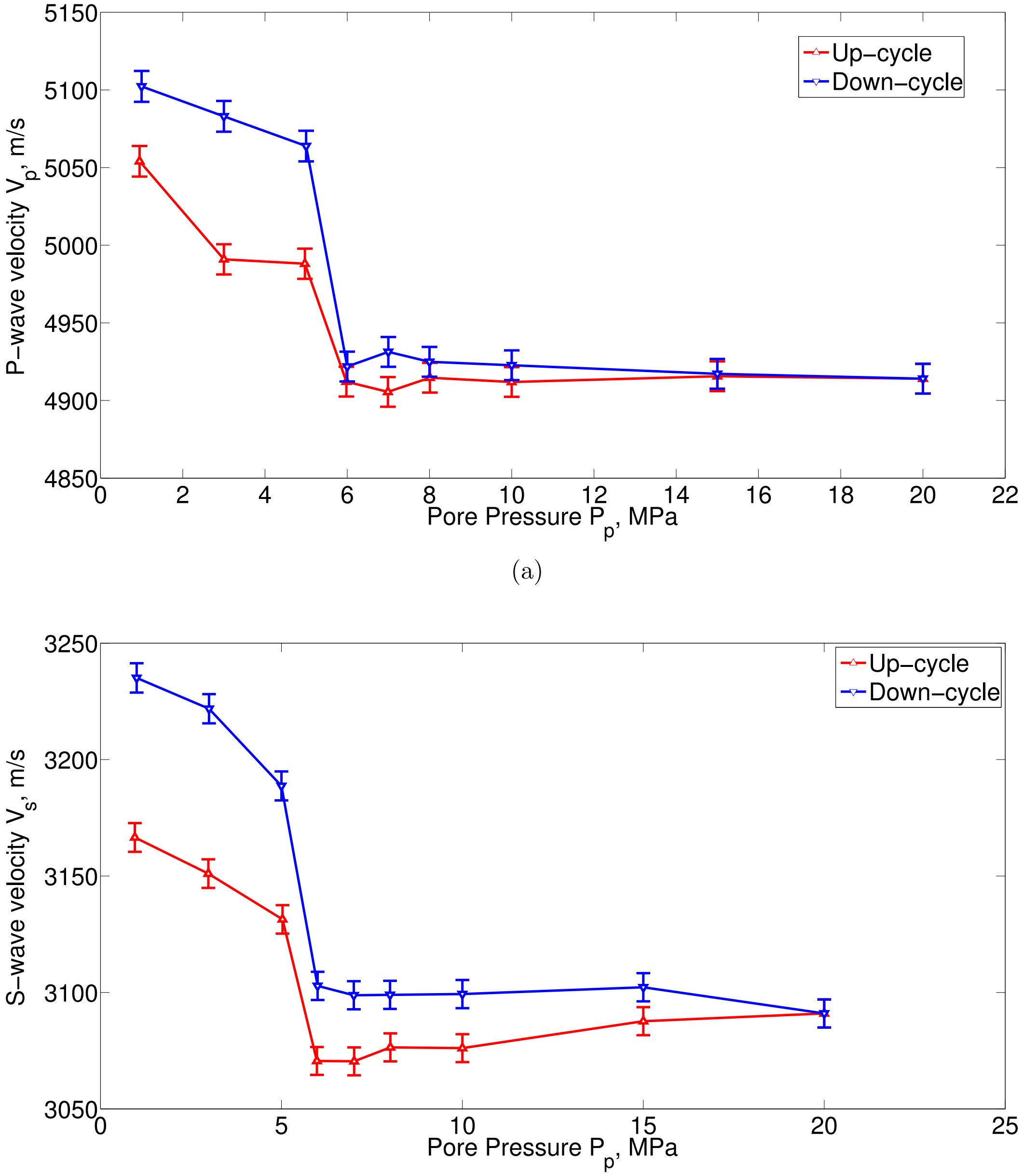

(a)

(b)

Figure 5.20: Franc sample normalized (a) and (b) are the P- and S-wave velocities with their corresponding errors obtained under CO_2 saturation for liquid to gas transition as a function of pore pressure with constant low temperature (21^0 C).The transition is expected to happen at 5.868 MPa.

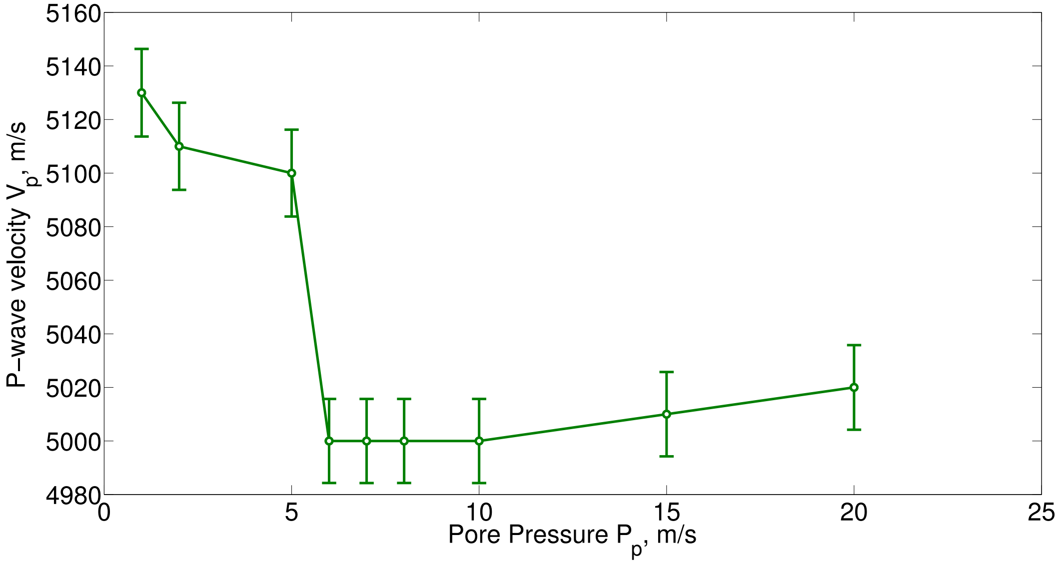

(a)

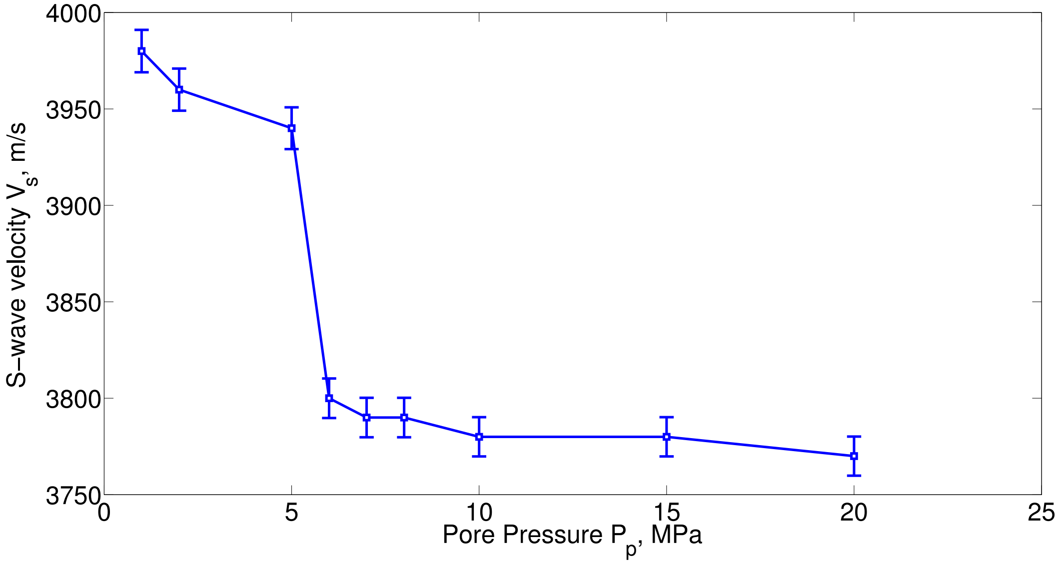

(b)

Figure 5.21: Vif sample normalized (a) and (b) are the P- and S-wave velocities with their corresponding errors obtained under CO_2 saturation for liquid to gas transition as a function of pore pressure with constant low temperature (21^0 C).The transition is expected to happen at 5.868 MPa.

As the pore pressure increases, the wave velocities generally decrease. The exception is shown for the P-wave case where after the transition the velocity trend to increase little bit for Franc sample In contrast, the velocities remain nearly unchanged after the transition for both P- and S -wave. The phase transition for the gas to liquid is obvious for both P-wave and S-wave indicating an immediate and large drop in wave velocities around their respective vapour pressure (the pressure indicate the transition of gas to liquid at a given temperature). The wave velocity declines gradually up to the phase transition. For Franc sample on the initial pressurization, the wave speeds discontinuously drop by 1.5% and 1.9% for P-wave and S-wave, respectively, but upon release of the pore pressure and reversal of this transition during depressurization the waves speeds jump by 2.9% and 2.8% for P- and S-wave, respectively. In the case of Vif sample we see a overall 2.14% and 5% decrease for P-wave and S-wave velocities respectively.

To summarize this run, a sharp change in the wave speeds is observed at the gas-liquid phase transition, that should occur at 5.868 MPa in pure bulk fluid. The shear wave speed shows a substantial increase with pore pressure above this transition pressure. Finally, the shear wave speed displays a significant hysteresis during depressurization. We will attempt to rationalize these observations in the coming section on modelling.

5.2.2.2 Gas to supercritical fluid transition

The Figures 5.22 a) and b) and 5.23 a) and b) give the P - and S-wave velocities, respectively, across gas to supercritical fluid transition at a constant temperature of 50^0 C that is well above the critical temperature of 31^0 C. Again, this transition should take place at the critical pressure of 7.4 MPa. The behavior of the observed wave speed curves here contrast markedly with that for the just presented gas-liquid transition. Only a gradual variation of 2.7-3.1% and

3.9-4.2 % for the P- and S-wave velocities exists across this entire range of pore fluid pressures for Franc sample. The P-wave velocities display little, if any, hysteresis, and with the pressurization and depressurization curves almost stays in the range of uncertainty limits. In the case of the S-wave a small hysteresis exists between the pressurized and depressurized cycles. On the other hand, the Vif sample shows a gradual change of 1.97% and 2.02% for P- wave and S- wave, respectively. As the gas-supercritical phase transition is of 2nd order with no discontinuities in the properties, these gradual changes are not unexpected.

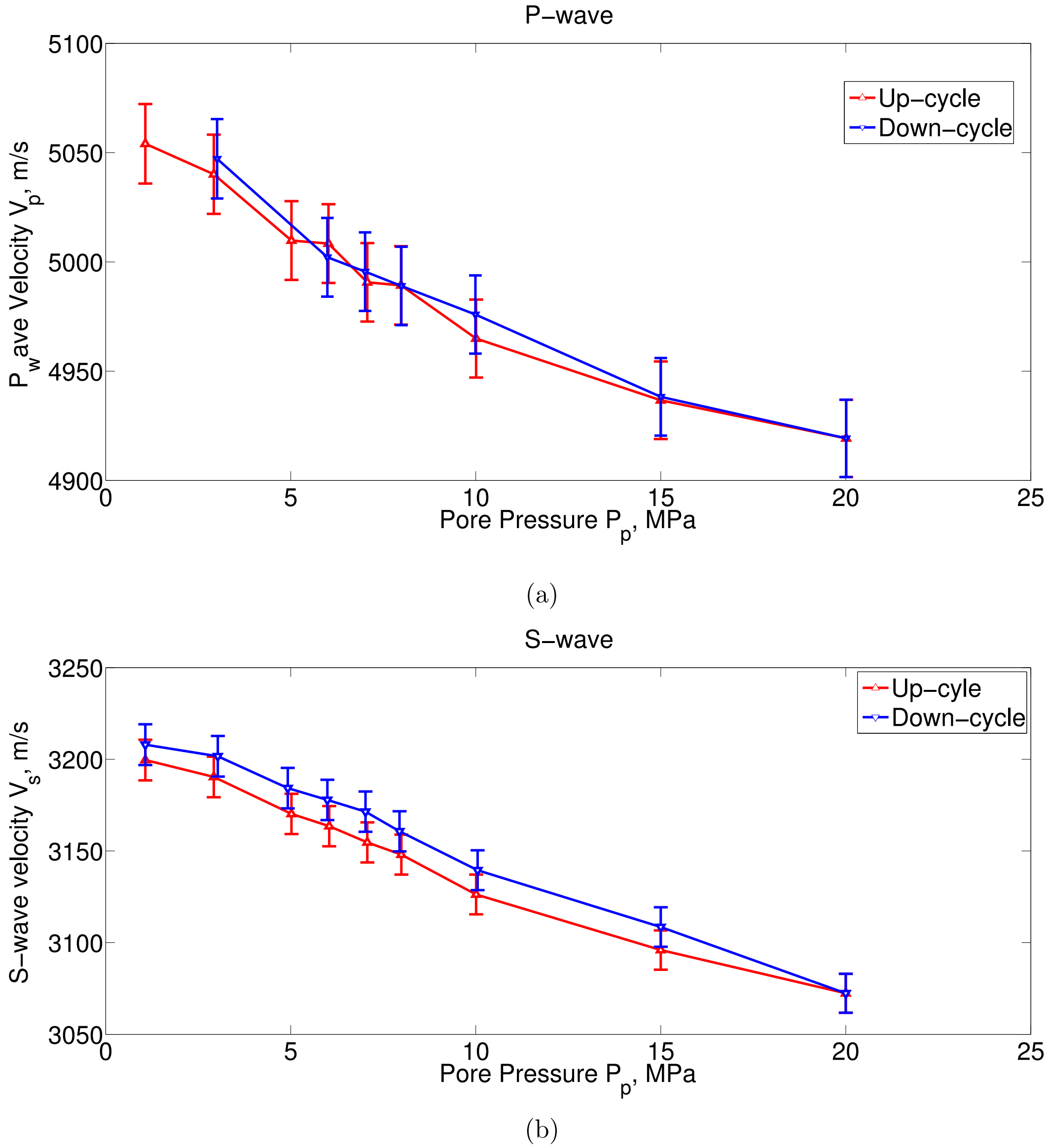

Figure 5.22: Franc sample normalized (a) and (b) are the P- and S-wave velocities with their corresponding errors obtained under CO_2 saturation for gas to supercritical fluid transition as a function of pore pressure with constant high temperature (50^0 C). The transition occurs at 7.40 MPa.

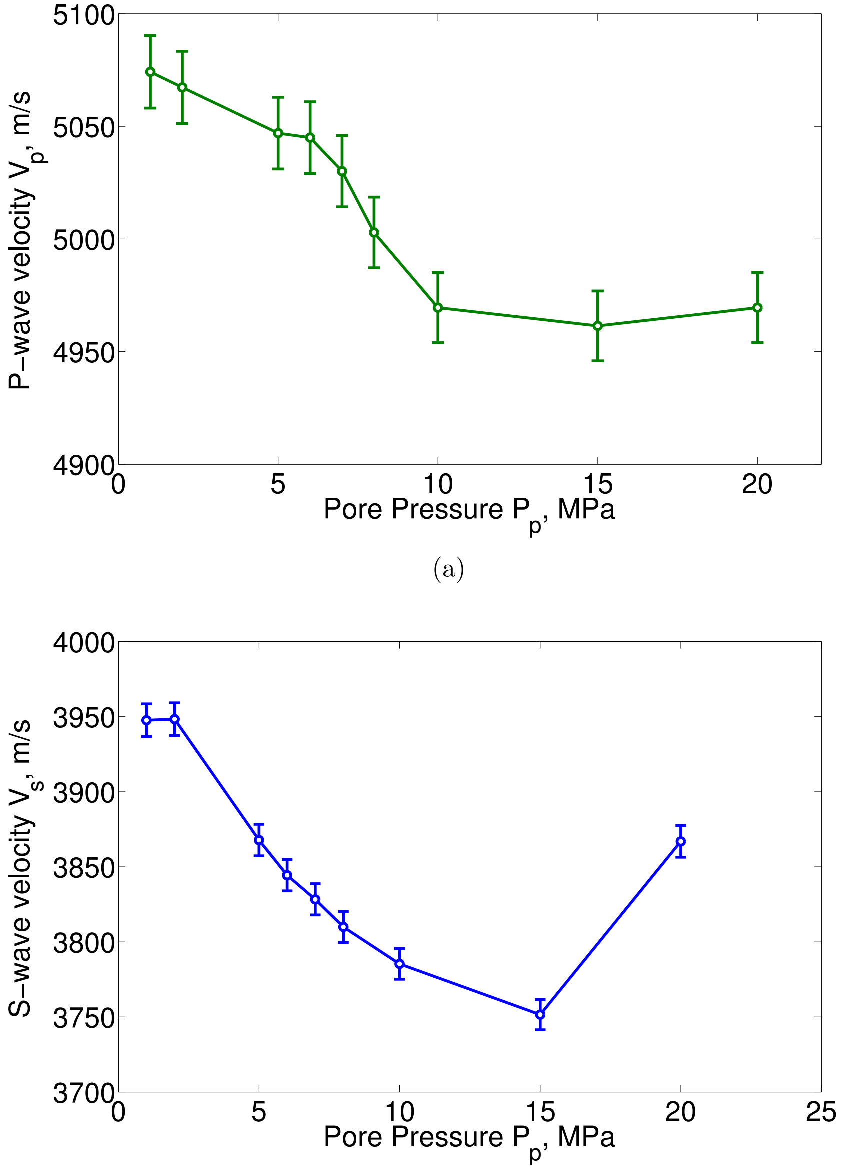

(a)

(b)

Figure 5.23: Vif sample normalized (a) and (b) are the P- and S-wave velocities with their corresponding errors obtained under CO_2 saturation for gas to supercritical fluid transition as a function of pore pressure with constant high temperature (50^0 C). The transition occurs at 7.40 MPa.

5.2.2.3 Liquid to supercritical fluid transition

Figures 5.24 a) and b) and 5.25 a) and b) show the P-wave and S-wave velocity with their corresponding errors for the liquid to supercritical transition, respectively. The change in wave velocity is gradual in the whole run. Over the entire measurement we noticed an overall decrease in wave velocity of only 1.19 % and 0.69 % in P-wave and S-wave, respectively, during the investigated temperature interval. The phase transition is not apparent at all in the wave speeds; moreover, we see a smooth velocity variation without any abrupt change in the trend. The up-cycle and down-cycle also do not show any significant hysteresis as both are in the range of error of each other. In the case of Vif sample we see the same trend with a gradual change in velocities of 1.19 % and 1.05% for P-wave and S-wave, respectively.

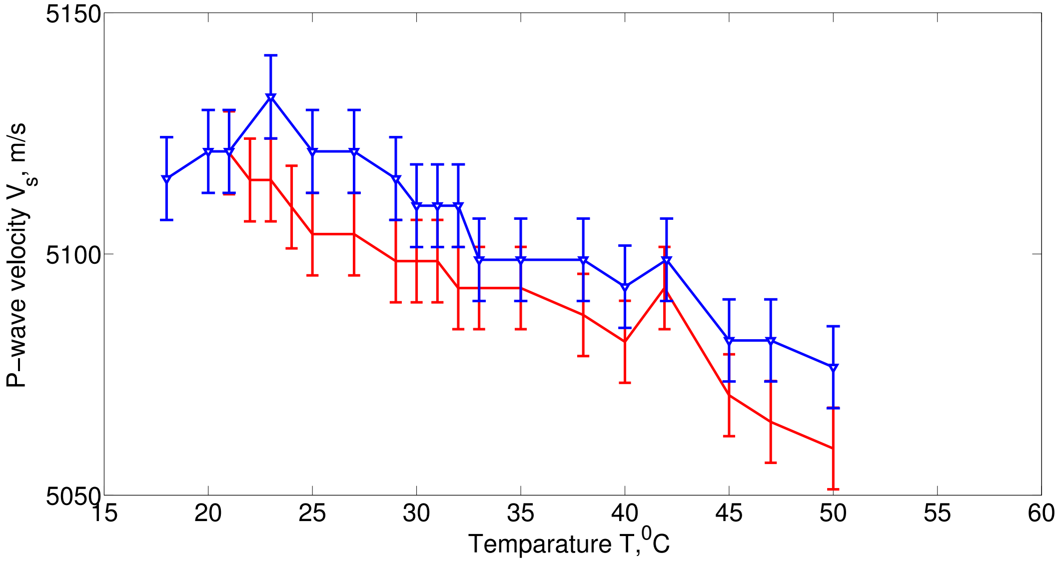

(a)

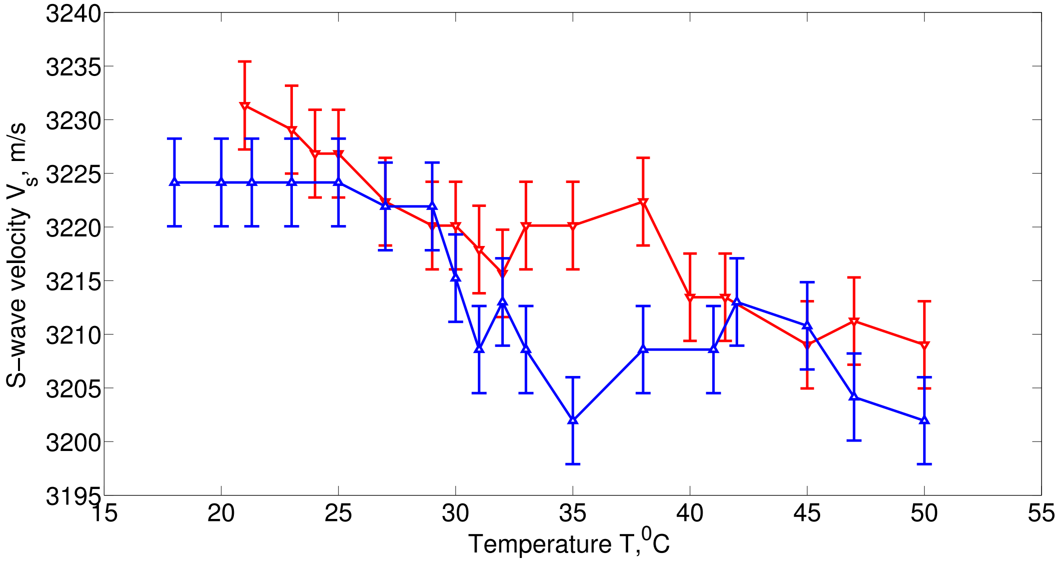

(b)

Figure 5.24: Franc sample normalized (a) and (b) are the P- and S-wave velocities with their corresponding errors obtained under CO_2 saturation for liquid to supercritical fluid transition as a function of temperature with constant pore pressure ($P_p = 8MPa$). The transition occurs at 31^0 C.

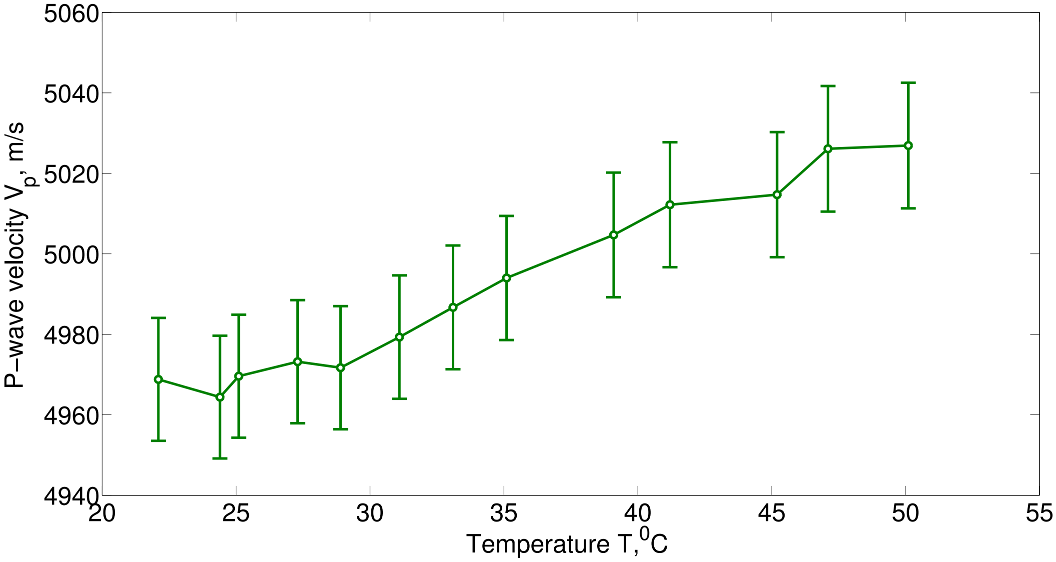

(a)

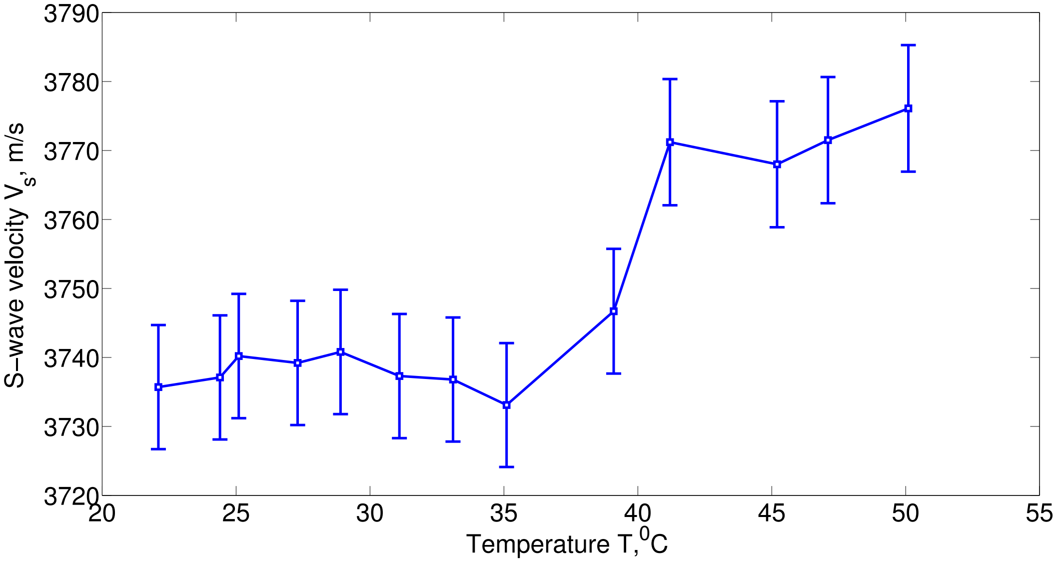

(b)

Figure 5.25: Vif sample normalized (a) and (b) are the P- and S-wave velocities with their corresponding errors obtained under CO_2 saturation for liquid to supercritical fluid transition as a function of temperature with constant pore pressure ($P_p = 8MPa$). The transition occurs at 31^0 C.

5.3 H_2O saturation

Measurements were carried out on the Franc sample only under water saturated conditions. The sample was kept at constant room temperature of 21^0C and differential pressure of 15 MPa. The pore pressure increased from 1 MPa to 25 MPa.

5.3.1 Waveforms

The waveforms for P- and S-wave are shown in Figure 5.26 for the full water saturated measurements. There is no significant changes noticed for either of the P- and S- wave signals and travel times. The amplitudes, too, show little variation.

5.3.2 Water saturated wave velocities

Figure 5.27 shows the P -and S- wave velocities with error as a function of pore pressure for the water saturated runs calculating from the wave forms shown in Figure 5.26. Both the P and S-wave speeds under these water saturated conditions are significantly larger than those for the dry sample at the effective confining pressure of 15 MPa. We see some increment in both P -and S- wave velocities as the pore pressure increases. At high pore pressures the up-cycle and down-cycle velocities are almost linear while in low pore pressure show some minor variations for pressurised and depressurised cycles. An overall $\sim$ 0.3% velocity change is visible for both P- and S-wave.

5.4 Summary

The ultrasonic pulse transmission method is used to measure the P- and S-wave speeds on Franc and Vif Fontainebleau sandstone samples under dry, N_2 satu-

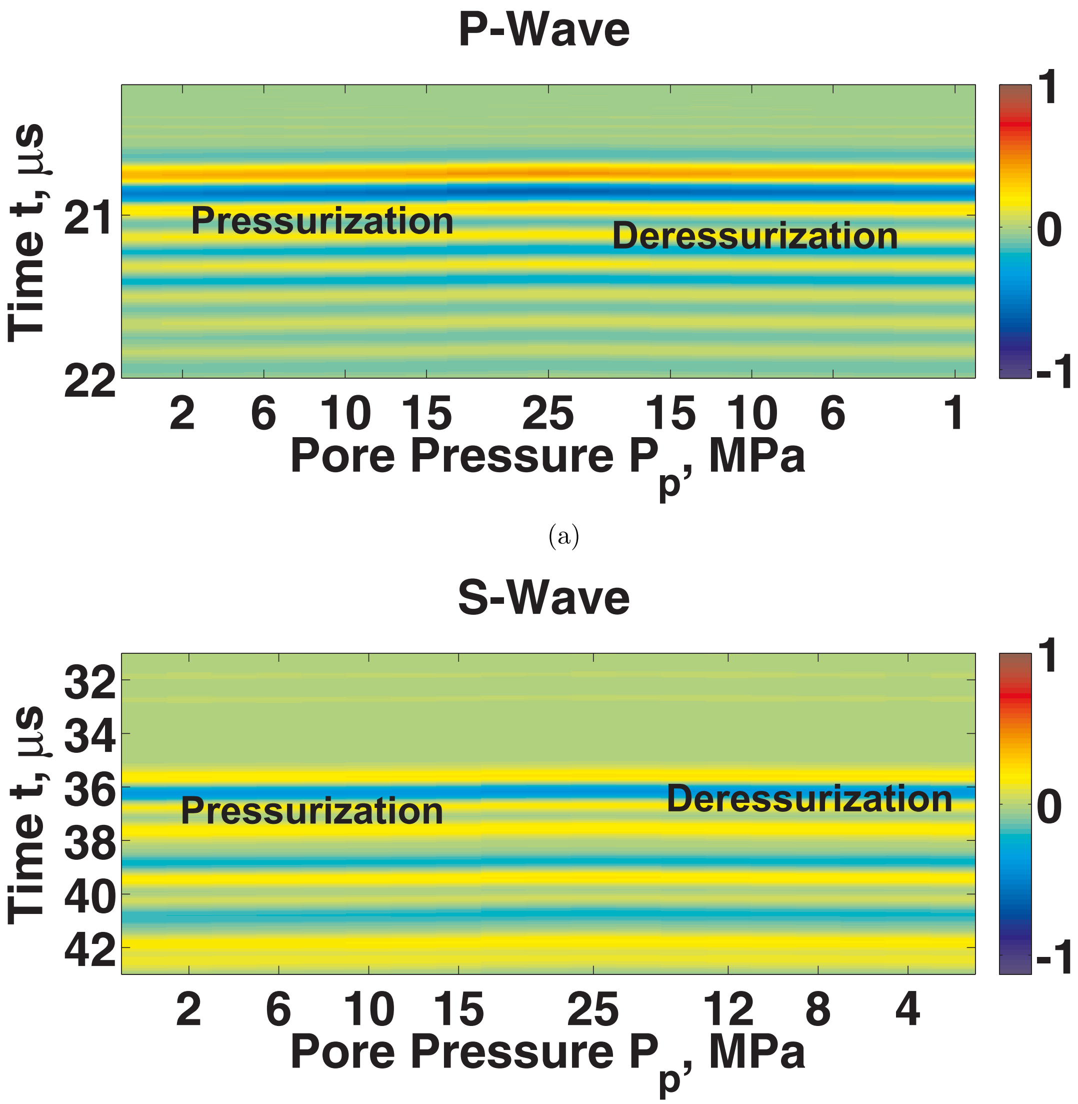

(a)

(b)

Figure 5.26: Normalizeda) P- and b) S- waveforms for fully water saturated runs where the differential pressure is kept constant at 15 MPa at room temperature for Franc sample.

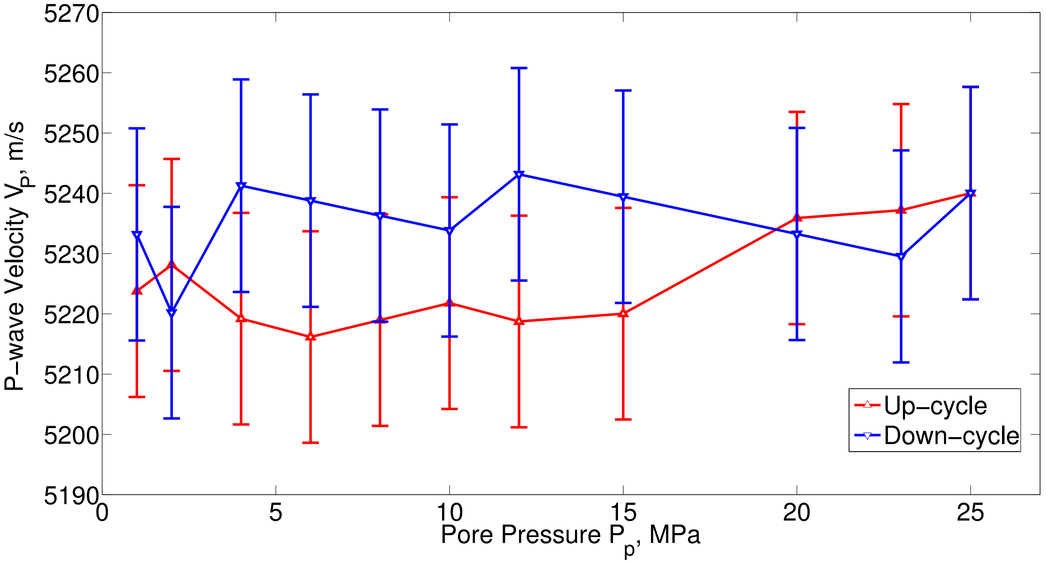

(a)

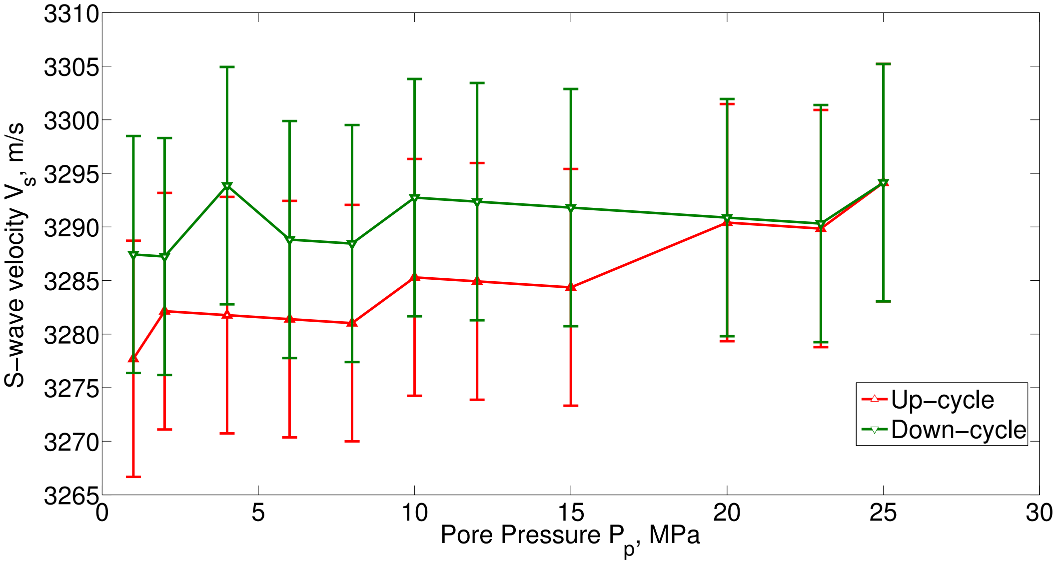

(b)

Figure 5.27: a) P- and b) S- wave velocities with their corresponding errors measured under the water saturation of the sample for various pore pressure at room temperature and constant differential pressure 15 MPa for Franc sample.

rated, CO_2 saturated and H_2O saturated conditions. The P -and S-waveforms with their corresponding velocities were presented for all four saturation conditions. The dry wave velocities displayed substantial pressure dependence under both room and high temperatures. This variation in velocities is due to closing and opening rate differences of the pores and micro cracks of the sample. For nitrogen runs we saw almost unchanged wave velocities for P- and S- wave.

In these experiments, it appears for both the Vif and Franc samples that only the abrupt changes in the wave speeds and densities afforded by the liquid to gas transition may be easily detected using remote seismic methods. The changes in the properties associated with the 2nd order phase transition of liquid to supercritical or gas to supercritical both are much smoother and likely more difficult to detect. We will study these changes in reflectivity more quantitatively in the coming chapters.

Chapter 6

Models and observations: a comparative discussion

In this chapter at first we will present how the density, bulk modulus and the viscosity of the fluids N_2, CO_2 and H_2O change over the ranges of our experimental conditions.Then we will develop the fluid saturations models of Gassmann and Biot, which we already discussed in chapter 2, using the same pressure and temperature conditions used for the lab experiments. To carry out calculations with these two models we need to know a number of sample and fluid properties. Table 6.1 shows some of the parameters for both samples that we used to establish these two models. The bulk modulus, the density, the fluid viscosity of N_2, CO_2 and H_2O were taken from the NISTs online chemistry webBook [http://webbook.nist.gov/chemistry/], from Bass [103] we retrieved the density and bulk modulus of the mineral grains, and the bulk modulus of the frame was calculated using the dry run measurements. The bulk density, porosity and tortousity were determined as discussed already in Chapter 3. A comparative discussion on model and observed measurements will be presented at the end of this section.

Property	Symbols	Franc type Fontainebleau	Vif type Fontainebleau
Porosity(%)	ϕ	6.28	12.5
Tortousity (unitless)	τ	7.1	3.7
Permeability (mD)	κ	16.58	16.56
Dry Frame Bulk Modulus (GPa)	K_d	27.95	12.60
Solid Bulk Modulus (GPa)	K_s	37.8	37.8
Solid frame density (kg/m^3)	ρ_s	2640	2647

Table 6.1: Different Parameters for Fontainebleau sandstone samples

6.1 Effect of change in fluid properties under different conditions for N_2, CO_2, & H_2O

One of the main goal of this work is to map out the effect of change of fluid properties and particularly the the phase state of the fluids on ultrasonic wave speeds. To have a good idea of what could happen under a range of different physical conditions, we mapped different physical properties (bulk modulus, density, and viscosity) of each fluid as function of pressure and temperature using the models provided by the NIST Chemistry Webbook programs. Here we will mainly examine the dependency of bulk modulus, fluid density and viscosity with the change of pressures, temperatures and other related parameters. Figures 6.1 and 6.2 show the bulk modulus, fluid density and viscosity dependency for N_2 and H_2O, respectively.

These figures show that the physical properties of these two fluids vary in a simple linear fashion with pressure if the temperature is maintained constant. We expect this gradual change to also transfer through to the corresponding seismic velocities as estiamted by either the Biot or Gassmann models. We will see this effect later in the modelling that follows.

Three different runs were carried out on each of the samples while subject to CO_2 saturation: two at constant temperatures of 21^0C and 50^0C and one at a constant pore pressure of 8 MPa. In all three cases the differential or effective

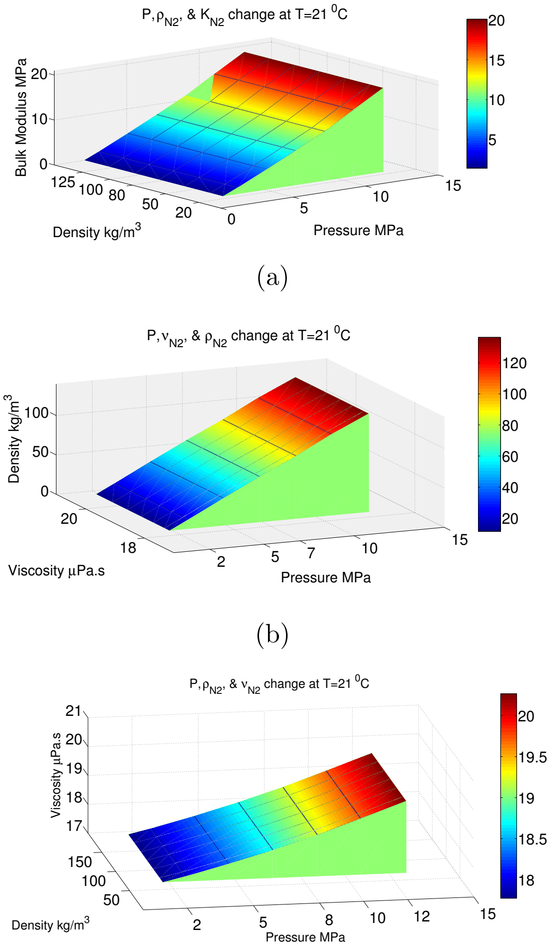

(a)

(b)

(c)

Figure 6.1: Three dimensional representations of the change of the bulk modulus, density, viscosity and pressures of the fluid N_2 at room temperature (T=21 ^0C). Data used here are obtained from NIST chemistry webBook.

pressure was maintaned at a constant 15 MPa. Figures 6.3, 6.4, and 6.5 show the relationships between the various properties with pressure at the constant temperature of 21^0C in a 3D depiction.

Figure 6.3(b) shows the liquid to gas transition case where the temperature and differential pressure was kept constant and pore pressure was changed. Here we see a very sharp change in it rises rapidly from 5 MPa to 6 MPa in pore pressure (the phase transition occurs at 5.686 MPa at this temperature). This change is expected as liquid transforms to gas. Rapid changes are also

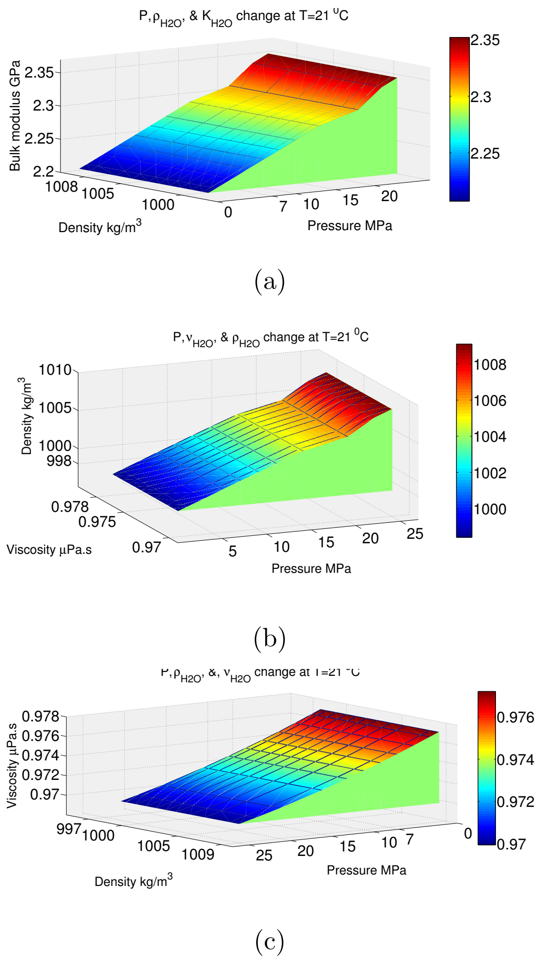

Figure 6.2: Three dimensional representations of the change of the bulk modulus, density, viscosity and pressures of the fluid H_2O at room temperature (T=21 ^0C). Underlying data are obtained from NIST chemistry webBook.

seen for the bulk modulus and the viscosity across this transition.

For gas to supercritical fluid transition in Figure 6.4 (with constant high temperature T=50 ^0C) we do not see a big sudden change for bulk density (Figure 6.4(a)) and density (Figure 6.4 (b)) but a gradual increment in the corresponding parameters. On the other hand, for viscosity (Figure 6.4(c)) around P=7.40 MPa we see a sudden fall as pressure increases which indicate the transition of phases.

Finally, Figure 6.5 that represents the liquid to supercritical fluid transition (constant pore pressure at P=8 MPa and constant differential pressure 15 MPa)

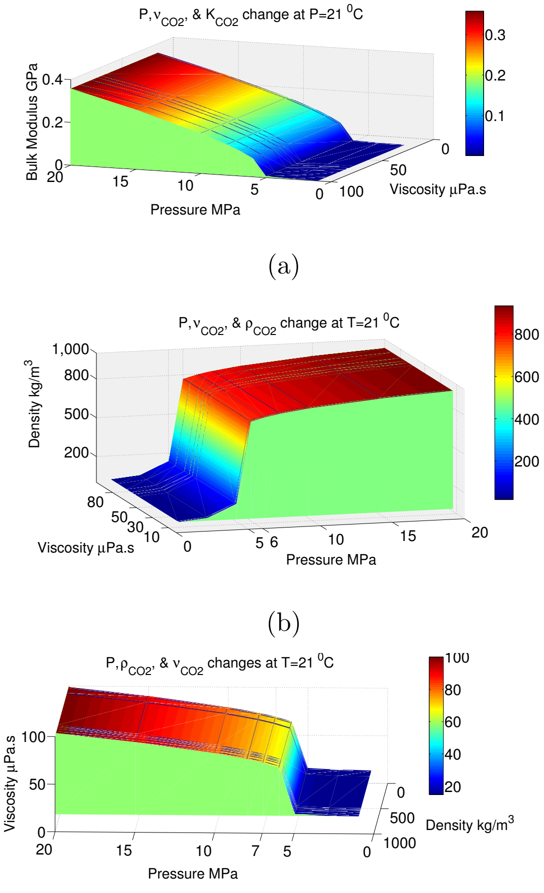

(a)

(b)

(c)

Figure 6.3: Three dimensional representations of the change of the bulk modulus, density, viscosity and pressures of the fluid CO_2 at room temperature (T=21 ^0C) and constant differential pressure showing the vapour to liquid phase transition. Underlying data are obtained from NIST chemistry webBook.

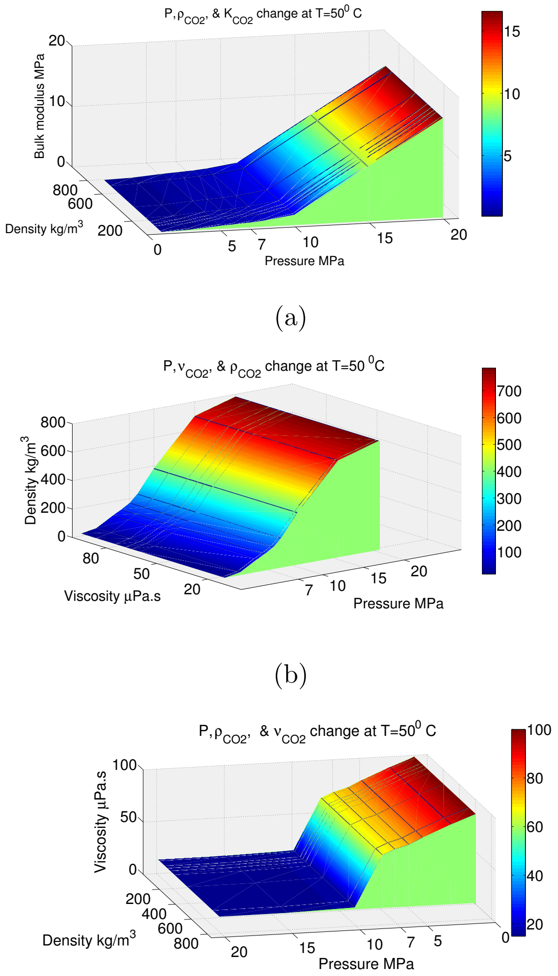

(a)

(b)

(c)

Figure 6.4: Three dimensional representations of the change of the bulk modulus, density, viscosity and pressures of the fluid CO_2 at high temperature (T=50 ^0C) and constant differential pressure showing the gas to supercritical fluid phase transition. Underlying data are obtained from NIST chemistry webBook.

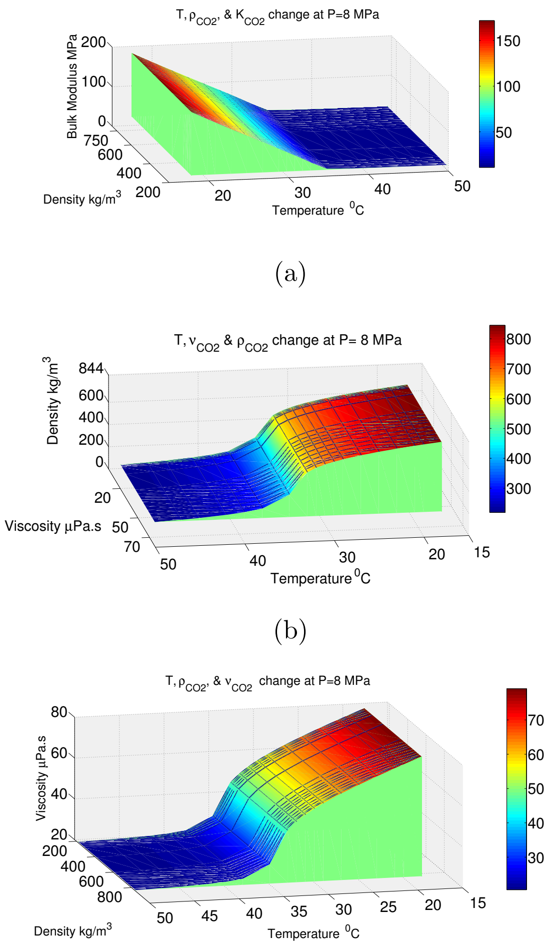

(a)

(b)

(c)

Figure 6.5: Three dimensional representations of the change of the bulk modulus, density, viscosity and temperature of the fluid CO_2 at constant pore pressure (P_p=8 MPa) and constant differential pressure showing the liquid to supercritical fluid phase transition. Underlying data are obtained from NIST chemistry webBook.

case. Almost all parameters change in a gradual fashion in this case and we see the phase transition starts around T=31 ^0C as the temperature increases.

From these 3D plots we get the idea of where to expect the phase transition to happen in all three case. We expect to see a gas to liquid transition around pore pressure P=5.686 MPa, at P= 7.40 MPa we should see the transition of gas to supercritical start and lastly liquid to supercritical fluid is more likely to begin around T=31 ^0C.

6.2 Gassmann's and Biot's fluid saturation models

We have already introduced the two fluid substitution models to predict wave velocities of a saturated porous sample in Chapter 2. Using the same pressures and temperatures that used in our experiments, the Gassmann and Biot predicted wave velocities will be calculated here for all fluids N_2, H_2O and CO_2. For the convenience I will give the Gassmann's equation here again.

6.2.1 Gassmann's Model

Gassmann's equation [29] calculates the bulk and shear moduli of a fluid saturated porous rock under some assumptions (discussed in Chapter 2). The equations are:

$$K_{sat} = K_{dry} + \frac{(1-\frac{K_{dry}}{K_s})^2}{\frac{\phi}{K_f} + \frac{1-\phi}{K_s} + \frac{K_{dry}}{K_s^2}}. \tag{6.1}$$

and

$$\mu_{sat} = \mu_{dry}. \tag{6.2}$$

Here K_{sat} is the saturated bulk modulus of the sample, K_{dry} is the bulk modulus at dry condition(no fluid present in the pores), ϕ is the porosity of the rock sample, K_s is the solid frame modulus, μ_{sat} is the saturated shear modulus which is the same as dry shear modulus μ_{dry}, and K_f is the fluid modulus. Most of these parameters are already tabulated in table 6.1 of this chapter and other paramaters are used from the NIST chemistry webBook data base.

The saturated bulk density is also important in our calculation which is

$$\rho_{sat} = (1-\phi)\rho_s + \phi\rho_f. \tag{6.3}$$

here ρ_{sat}, ρ_s, and ρ_f are saturated sample density, solid frame density and fluid density respectively.

Using the two moduli (K_{sat} and μ_{sat}) and the saturated bulk density we can predict P- and S-wave velocities for CO_2 saturated Fontainebleau sample for all cases. The wave velocities are calculated using the following equations:

$$V_{psat} = \sqrt{\frac{1}{\rho_{sat}}(K_{sat} + \frac{4}{3}\mu_{sat})}, \tag{6.4}$$

and

$$V_{ssat} = \sqrt{\frac{\mu_{sat}}{\rho_{sat}}} \tag{6.5}$$

where V_{psat} and V_{ssat} are the Gassmann predicted P-wave and S-wave velocities, respectively. We will use the Gassmann's equation to predict transverse and longitudinal wave velocities for N_2, H_2O and three CO_2 saturated cases.

6.2.1.1 Nitrogen and water saturation run and Gassmann's prediction

We have done two saturated runs with fluids N_2 and H_2O. Two samples Franc and Vif were saturated with N_2. For H_2O run I only use Franc sample. From Figures 6.1 and 6.2 we know N_2 and H_2O show a gradual change in bulk modulus and bulk density with the change of pressure at room temperature. Using

Gassmann's equation I have calculated the wave velocity predictions for both N_2 and H_2O saturated runs. As bulk modulus and density are the controlling parameters of the Gassmann velocity predictions we expect to see a gradual change in the P- and S-wave velocities during the saturation runs with N_2 and H_2O. Figure 6.6 shows the comparative illustration of lab measurements and model prediction for N_2 runs in the case of both Fontainebleau samples. In the case of both samples the prediction and observation almost coincide with each other.

Figure 6.7 shows the modelled and observed P- and S- wave velocities of the water saturated state of the Franc Fontainebleau sample. We see a similar trend for the prediction and observation results, but there is a significant velocity difference of $\sim$ 400 m/s for P-wave and $\sim$ 200 m/s for S- wave velocities. The Gassmann model over and under-predicts the observed P- and S-wave speeds, respectively.

6.2.1.2 CO_2 saturated runs and Gassmann's prediction

We had three distinct CO_2 saturation runs for both Franc and Vif samples of Fontainebleau sandstones. Now in this section we will give a comparative discussion on the measured velocities and predicted velocities through Gassmann's equation. Three cases are as follows:

6.2.1.3 Liquid to Gas transition

Figures 6.8 and 6.9 shows the comparison between the observed CO_2 saturated runs with the Gassmann predicted measurements for two Fontainebleau samples. Returning to Figure 6.3 we see a large change in both the bulk modulus and fluid density across the liquid to gas phase transition at 5.868 MPa; we anticipate that these changes must be expressed in the saturated moduli and

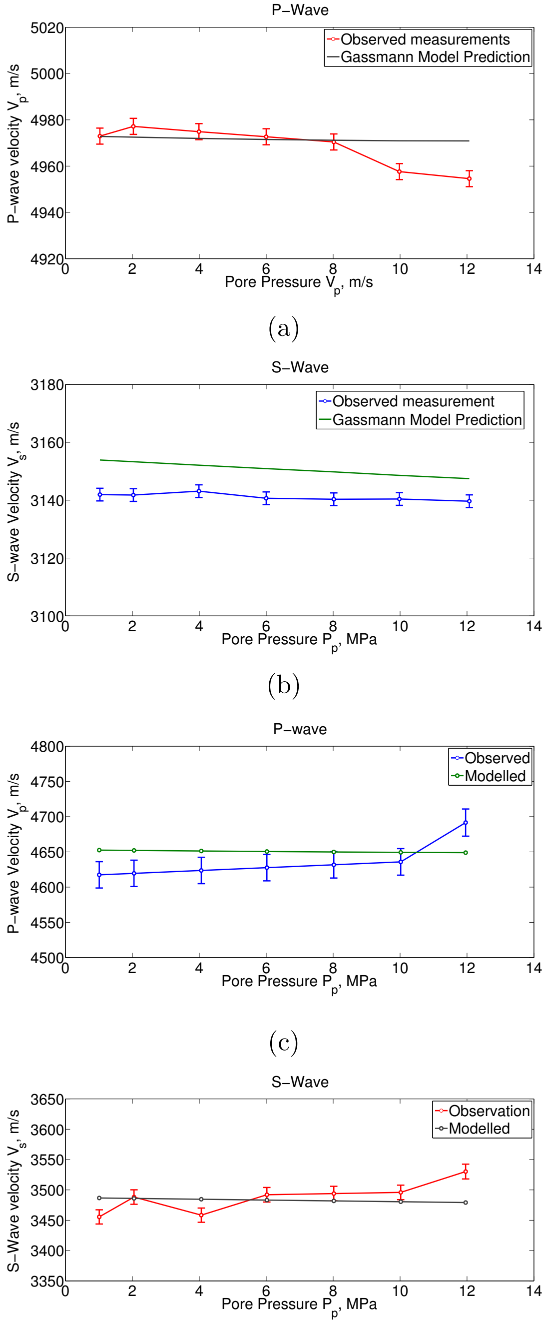

(a)

(b)

(c)

(d)

Figure 6.6: Observed N_2 saturated measurements Vs Gassmann equation for two Fontainebleau sandstones. a) and c) P-wave & b) and d) S-wave, respectively. Here observed data are the up-cycle data.

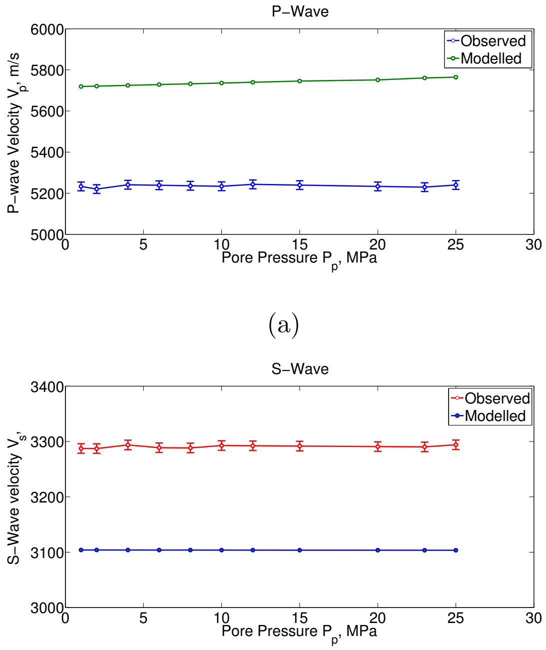

(a)

(b)

Figure 6.7: Observed H_2O saturated measurements Vs Gassmann equation for Franc Fontainebleau sandstone showing a) P-wave and b) S-wave, respectively.Here observed data are the up-cycle data.

density for the rock and hence in the values predicted using Gassmann's equation. As in the experiments described in Chapter 5, we hold the temperature and differential pressure constant at 15 MPa while varyig the pore pressure from 1 MPa to 20 MPa. The measurements of the P and S wave speeds in the previous chapter both showed relatively prominent decreases in the P and S-wave speeds across the transition from gas to liquid and it was suggested that this was due to the increase in the fluid density overcoming any changes in the bulk modulus. Gassmann's calculations here repeat this trend but with somewhat diminished values (Figure 6.8a, b) The experimental declines are 2.89% and 2.7% for the P- and S-wave, respectively while the correlating calculations only yield respective decreases of only 1% and 1.01% for the Franc sample. Similar trends are seen for the Vif sample in Figure 6.8 c), d).

Although Gassmann's equation shows relatively similar trends to the real observations, it does not in an absolute sense quantitatively reproduce them. As Figures 6.8 and 6.9 show, the calculated values are always less than the observed. The match is reasonable at lower pressures while CO_2 is a gas, but this is partly because the lower density and bulk modulus gas also affects the saturated rock modulus much less than a denser, less compressible liquid will.

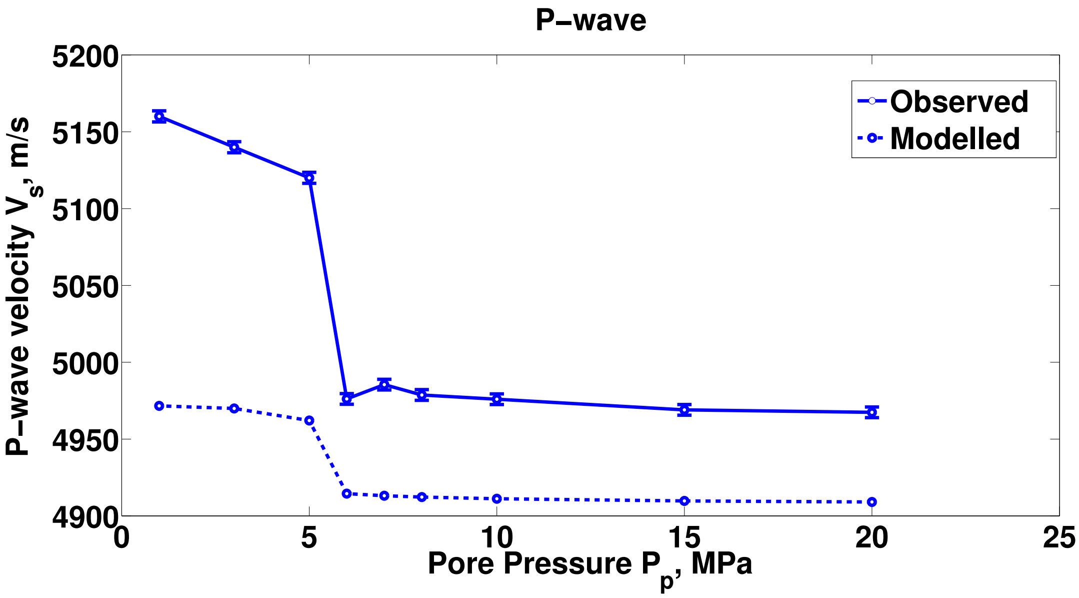

(a)

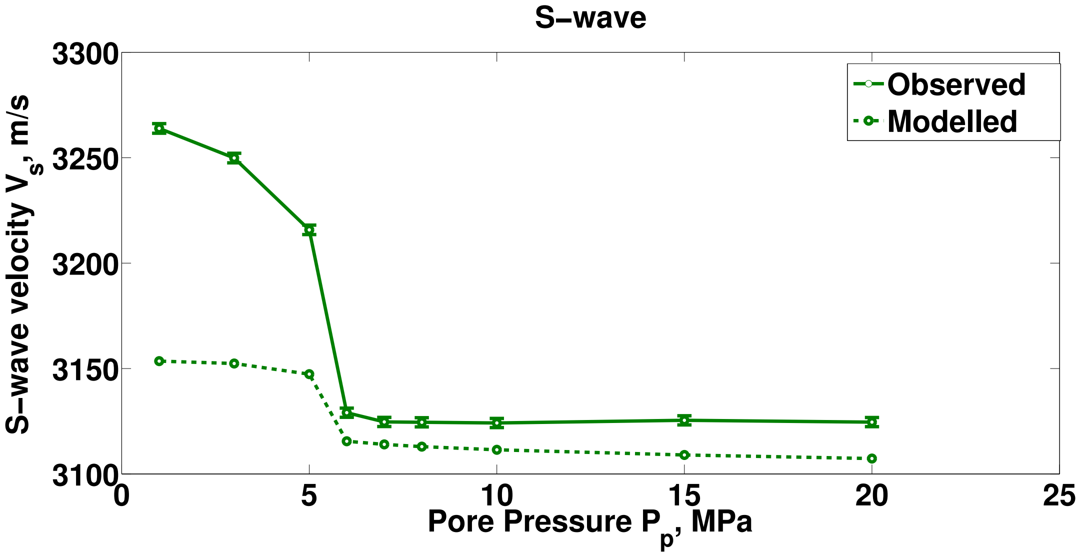

(b)

Figure 6.8: Comparison of the observed to the Gassmann predicted wave speeds for the Franc sample a) P-wave speed and b) S-wave speed. Here observed data are the up-cycle data.

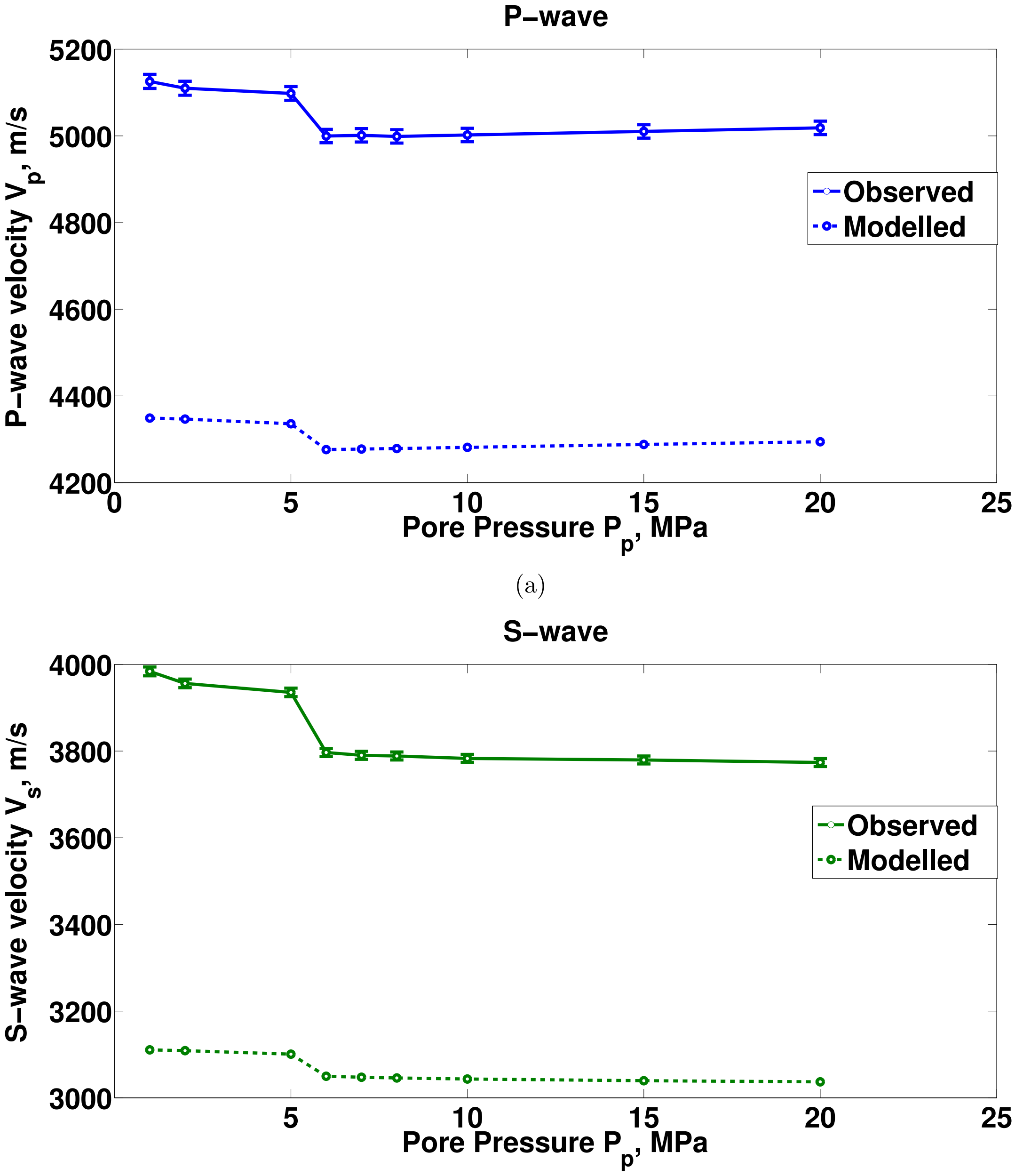

(a)

(b)

Figure 6.9: Comparison of the observed to the Gassmann predicted wave speeds for the Vif samples c) P-wave speed and d) S-wave speed. Here observed data are the up-cycle data.

6.2.1.4 Gas to Supercritical transition

Figures 6.10 and 6.11 show the comparison of observed CO_2 measurements with the Gassmann prediction for Gas to Supercritical fluid transition for both samples. In this case the temperature was constant at T=50 ^0C and a fixed differential pressure 15 MPa. The pore pressure was changed from 1 MPa to 20 MPa. In the Figure 6.4 we already saw a gradual change for bulk modulus and bulk density as the pressure changes for gas to supercritical fluid transition. Therefore we expect gradual change in Gassmann's predictions for wave velocities. Both the observed result and Gassmann prediction show similar behaviours with pore pressure for both samples. The Gassmann prediction is always lower than the observation for P-wave but for S-wave at high pore pressures ($>$ 8 MPa) the prediction shows greater values than the experimental results for the Franc sample (Figures 6.10 (a) & (b)). At high pressure for P-wave velocity shows the lowest difference than the prediction with only 0.17% difference. For S-wave at higher pore pressure we noticed the prediction is greater from the experimental results. In the overall predicted wave velocities we calculated a 1.23% drop in velocities which are lower than the experimental results for both P-and S-wave. For Vif sample we see the same trend for both P-wave and S-wave velocities for observation results and modelled prediction, although there remains a large difference between the predictions and the observations.

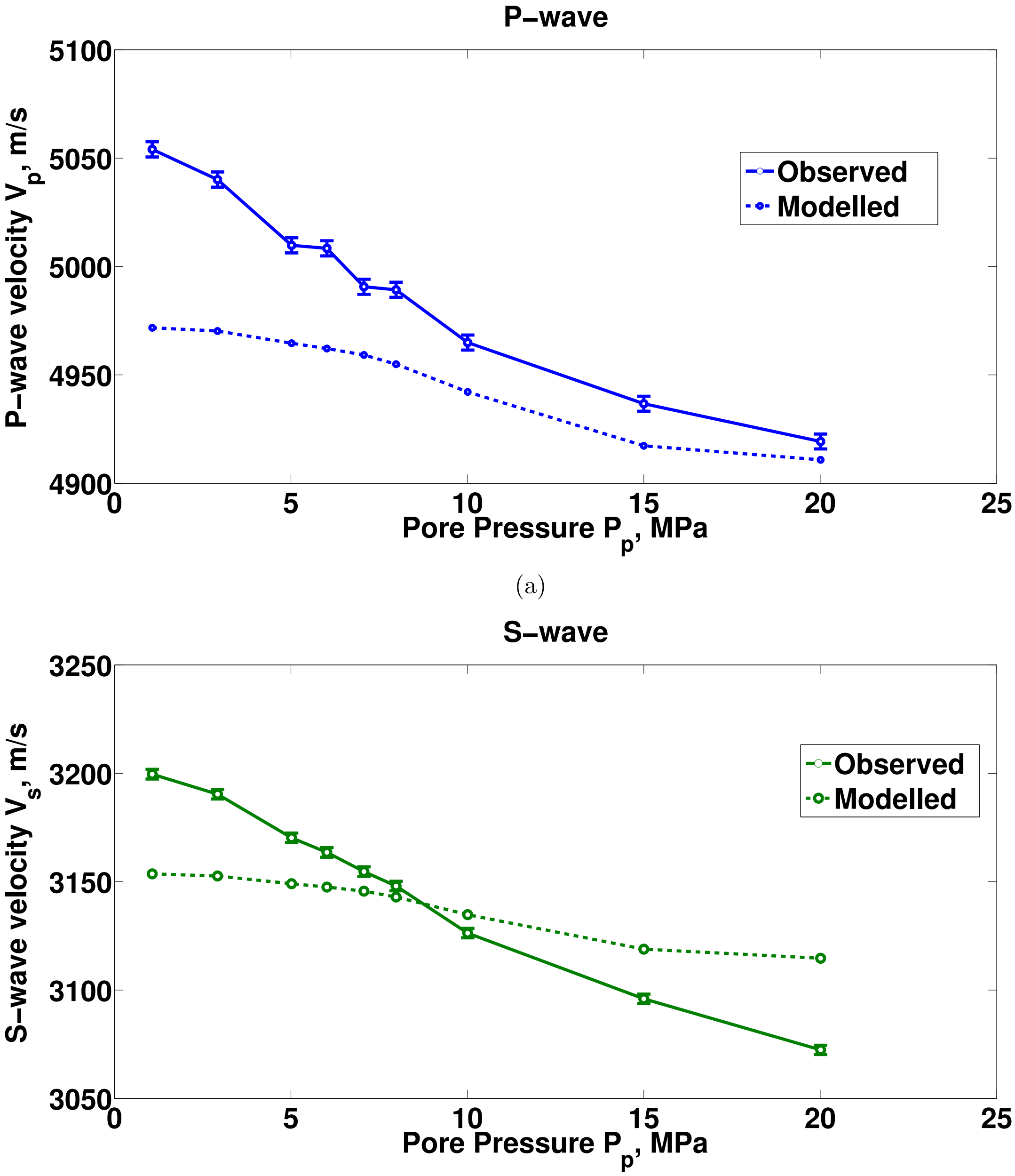

(a)

(b)

Figure 6.10: Comparison of the observed to the Gassmann prediction of the wave speeds across the gas to supercritical fluid transition for the Franc sample a) P-wave and b) S-wave.

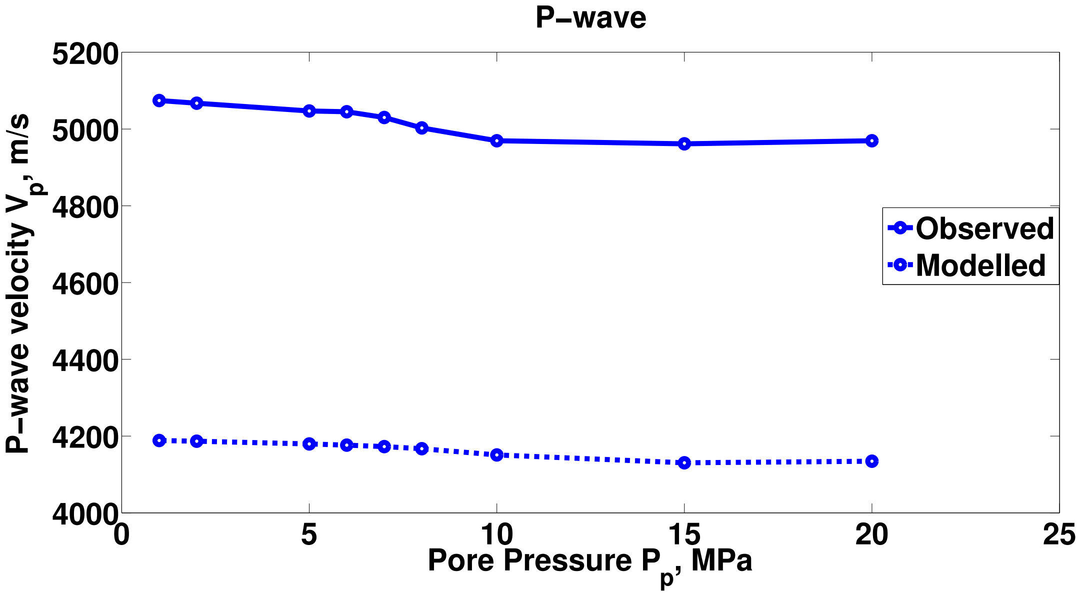

(a)

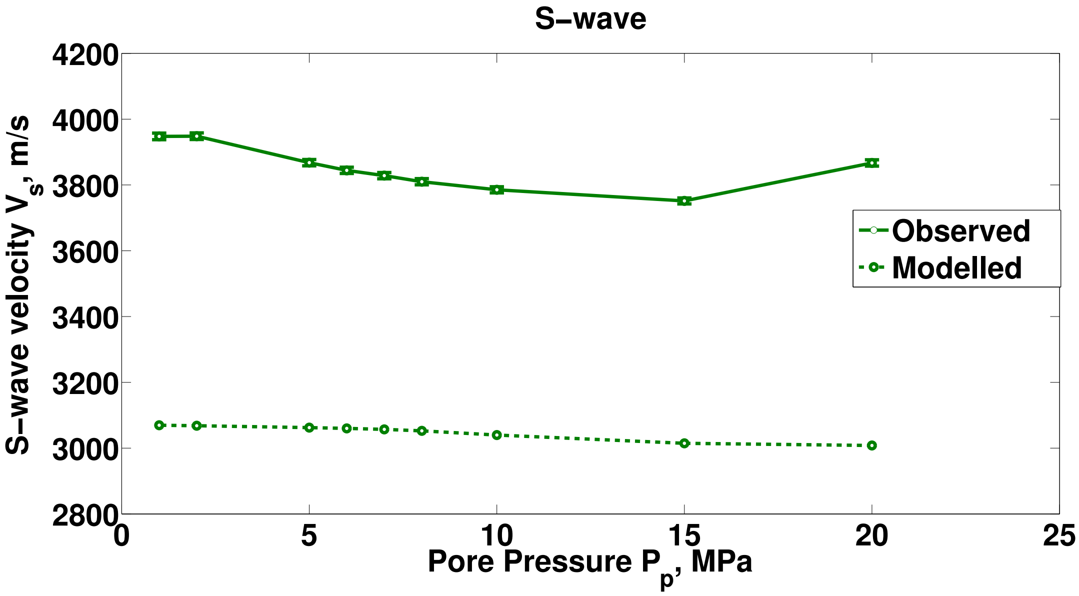

(b)

Figure 6.11: Comparison of the observed to the Gassmann prediction of the wave speeds across the gas to supercritical fluid transition for the Vif sample c) P-wave and d) S-wave.Here observed data are the up-cycle data.

6.2.1.5 Liquid to Supercritical transition

Figures 6.12 and 6.13 present the liquid to supercritical fluid transition cases with a comparison between the observation and modelled prediction for both samples. From Figure 6.5 we see a gradual change in bulk modulus and density with the increase of temperature with a constant pore pressure 8 MPa and differential pressure fixed at 15 MPa.

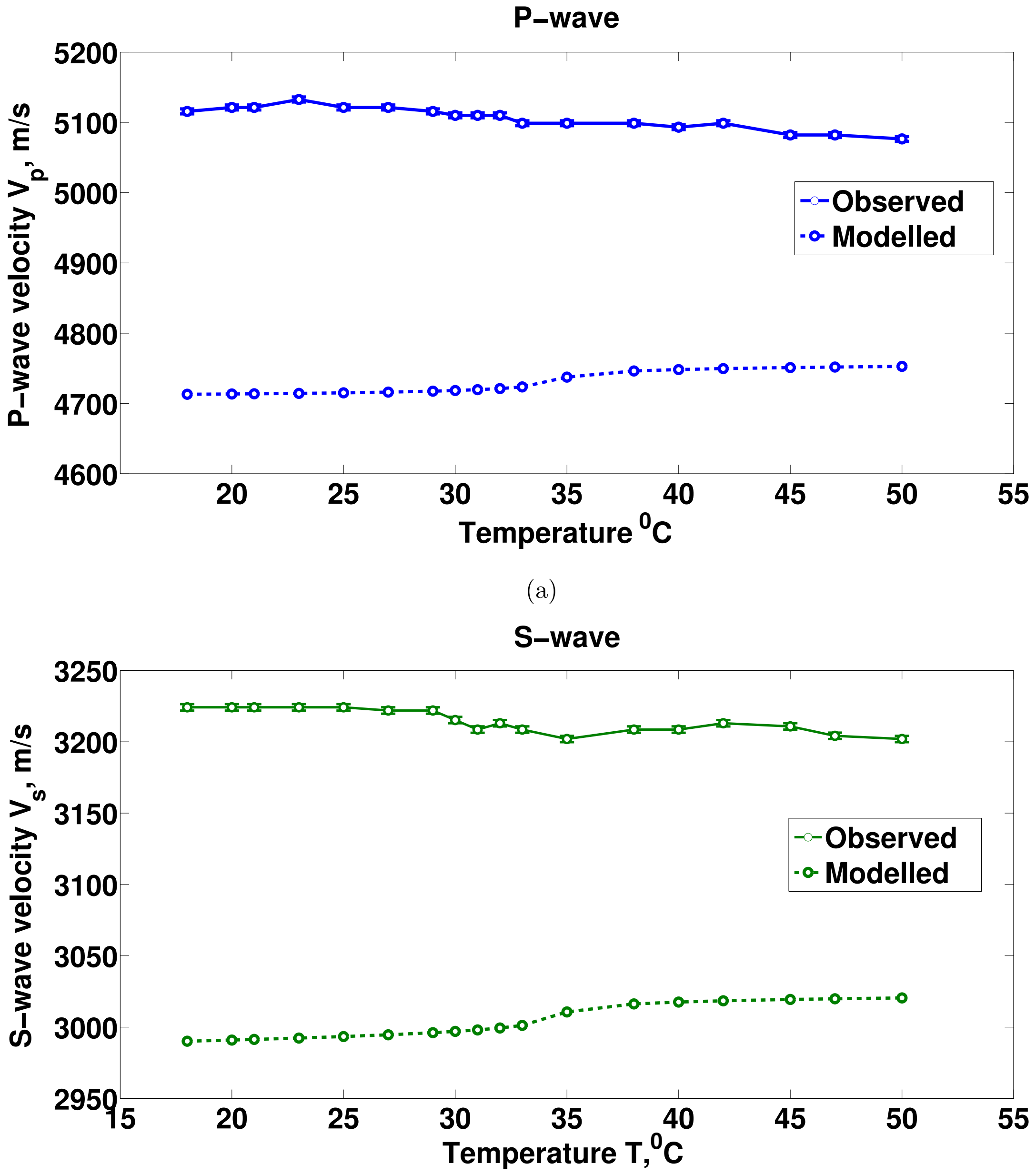

(a)

(b)

Figure 6.12: Comparison of the observed and Gassmann calculated wave speeds across the liquid to supercritical fluid transition for the Franc sample a) P-wave and b) S-wave.

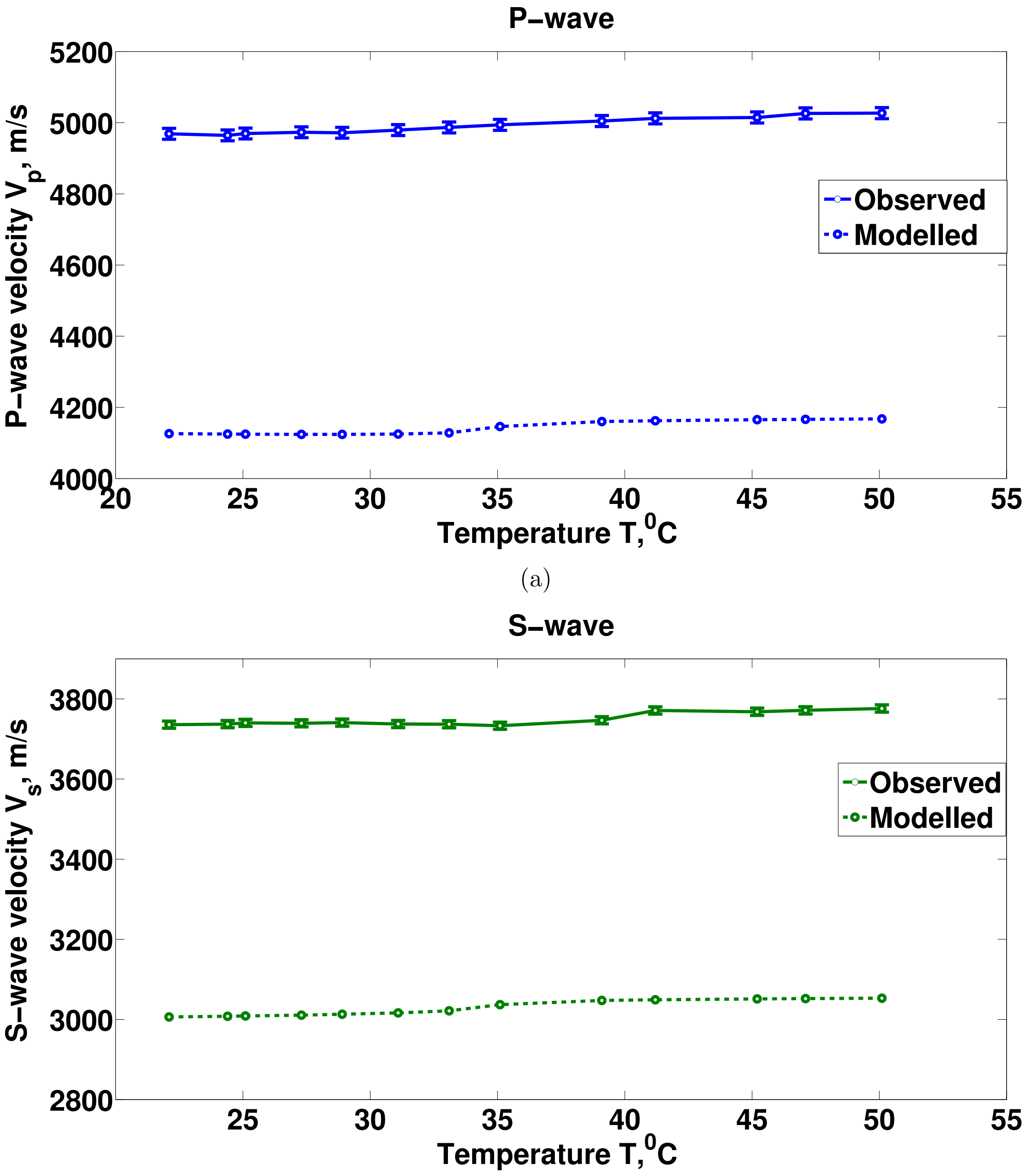

(a)

(b)

Figure 6.13: Comparison of the observed and Gassmann calculated wave speeds across the liquid to supercritical fluid transition for Vif sample c) P-wave and d) S-wave. Here observed data are the up-cycle data.

The temperature is changed from room temperature to 50^0 C. As in the other cases the trend shows an almost similarity between the lab measurements and Gassmann prediction. The absolute velocity value shows a significant difference between the observation and model. The overall prediction shows a 0.84% and 1.4% increase in wave velocities for P-wave and S-wave velocity for Franc sample. In the Vif sample prediction an overall 1.13% and 1.58% of P-wave and S-wave velocity increment, respectively.

6.2.1.6 Reasons behind the discrepancy between observations and predictions

Gassmann's [29] equation is widely used for predicting velocity changes in the cases of different pore fluid saturation. Many of the assumptions of Gassmann's equation are not true for real rock saturation cases. In our transition cases we see some differences in the absolute velocity values between the observation and Gassmann prediction. The reasons behind this discrepancy may be:

1. All real rocks are not completely isotropic there always some degree of anisotropy in them which invalidate one of the assumption where the porous material is considered as perfect isotropic.
2. Gassmann's equation is strictly valid for a static (i.e. zero frequency) case although it is usually assumed to still be applicable for frequencies below 100 Hz. The current measurements are made at ultrasonic frequencies of 1 MHz which is 4 orders of magnitude higher.
3. Related to the last statement is the possibility that the pore fluid pressures induced by the passing wave did not have time to reach equilibrium. Another way to say this is that the pore fluid pressures did not relax at the 1 MHz frequencies and this overall makes the sample stiffer.
4. The pore network within the sample may not be fully connected, again allowing for free relative motion of fluids during the passage of the wave.
5. The high frequency effect may result differential movements between the

pore fluid and pore wall that will lead to frequency-dependant were attenuation which also was not accounted in the Gassmann's model.

This strong disagreement between the predictions and the observed values necessitates use of the more sophisticated Biot model that will account for frequency effects.

6.2.2 Biot's Model

The Gassmann prediction represents the wave frequencies (<100 Hz) which are much lower than the laboratory frequencies ($\sim$ 1 MHz). From our previous discussion we saw that the Gassmann predictions are all in substantial disagreement with those observed, except perhaps at the low pressures when the pore space is saturated with low density compressible gas. As Biot's formula [59] deals with the higher wave frequencies we expect to see a better agreement between the calculated and observed velocities. Moreover, Biots theory also considers the attenuation of waves which is ignored in the Gassmann's formulation. As already discussed in Chapter 2, the Biot formula requires that both the material pore tortuosity and the fluid viscosity be introduced. The tortousity for both samples are enlisted in the table 6.1. Viscosity is not constant for any of the fluids (N_2, H_2O and CO_2) but changes with pressure and temperature. We used the viscosity values from the NIST chemistry webBook for different cases for each fluids. Now we will see how this model predicts P- and S-wave velocities for different cases.

6.2.2.1 N_2 and H_2O

Figure 6.14 shows the comparison between observed velocity and Biot's prediction velocity for P- wave and S- wave for the Franc and Vif samples under N_2 saturation and maintained at a constant effective pressure of 15 MPa As discussed earlier, we know that the N_2 transforms from the gas to the supercritical state before 4 MPa of pore pressure at room temperature. From Figure 6.1 we see that under the range of pore pressures encountered the bulk modulus, fluid density, and viscosity vary gradually even with this phase transition. As such, we do not expect to see large or discontinuous variations in the observed wave speeds. Figure 6.14 shows good comparison between the Biot predictions and the observations for the Franc sample. As with the Gassmann modelling, this is probably due more to the fact that the N_2 is of low density and is highly compressible so that it does not much affect the overall rock modulus.

The situation is somewhat different for the much more incompressible and dense H_2O. Again, the physical properties of the water, as shown in Figure 6.2, do not vary greatly over this range of fluid pressures from 1 MPa to 25 MPa and at the constant temperature of 21 ^0C, and this lack of variations transfers to a lack of pore pressure dependency for the P and S-wave velocities in Figure 6.15. However, there is a large discrepancy of about 400 m/s that remains. Clearly, Biot's model as applied here does not adequately account for the frequency effects for a liquid in this rock.

6.2.2.2 Biot's prediction on different cases for CO_2 saturation

For the cases of constant low temperature (21^0 C) and high temperature (50 ^{0} C) with unchanged 15 MPa differential pressure, Biot's modelled P-wave and S-wave velocities of the CO_2 saturated two types Fontainebleau sandstone are shown in the Figures 6.16 to 6.19. Both of the Biot's modelled velocity curves give a similar behavioural trend as the Gassmann prediction with changing pore pressures under conditions. The gas to supercritical fluid transition shows a more compatible trend to the laboratory results than the Gassmann's predicted for S-wave velocity in Biot's formulation. Moreover for Franc sample we see the maximum difference in wave velocities between lab measurements and Biot's predictions is $\sim$ 170 m/s while the Vif sample there is a maximum difference

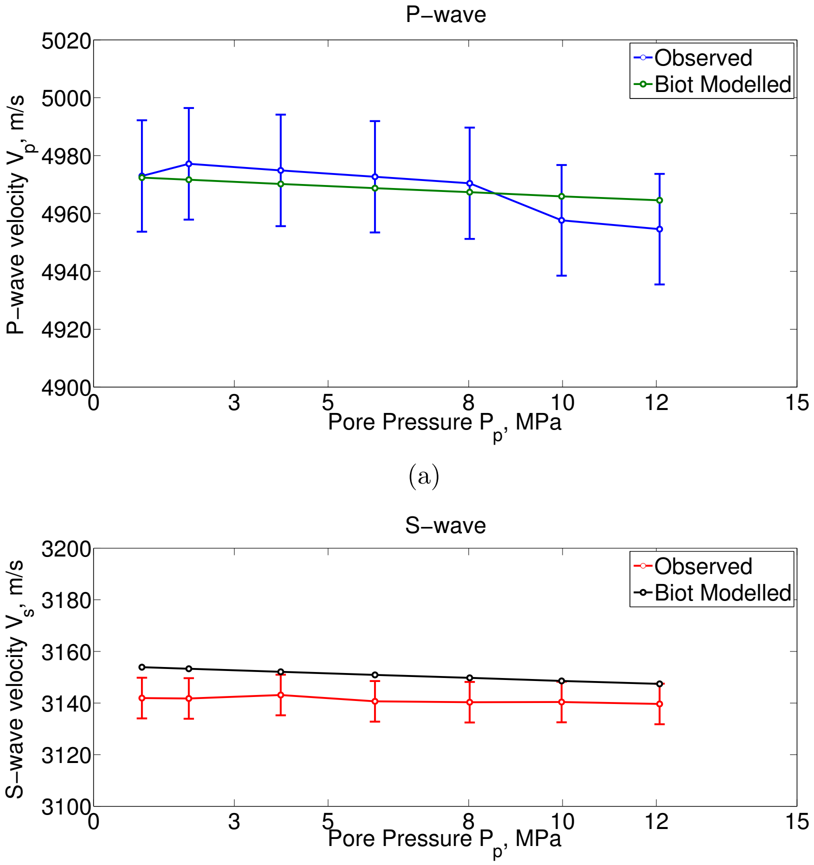

(a)

(b)

Figure 6.14: Comparison of observed and Biot predicted a) P-wave and b) S-wave speeds for the Franc sample under N_2 saturation. Here observed data are the up-cycle data.

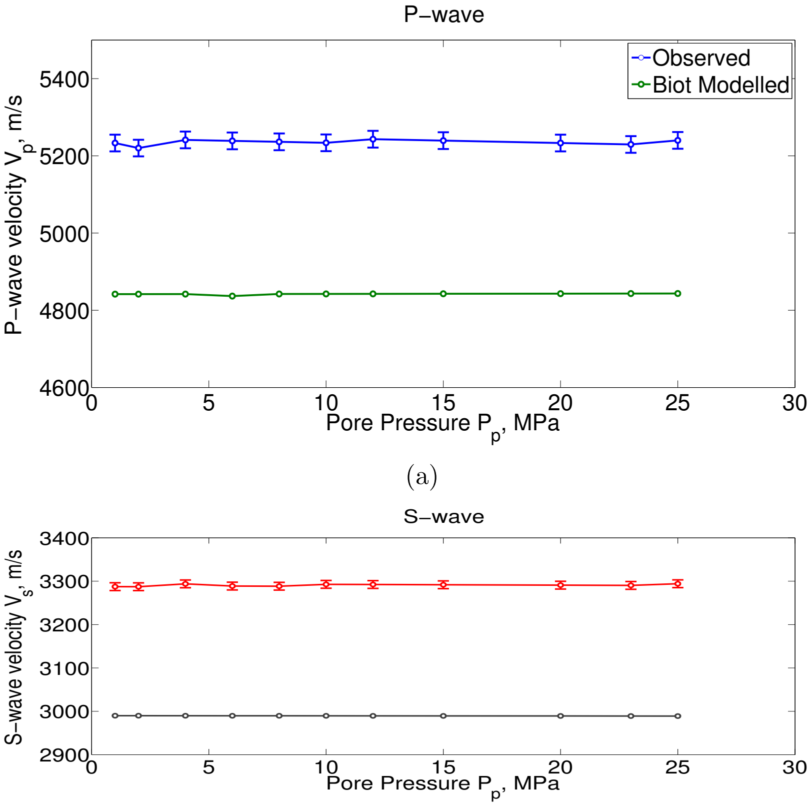

(a)

(b)

Figure 6.15: Comparison of observed and Biot predicted a) P-wave and b) S-wave speeds for the Franc sample under H_2O saturation. Here observed data are the up-cycle data.

of $\sim$ 200 m/s.

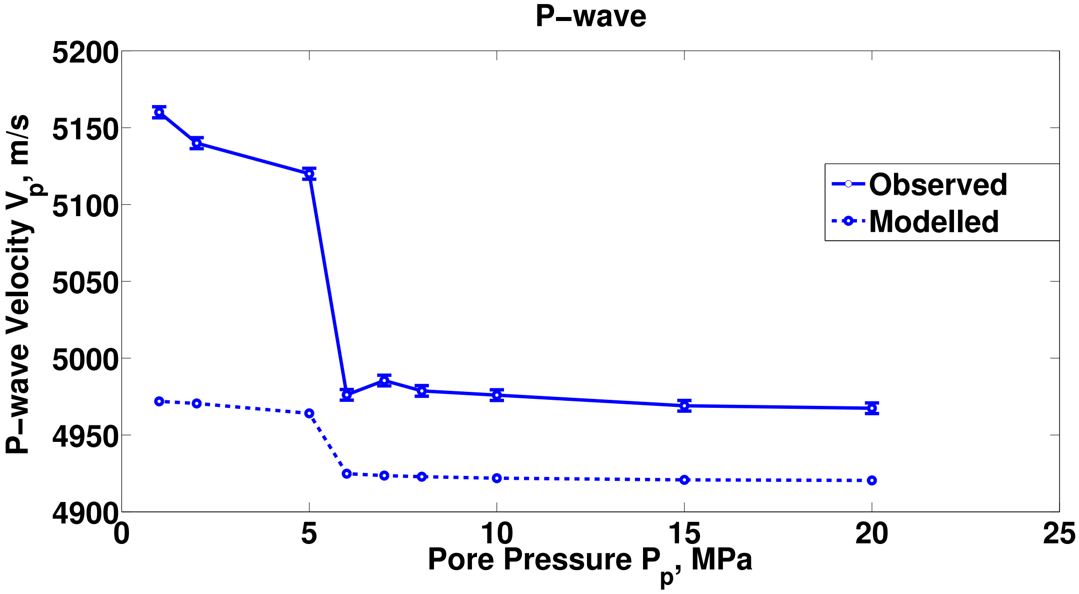

(a)

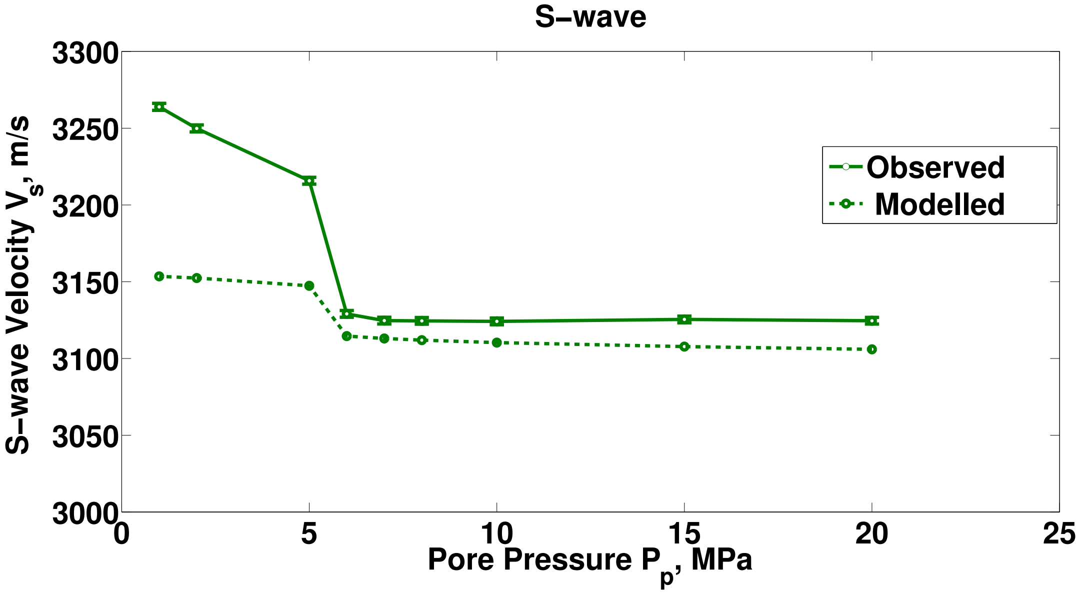

(b)

Figure 6.16: Comparison of the velocities observed and predicting using Biot's model for the gas to liquid transition of CO_2 for the Franc sample a) P-wave and b) S-wave. Here observed data are the up-cycle data.

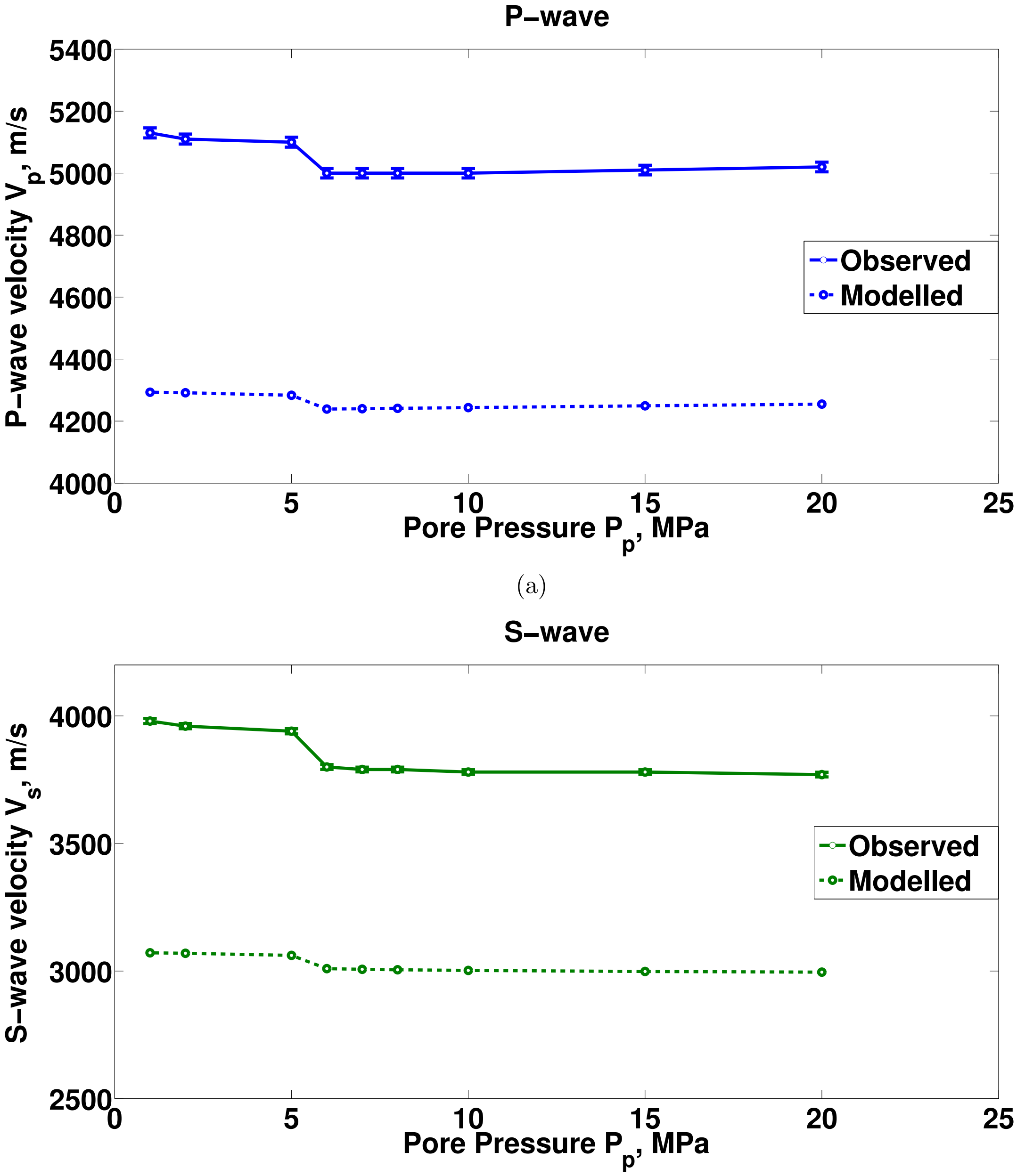

(a)

(b)

Figure 6.17: Comparison of the velocities observed and predicting using Biot's model for the gas to liquid transition of CO_2 for Vif sample c) P-wave and d) S-wave. Here observed data are the up-cycle data.

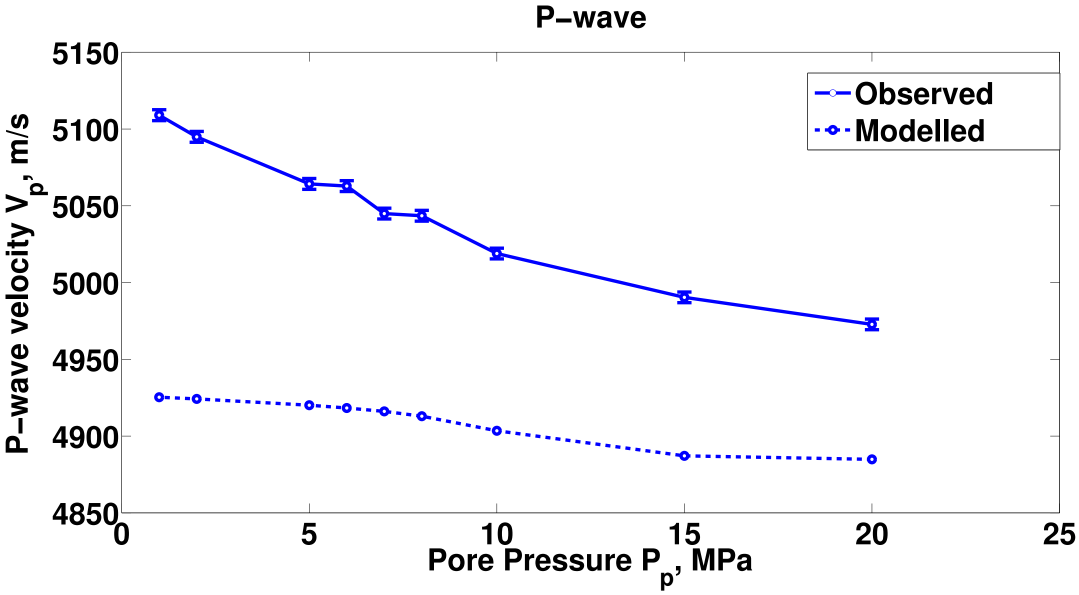

(a)

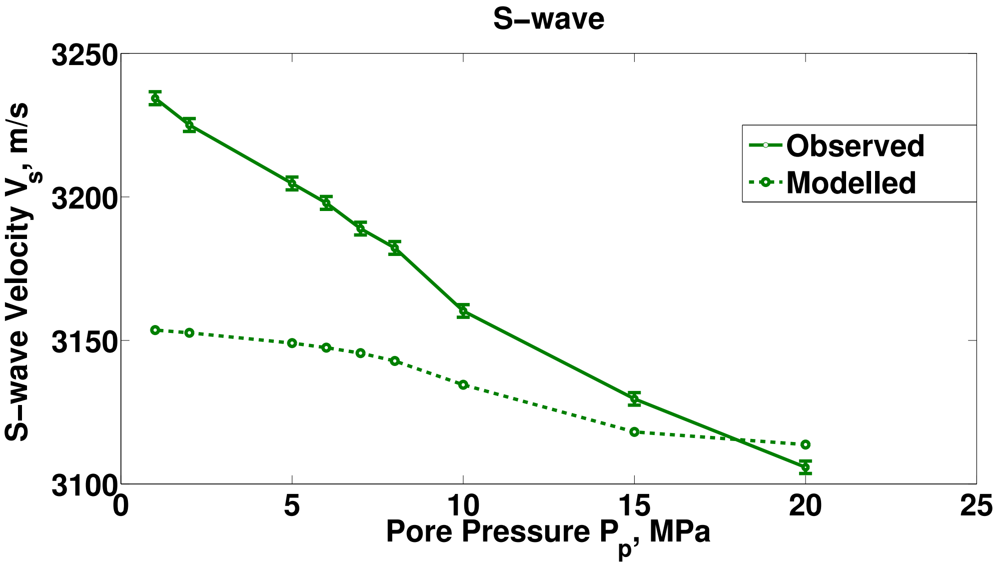

(b)

Figure 6.18: Comparision of the wave speeds observed and calculated using Biot's model across the gas to supercritical fluid transition for the Franc sample a) P-wave and b) S-wave. Here observed data are the up-cycle data.

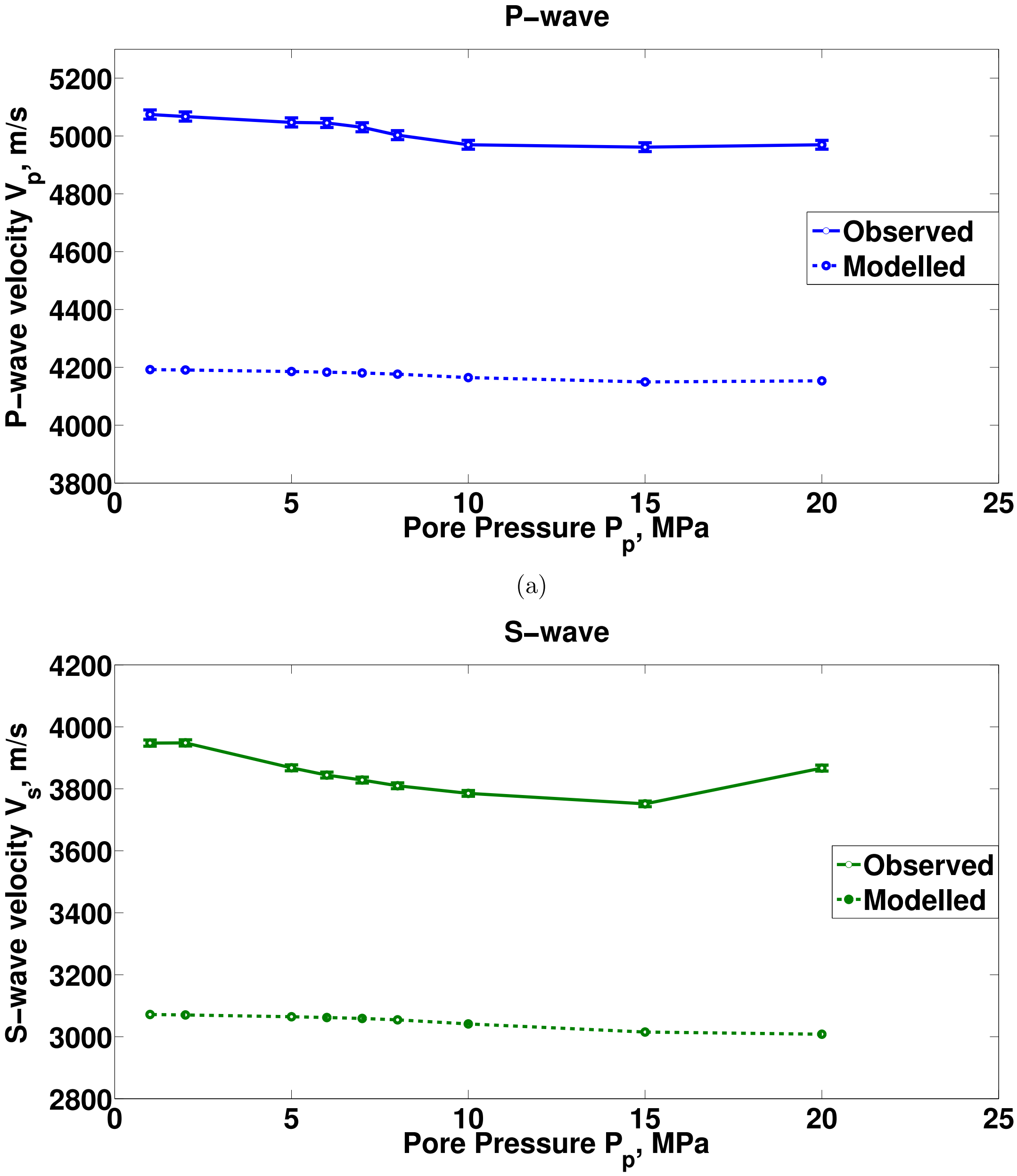

(a)

(b)

Figure 6.19: Comparision of the wave speeds observed and calculated using Biot's model across the gas to supercritical fluid transition for the Vif sample c) P-wave and d) S-wave. Here observed data are the up-cycle data.

The observed and predicted changes in the CO_2 saturated wave speeds across the liquid to supercritical fluid transition at a constant pore pressure of 8 MPa are shown in Figures 6.20 and 6.21. These show similar trends to those for the Gassmann calculations shown earlier.

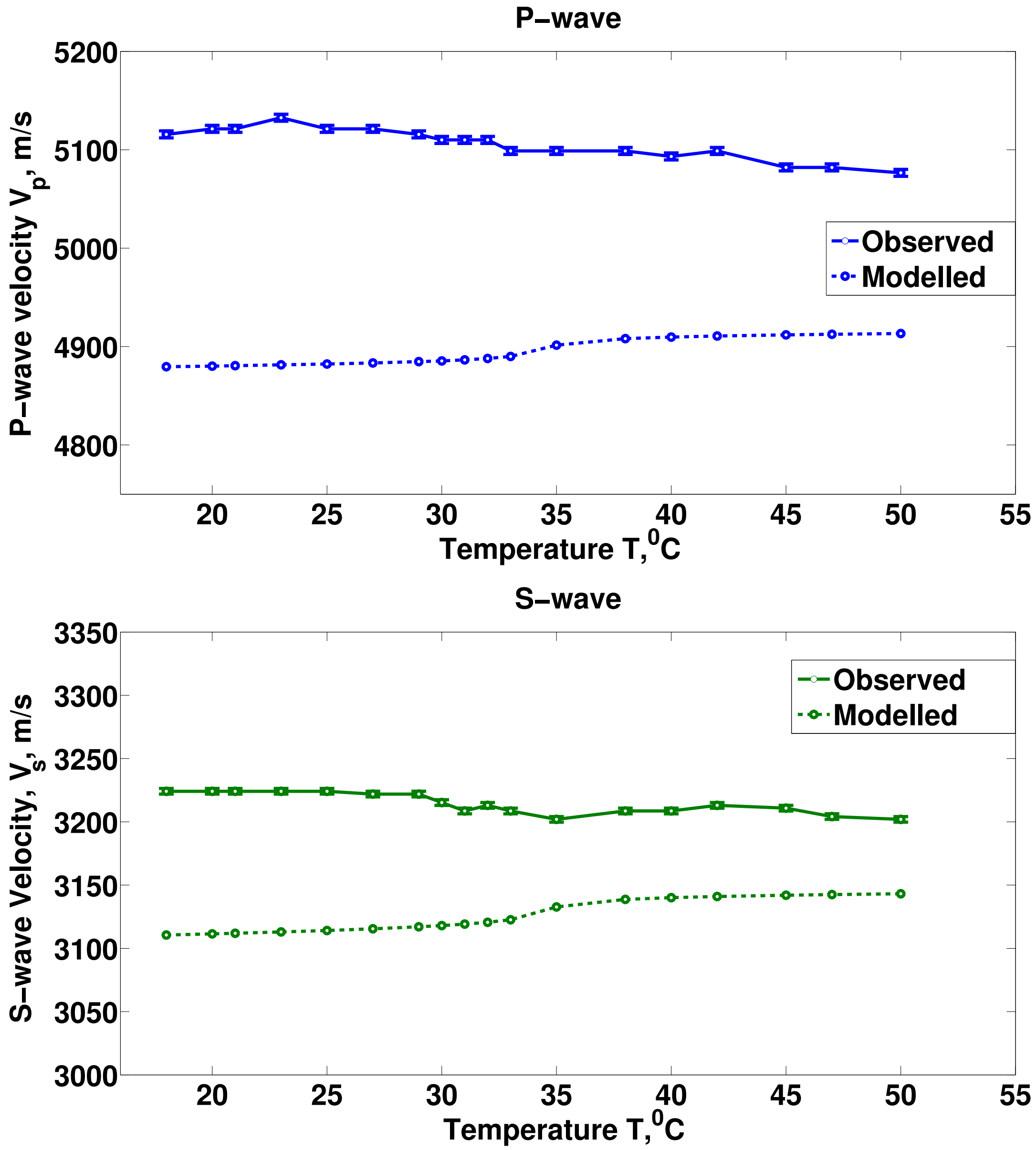

Figure 6.20: Comparison of the observed and Biot predicted velocities under as a function of pore pressure at constant effective pressure of 15 MPa and the room temperature of 21^0C. Panels are for the Franc sample a) P-wave speed and b) S-wave speed. Here observed data are the up-cycle data.

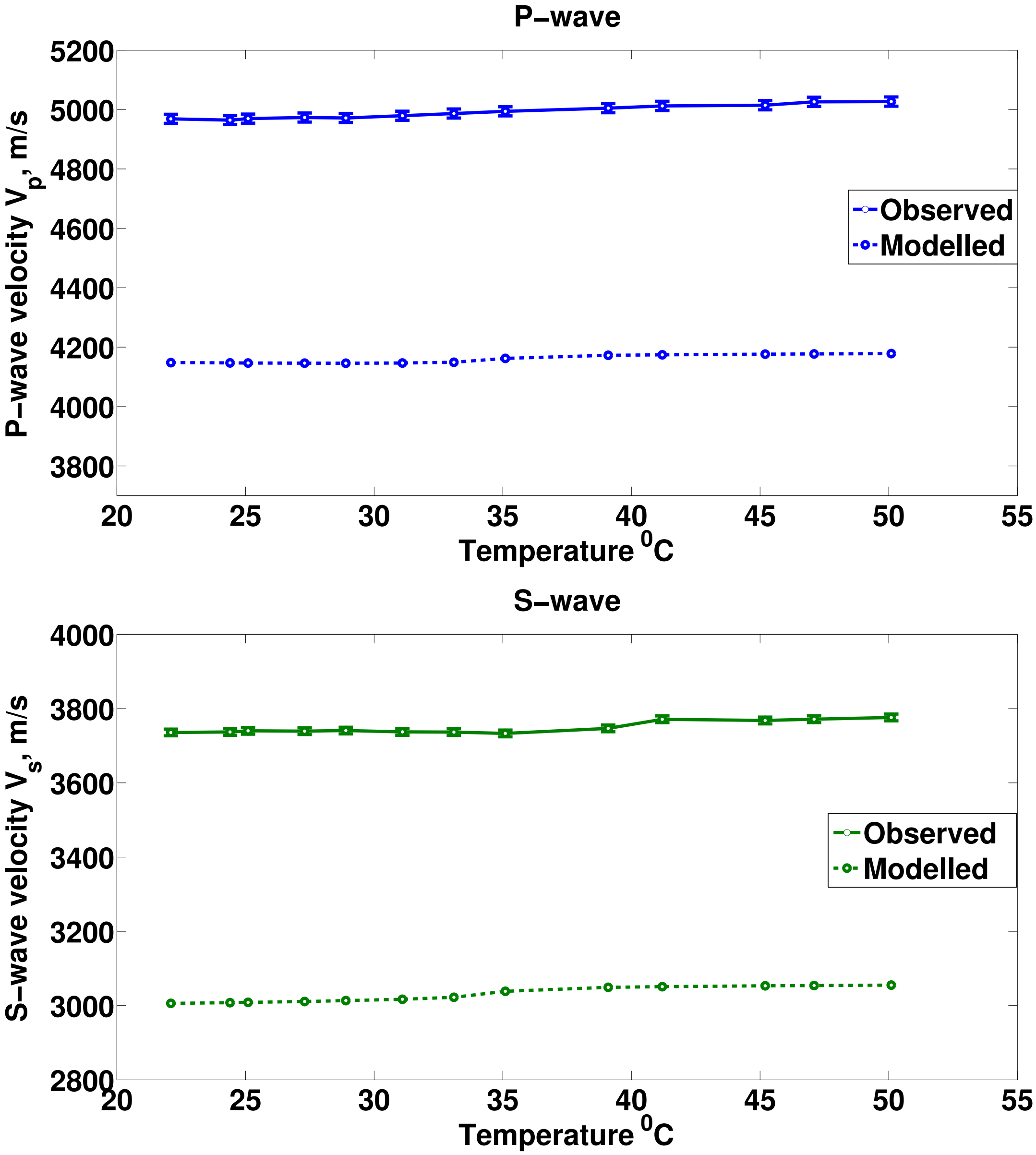

Figure 6.21: Comparison of the observed and Biot predicted velocities under as a function of pore pressure at constant effective pressure of 15 MPa and the room temperature of 21^0C. Panels are for the Vif sample c) P-wave speed and d) S-wave speed. Here observed data are the up-cycle data.

6.3 Results and Discussion

We will discuss about the pore fluid effects of N_2, H_2O, and CO_2 on the wave behaviours observed and modelled in this chapter. The similarities and differences between the results of the two Fontainebleau samples will also be discussed here. For N_2 saturation cases for both samples we see a good agreement between the observed and modelled results (Gassmann and Biot).
For H_2O saturation we noticed similar trend but large differences in the velocities between the lab results and model predictions (Gassmann and Biot). One of the contributing factor to changing the sample integrity during the water is due to chemical change. After CO_2 runs we vacuum the system over night and we can not perfectly sure that there is no trace of CO_2 presented during the water run. If any CO_2 remains in the samples the mixture of CO_2 and water may form an acidic solution that could chemically react with the rock minerals. There was no chemical analysis done after the water run which would be efficient step to know precisely if any chemical effect went through the time of water runs.

For CO_2 saturation runs we noticed the dominance of bulk density over bulk modulus in affecting the wave velocity for both samples in most of the observed and modelled wave velocity responses. From Figure 6.3 through 6.5 we saw the greater influence of the fluid density over the bulk modulus for all CO_2 fluid saturation cases. Again, the discontinuity in the CO_2 density and bulk modulus at the gas-liquid phase boundary has a large impact on the changes in the wave speeds. The changes across the 2nd order transitions to the supercritical fluid state are continuous and their wave speeds alone provide no information on the face transition location.

Though both of the samples are two different types of Fontainebleau sandstone, they still show some differences between the observations and modelled predictions. One of the reason is may be that the real rock is always far more complex in various aspects than Gassmann's and Biot's simple assumptions are able to account for. It is likely the fact that much of the porosity is more 'crack-like' in these samples that causes the descrepancy between the observed and modelled values. . Another reason may be the tortousity measurement. The tortousity of the samples were calculated from Archie's modified equation (discussed in chapter 2) which also may not always give a real value for this parameter.

6.4 Summary

A detail discussion with the comparison of observation and two modelled (Gassmann's and Biot's) predictions were presented in this chapter for all three fluid saturation states of N_2, H_2O, and CO_2. We saw a good matching between theory and observation for nitrogen saturation case. For H_2O saturation we found the similar trend between the observation and prediction but the absolute values between the two were quite discrepant. For the cases of CO_2 saturations for both samples we saw the good agreement with theories in terms of changing velocity with the corresponding observation results. The predicted values were somewhat better for the Franc sample than the Vif sample. As understanding real rock is always difficult, the assumptions of Gassmann's and Biot's were not able to adequately describe the behaviour of the two Fontainebleau samples. Despite this, we did obtain some good insight of the samples through comparing our observations with these fluid models.

Chapter 7

Implications for seismic monitoring

So far we have presented the fully saturated cases of N_2, H_2O and different phase transition cases of CO_2 saturations and thereby showed influence of these fluid saturations on the acoustic properties of the rock. This is useful information but in a real reservoir situation one might otherwise expect the CO_2 to co-exist with other reservoir fluids such as brine or hydrocarbons. As such, we presented here only end-member experimental results and simple saturation models. The real situation is likely better characterized by greater complexity of the heterogeneity with patchy saturations and varying degrees of saturation throughout the reservoir. Presenting a full reservoir model on the basis of our experimental results alone remains difficult.

The main goal of reflection seismology is to image the subsurface structure of the earth by producing essentially a mapping of the variations of the seismic reflectivity with depth. In this chapter we will introduce the concept of reflectivity and then apply this to determine how seismic reflectivity may change in a reservoir containing CO_2 and H_2O during sequestration.

7.1 Reflectivity

For seismic monitoring purpose, in an ideal case, we could find out the fluid movements remotely by observing the changes in the seismic reflectivity as a function of time. The reflection coefficient R of a reflected wave, for the simple case of normal seismic reflections from the interface between two elastic materials is given by

$$R = \frac{Z_2 - Z_1}{Z_1 + Z_2}, \tag{7.1}$$

Here Z_i's are the acoustic impedance defined as $Z_i = V_i \rho_i$ where V_i is the acoustic velocity, ρ_i is the material density, and $i = 1, 2$; 1 and 2 indicates the upper and lower layers of the material, respectively [38].

In Figure 7.1 we show the P- and S- wave impedances for water and CO_2 saturation. The impedances were calculated using the density and wave speeds for the Fontainebleau Franc sample. There is little change in the impedances with pore pressure under water saturation. Again, this situation was expected as the physical properties of the water itself do not vary significantly over this relativity modest range of pressures. The CO_2 properties, in contrast, are substantially more pressure dependent and again the increases in density are important even before the phase transition occurs. The decrease in the impedances are not surprising given that the wave speeds are both observed and modelled to decrease across the same pressure intervals as shown in Chapters 5 and 6. The discontinuous nature of the CO_2 gas to liquid phase transition is again apparent in the impedances as is the lack of discontinuity for the gas to supercritical transition.

For the current sample, we calculate the reflectivity R as a function of pressure for the hypothetical contact, within a uniform geological formation composed of the Franc sample, but with zones that are saturated fully either with water

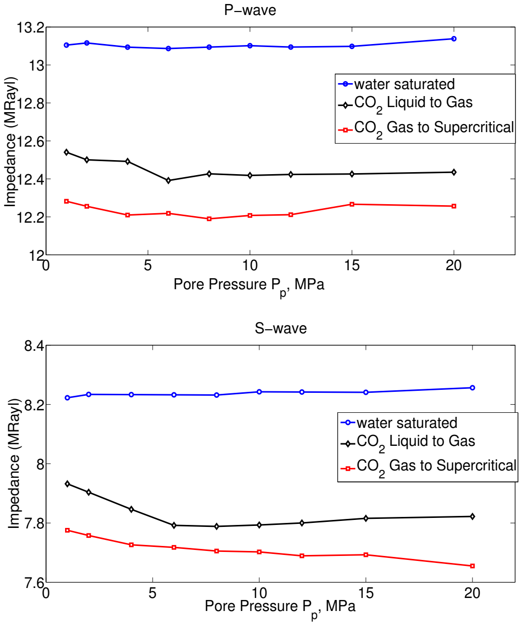

Figure 7.1: Figures 1a) and 1b) show the P- and S-wave acoustic impedances for Franc type Fontainebleau sample under a constant differential pressure of 15 MPa. The blue line indicates the water run, the black line shows the CO_2 saturated run for low temperature (liquid to gas transition), and the red line gives high temperature case for CO_2 (liquid to supercritical fluid). Impedance unit is taken as Rayl which is 1 MRayl=10^6 $kg/s.m^2$

or with CO_2. In this case we assign layer 1 and layer 2 to the H_2O and CO_2 saturated cases, respectively. This is not perhaps exactly the case we might expect in situ as eventually we would anticipate that in a reservoir the denser water would sink beneath the CO_2, but it would be representative of a the case where CO_2 has been injected near the bottom of the reservoir initially. [38, 104, 105].

Figure 7.2 shows the reflectivity of the hypothetical geological structure for a) low temperature and b) high temperature cases, respectively. The low temperature case could be represented a relatively cold reservoir. Both R_p and R_s gradually increases until the gas-liquid transition pressure but after transition the reflectivity remains almost unchanged. For the high temperature case there is not a large change in the coefficients for both P- and S- wave aside from a gradual increase as the pore pressure increases. At low pressure both

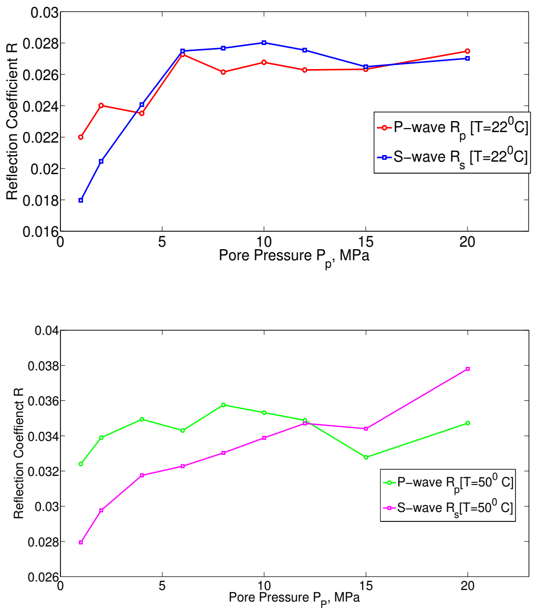

Figure 7.2: An imaginary normal incidence P- and S- waves reflection coefficient with the acoustic properties of Fontainebleau sample considering water over CO_2 geometry for a) low temperature and b) high temperature cases.

scenarios show small coefficients giving less bright reflection of acoustic waves.

7.2 Summary

For a real-world situations where CO_2 may coexist with other in situ fluids such as oil and brine in pore spaces, we made a hypothetical reservoir conditions and calculated the seismic reflectivity for a zone fully saturated with CO_2 underlying a fully water saturated zone. The results suggest that at the high pressure the seismic reflectivity is brighter than the lower pressures.

Chapter 8

Conclusion

Locating the subsurface movement of stored CO_2 quantitatively and qualitatively in a geological CO_2 sequestration site is very important. The time-lapse seismic method is perhaps the most effective means of carrying out such monitoring over a wide area. CO_2 can be a gas, liquid or supercritical fluid depending on different physical conditions of pressure and temperature it is subject to. These changing conditions also influence the bulk modulus, density, and viscosity of CO_2 and these varying fluid properties influence the overall ultrasonic wave speeds. In our work we investigated the influence of N_2, CO_2, and H_2O as pore fluids in Fontainebleau sandstone samples on the overall seismic wave responses. We have presented an end-member study by conducting different measurements using full saturated CO_2 to show its pore fluid effects on the rock samples.

In this thesis, we have performed a series of ultrasonic measurements on two Fontainebleau sandstone samples with N_2, CO_2, and H_2O pore fluid saturation under various pressures and temperature conditions. The two fluid saturation models of Gassmann and Biot were applied to compare against the observations. In the case of CO_2 saturation we carried out three distinct suites of measurements to examine the gas to liquid, gas to supercritical fluid, and liquid to supercritical fluid transitions. Experiments were carried out on the Fontainebleu sandstone that is popular in rock physics studies because it is composed of nearly pure quartz grains. Three types of this rock were provided to us: Maigre, Franc, and Vif that are separately distinguished on the basis of their increasing strength and solidity. As the Maigre sample did not survive shipment, we worked only on the Franc and Vif materials with respective porosities of 6.8% and 12.5%. Mercury injection porosimetry also showed these samples to have modal pore sizes that ranged from 2.1 mm for Franc but 7.86 mm for Vif. Microscopy and the behaviour of the samples under pressurization indicated too that a substantial portion of their porosity is microcracks.

As noted, an interesting aspect of CO_2 is that it can be either in gas, liquid, or supercritical states at modest pore pressures and temperatures. As such, we devised a measurement protocol that attempted to study the rock properties under these different conditions and to provide necessary data for modelling. The experimental plan followed:

1) Dry measurements with the pore space subject to vacuum. In this the P and S-wave speeds were measured as a function of the confining pressure. These results are necessary in order to obtain values of the dry bulk and shear moduli that are needed for the Gassmann and Biot calculations of Chapter 6. The observed wave speeds, too, displayed significant nonlinear behaviour with increasing confining pressure further confirming the significant microcracking of the rock.

2) N_2 saturated tests. Here, the P- and S-wave speeds were measured with the sample subject to a constant effective or differential pressure of 15 MPa with the pore and confining pressures tracking one another from 1 MP to 12 MPa and 16 MPa to 27 MPa, respectively. All of these measurements were carried out at a constant temperature of 21^0C. The purpose of these tests was to carry out the measurements using an inert low density, highly compressible fluid in order to mimic a gas phase. Under these constant effective pressure conditions

we observed nearly no changes in the wave speeds.

3) CO_2 saturated test. These are the primary measurements of this thesis. All of these measurements were made, again, at the constant effective pressure of 15 MPa but three different runs were made in order to cross the gas-liquid, the gas-supercritical, and the liquid-supercritical phase boundaries. The results of the measurements, described in detail in Chapter 5, showed large discontinuous decreases in both the P- and S-wave speeds upon the transition from gas to liquid. This contrasted with the gradual and smooth changes across both transitions to the supercritical state. This was not unexpected as these latter transitions are known to be of 2nd or higher order meaning that there is no noticeable change in the physical properties across the transition. The discontinuous decrease in the wave speed across the transition from gas to liquid indicates that they are controlled primarily by the variation in the CO_2 density. In this one must recall the equations that relate elastic moduli and density to the wave speeds. Density is in the denominator of these equations and the decline in the wave speeds indicate that the increased density is more important than the increased fluid bulk modulus.

4) H_20 saturated tests: The final set of measurements were carried out with distilled H_20 saturating the pore space to provide a case in which the pore fluid remains liquid over the entire pressure and temperature range studied. Again, these measurements were carried out at the chosen constant effective pressure of 15 MPa with the sample otherwise subject to nearly the same conditions as for the N_2 case. Again, the velocities changed little during the test again in agreement with expectation as the physical properties of the liquid did not vary significantly across this range of pore pressures.

Using the experimental values of the dry frame modulus together with the properties of quartz and the saturating fluids under the temperatures and pore pressures of the tests, we carried out the exercise of applying Gassmann's formulae to predict the observed wave speeds. To some degree this is not valid as the measurements are carried out at 1 MHz frequencies while Gassmann's formulae apply strictly only under static undrained conditions (i.e. approaching zero frequency). Accordingly, the observed and predicted values did not agree although the trends between the two were similar. Model for both samples gave us prediction of wave velocities under the experimental physical conditions. Though our measurements are done on ultrasonic frequency ($\sim$ 1 MHz), prediction trends were matching with the observations. Wang, Marion and Jizba, Baechle et al. and Rogen et al.)[106, 107, 108, 109] have previously shown that Gassmann's prediction mostly underpredict the ultrasonic frequency measurements. For the suite of measurements here, the Gassmann predictions are about 3% and 15% lower than those observed in the Franc and Vif samples, respectively.

An attempt was made to employ Biot's more sophisticated model that incorporates frequency. This model attempts to more explicitly account for differential movements between the fluid and the solid in the rock frame as the wave passes. Biot's predictions of the wave speeds here did not vary much from Gassmann's, however, and this tells us that the Biot model also does not adequately account for this kind of rock that contains large aperture microcrack like pores. The rationale for this disagreement was discussed in detail in Chapter 6, but briefly it lies in the fact that the Gassmann's model cannot account for the effects of high frequency wave propagation particularly through the complex porosity structure of these sandstones.

Finally, using our empirical measurements of wave speeds and densities, we considered a hypothetical reservoir situation where a CO_2 saturated layer overlies a water saturated layer within the same rock type. The pore pressure and temperature dependent impedances were calculated and these in turn were used to determine the normal incidence reflectivity from the CO_2-water saturated interface. The results suggest that at the high pressure (when the CO_2 is high density compressible gas) the seismic reflectivity is brighter.

8.1 Future work

To date, we have only carried out measurements in a quite clean quartz sandstone saturated with a single fluid at a time. We see this as only the beginning and a great deal of additional work is necessary. Short term goals should include

1. Testing samples with brines containing various saturations of CO_2 in solution. This can be accomplished relatively easily using our existing system. We note that parallel work is now ongoing on determining the waves speeds (and hence bulk moduli) of CO_2 saturated brines in our laboratory.
2. Testing samples with mixed phase brines and CO_2 in the pore spaces. This too in principle could be carried out with the existing system but one problem is that actually knowing the true saturation state within the pore spaces of the samples can be highly problematic.
3. Repeating the experiments but over longer time periods to see if there are any chemical effects (precipitation of carbonate minerals) that might change the rock frame and hence its elastic and seismic properties.
4. Carrying out similar measurements on the more common case of sandstones that contain clay minerals. We may expect some kinds of chemical reactions of the CO_2 with these clays to for carbonate minerals and this may have effects on both the fluid properties and the rock matrix with detectable elastic changes.

There should also be longer term goals. These could include

1. The development of instruments to measure the low frequency responses (i.e. at seismic frequencies) of these samples.
2. True field experiments in which surface and downhole seismic observations can be tied to expected in situ conditions. This could be a rich area of mul-

tidisciplinary research that would involve linking physical property laboratory measurements to field tests and reservoir modelling.

Bibliography

[1] D. Qin G.-K. Plattner M. Tignor S.K. Allen J. Boschung A. Nauels Y. Xia V. Bex Stocker, T.F. and P.M. Midgley (eds.). Ipcc, 2013: Summary for policymakers. in: Climate change 2013: The physical science basis. contribution of working group i to the fifth assessment report of the intergovernmental panel on climate change. Technical report, Cambridge University Press, Cambridge, United Kingdom and New York, NY, USA., 2013.

[2] Jerry M. Harris et al. Subsurface monitoring of geological CO_2 storage. Technical report, The Global Climate and Energy Project (GCEP) at Stanford University, 2007.

[3] R. S. Lakes. *Viscoelastic Materials*. Cambridge University Press, 2009.

[4] Helen Yam. CO_2 rock physics: a laboratory study. Thesis, University Of Alberta, 2011.

[5] Maciej Matyka and Zbigniew Koza. How to calculate tortuosity easily? In *AIP Conf. Proc.*, volume 1453, page 1722, 2012.

[6] J. H. Butler and S. H. Montzka. The noaa annual greenhouse gas index (aggi). *NOAA Earth System Research Laboratory, R/GMD, 325 Broadway, Boulder, CO 80305-3328*, 2013.

[7] S. A. Rackley. Carbon capture and storage. *Elsevier*, 2010.

[8] B. A. Seibel and P. J. Walsh. Potential impacts of CO_2 injection on deep sea biota. *Science, 294, 319-320*, 2001.

[9] Seibel B. A. Feely R. A. Fabry, V. J. and J. C. Orr. Impacts of ocean acidification on marine fauna and ecosystem processes. *ICES Journal of Marine Science, 65, 414-432*, 2008.

[10] Doetsch J Fiandaca G Christiansen AV Gazoty A Cahill AG & Jakobsen R Auken, E. Imaging subsurface migration of dissolved CO_2 in a shallow aquifer using 3-d time-lapse electrical resistivity tomography. *Journal of Applied Geophysics*, (101):31–41, 2014.

[11] Kowalsky M B Doughty C Finsterle S Ajo-Franklin J B Carrigan C R Yang X J Hovorka SD & Daley T M Doetsch, J. Constraining CO_2 simulations by coupled modeling and inversion of electrical resistance and gas composition data. *International Journal of Greenhouse Gas Control*, 18:510–522, 2013.

[12] Toomey A Hoversten M Gasperikova E & Dodds-K Sherlock, D. Gravity monitoring of CO_2 storage in a depleted gas field: A sensitivity study. . *Exploration Geophysics*, 37:37–43, 2006.

[13] M Gasperikova, E & Hoversten. Gravity monitoring of CO_2 movement during sequestration: Model studies. *Geophsics*, 73:WA105–WA112, 2008.

[14] & Fabriol H Maxwell SC, White DJ. Passive seismic imaging of CO_2 sequestration at weyburn. *SEG Expanded Abstracts.*, 23:568571, 2004.

[15] Elsayed R. Van Der Meer L. Eiken O.-Ostmo O. Chadwick A. Kirby G. Arts, R. and B. Zinszner. Estimation of the mass of injected CO_2 at sleipner using time-lapse seismic data. *EAGE 64th Annual Conference*, (Paper H-16), 2002.

[16] Ramirez A. Newmark, R. and W. Daily. Monitoring carbon dioxide sequestration using electrical resistance tomography (ert): A minimally invasive method. *Proceedings of the Sixth International Conference on Greenhouse Gas Control Technologies*, pages 353–358, 2002.

[17] Gritto R. Washbourne J. Hoversten, G. M. and T. Daley. Pressure and fluid saturation prediction in a multicomponent reservoir using combined seismic and electromagnetic imaging. *Geophysics*, 68:1580–1591, 2003.

[18] Daley T. M. Gritto, R. and L.R. Myer. Joint cross-well and single-well seismic studies at lost hills, california. *Geophys. Prospect*, 52:323–339, 2004.

[19] Nobuoka D. Azuma H. Xue Z. Saito, H. and D. Tanase. Time-lapse crosswell seismic tomography for monitoring injected $\mathrm{CO_2}$ in an onshore aquifer, nagaoka, japan. *Exploration Geophysics*, 37:30–36, 2006.

[20] Z. Xue J.Q. Shi and S. Durucan. Supercritical $\mathrm{CO_2}$ core flooding and imbibition in tako sandstone influence of sub-core scale heterogeneity. *Int J Greenhouse Gas Control*, 5:7587, 2011.

[21] K. T. Spikes Carter, R. W. and T. Hess. Inversion of multicomponent 3d vertical seismic profile data for porosity and $\mathrm{CO_2}$ saturation at the cranfield injection site, cranfield, ms. *Interpretation*, 2(2):SE77–SE89, 2014.

[22] Z. Saito H. Spetzler J., Xue and O. Nishizawa. Case story: time-lapse seismic crosswell monitoring of $\mathrm{CO_2}$ injected in an onshore sandstone aquifer. *Geophys. J. Int.*, 172:214–225, 2008.

[23] Peterson J Doetsch J & Daley TM Ajo-Franklin, JB. High-resolution characterization of a CO_2 plume using crosswell seismic tomography:

Cranfield, ms, usa. *International Journal of Greenhouse Gas Control*, 18:497–509, 2013.

[24] et al. White DJ. Geophysical monitoring of the weyburn CO_2 flood: Results during 10 years of injection. *Energy Procedia*, 4:36283635, 2011.

[25] Z. Wang and A. M. Nur. Effects of CO_2 flooding on wave velocities in rocks with hydrocarbons: Society of petroleum engineers. *Reservoir Engineering*, 3:429–436, 1989.

[26] Z. Xue and T. Oshumi. Seismic wave monitoring of CO_2 migration in water-saturated porous sandstone. *Exploration Geophysics*, 35:25–32, 2004.

[27] Z. Xue and X. Lei. Laboratory study of CO_2 migration in water-saturated anisotropic sandstone, based on p-wave velocity imaging. *Exploration Geophysics*, 37:10–18, 2006.

[28] X. Lei and Z. Xue. Ultrasonic velocity and attenuation during CO_2 injection into water-saturated porous sandstone: Measurements using difference seismic tomography. *Physics of the Earth and Planetary Interiors*, 176:224234, 2009.

[29] F. Gassmann. ber die elastizitt poroser medien. *Vierteljahrsschrift der Naturforschenden Gesellschaft in Zrich*, 96:1–23, 1951.

[30] Choi H. Park Y. C. Park, K. G. and S. Hwang. Ultrasonic laboratory measurements of the seismic velocity changes due to CO_2 injection. *EGU General Assembly 2009*, page 8497, 2009. Expanded Abstract.

[31] Mur A. Soong Y. Mclendon R. Haljasmaa I. V. Purcell, C. and W. Harbert. Integrating velocity measurements in a reservoir rock sample from the sacroc unit with an avo proxy for subsurface supercritical CO_2. *The Leading Edge*, 29:192–195, 2010.

[32] A Liebscher K Zemke and M Wandrey. Petrophysical analysis to investigate the effects of carbon dioxide storage in a subsurface saline aquifer at Ketzin, Germany (CO_2SINK). *Int J Greenhouse Gas Control 2010*, page doi: 10.1016/j.ijggc.2010.04.008, 2010.

[33] M. Lwinb A.F. Sigginsa and P. Wismanb. Laboratory calibration of the seismo-acoustic response of $\mathrm{CO_2}$ saturated sandstones. *International Journal of Greenhouse Gas Control*, 4:920927, 2010.

[34] Magnus Soldal istein Johnsen Binyam L. Alemu1, Eyvind Aker and Per Aagaard. Effect of sub-core scale heterogeneities on acoustic and electrical properties of a reservoir rock: a $\mathrm{CO_2}$ flooding experiment of brine saturated sandstone in a computed tomography scanner. *Geophysical Prospecting*, 61(1):235250, 2013.

[35] Kneafsey T. J. Daley T. M. Freifeld B. M. Nakagawa, S. and E. V. Rees. Laboratory seismic monitoring of supercritical $\mathrm{CO_2}$ flooding in sandstone cores using the Split Hopkinson Resonant Bar technique with concurrent x-ray Computed Tomography imaging. *Geophysical Prospecting*, 61: 254269, 2013.

[36] Maxim Lebedev, Vassili Mikhaltsevitch, Olga Bilenko, Tess Dance, Marina Pervukhina, and Boris Gurevich. Experimental laboratory study on the acoustic response of sandstones during injection of supercritical $\mathrm{CO_2}$ on crc2 sample from Otway Basin Australia. *Energy Procedia.*, 37: 4106–4113, 2013.

[37] H. Yam and D.R. Schmitt. Phase state of $\mathrm{CO_2}$ influences seismological properties: Experimental verification. *submitted Earth Planet. Sci. Lett.*, page 56, 2012.

[38] D. R. Schmitt H. Yam Njiekak, G. and R. Kofman. $\mathrm{CO_2}$ rock physics

as part of the Weyburn-Midale geological storage project. *International Journal of Greenhouse Gas Control*, 16:S118S133, 2013.

[39] Lawrence E. Malvern. *Introduction to the Mechanics of a Continuous Medium*. Prentice Hall, Inc., 1969.

[40] T. Lay and T. C. Wallace. *Modern Global Seismology in International Geophysics Series,*, volume 58. Academic Press, 1995.

[41] A.B. Bhatia. *Ultrasonic Absorption*. Dover Publications Inc., 1986.

[42] K. Aki and P.G. Richards. *Quantitative Seismology, Theory and Methods*, volume I. W.H. Freeman, San Francisco, 1980.

[43] Roylance D. Engineering viscoelasticity. *Cambridge, MA: MIT Press*, 2001.

[44] James A. Liggett. *Fluid Mechanics*. Mcgraw-Hill College, 1994.

[45] Jiajin Liu De-hua Han and Michael Batzle. Measurement of shear wave velocity of heavy oil. In *SEG Annual Meeting*, 2005.

[46] R Hill. The elastic behaviour of a crystalline aggregate. *Proceedings of the Physical Society*, 65(5):349, 1952.

[47] W. Voigt. Lehrbuch der kristallphysik. *Berlin-Leipzig: Teubner Verlag*, 1928.

[48] A. Reuss. Berechnung der fliegrenze von mischkristallen auf grund der plastizittsbedingung fr einkristalle. *ZAMM - Journal of Applied Mathematics and Mechanics / Zeitschrift fr Angewandte Mathematik und Mechanik*, 9(1):49–58, 1929.

[49] D. G. Willis Biot, M. A. Elastic coefficients of the theory of consolidation. *J. Appl. Mech.*, (24):594601, 1957.

[50] A. M. Bakhorji. *Laboratory Measurements of Static and Dynamic Elastic Properties in Carbonate.* Phd thesis, University of Alberta, 2010.

[51] D. R. Schmitt and M. D. Zoback. Poroelastic effects in the determination of the maximum horizontal principal stress in hydraulic fracturing tests-a proposed breakdown equation employing a modified effective stress relation for tensile failure. *International Journal of Rock Mechanics and Mining Sciences & Geomechanics Abstracts*, 26:499–506, 1989.

[52] A. W Wood. *A textbook of sound.* London: G. Bell and Sons Ltd, 1955.

[53] Coussy O. & Zinszner B. Bourbie, T. *Acoustics of Porous Media.* New York: Gulf Publishing Co, 1987.

[54] & Dvorkin J. Mavko G., Mukerji T. *The Rock Physics Handbook: Tools for Seismic Analysis of Porous Media.* Cambridge University Press, 2009.

[55] Mavko G. Dvorkin J. Nur, A. and D. Galmundi. Critical porosity: The key to relating physical properties to porosity in rocks. In *65th Ann. Internat. Mtg., Soc. Expl. Geophys., Expanded Abstracts*, number 878, 1995.

[56] J. Geertsma and D. C. Smit. Some aspects of elastic wave propagation in fluid-saturated porous solids. *Geophysics*, 26(2), 1961.

[57] J. Dewar. Rock physics for the rest of us an informal discussion. *CSEG Recorder*, 26:42–49, 2001.

[58] M. A. Biot. The theory of propagation of elastic waves in a fluid-saturated solid, ii higher frequency range. *Journal of Acoustical Society of America*, 28:179–191, 1956b.

[59] M. A. Biot. The theory of propagation of elastic waves in a fluid-saturated solid, i lower frequency range. *Journal of Acoustical Society of America*, 28:179–191, 1956a.

[60] D. L. Johnson and T. J. Plona. Acoustic slow waves and the consolidation transition. *Journal of Acoustical Society of America*, 72:556–565, 1982.

[61] Y. Bouzidi and D.R. Schmitt. Measurement of the speed and attenuation of the biot slow wave using a large ultrasonic transmitter. *J. Geophys.Res.*, 114(B08201), 2009.

[62] Y. Bouzidi. *The Acoustic Reflectivity and Transmissivity of Liquid Saturated Porous Media: Experimental Tests of Theoretical Concepts*. Thesis, University of Alberta, 2003.

[63] R. B. Gordon and L. A. Davis. Velocity and attenuation of seismic waves in imperfectly elastic rock. *Journal of Geophysical Research*, 73:3917–3935, 1968.

[64] B. McKavanagh and F. D. Stacey. Mechanical hysteresis in rocks at low strain amplitudes and seismic frequencies. *Physics of the Earth and Planetary Interiors*, 8:246–250, 1974.

[65] K. Winkler. *The effects of pore fluids and frictional sliding on seismic attenuation*. Thesis, Stanford University, 1979.

[66] S. G. O'Hara. Influence of pressure, temperature, and pore fluid on the frequency-dependent attenuation of elastic waves in berea sandstone. *Physical Review A*, 45:1780–1792, 1985.

[67] Batzle M. L. Yin, C. S. and B. J. Smith. Effects of partial liquid gas saturation on extensional wave attenuation in berea sandstone. *Geophysical Research Letters*, 19:1399–1402, 1992.

[68] Le Rousseau J. H. L. Scales J. A. Zadler, B. J. and M. L. Smith. Resonant ultrasound spectroscopy: theory and application. *Geophysical Journal International*, 156:154–169, 2004.

[69] K. Winkler and T. Plona. Technique for measuring ultrasonic velocity and attenuation spectra in rocks under pressure. *Journal of Geophysical Research*, 87:776–780, 1982.

[70] C. McCann and J. Sothcott. Laboratory measurements of the seismic properties of sedimentary rocks. *The Geological Society, London, Special Publications*, 65:285–297, 1992.

[71] E. Mashinkskii. Experimental study of the amplitude effect on wave velocity and attenuation in consolidated rocks under confining pressure. *Journal of Geophysics and Engineering*, 44:161–178, 2005.

[72] J. B. Molyneux and D. R. Schmitt. Compressional-wave velocities in attenuating media: A laboratory physical model study. *Geophysics*, 65: 1162–1167, 2000.

[73] X. Zhu and Z. Meng. *Actuators, piezoelectric ceramic, functional gradient: Encyclopedia of Smart Material*. John Wiley and Sons, 2002.

[74] D. Hemsing. Laboratory determination of seismic anisotropy in sedimentary rock from the western canadian sedimentary basin. M.sc. thesis, University of Alberta, 2007.

[75] NIST Chemistry WebBook. http://webbook.nist.gov/chemistry/.

[76] Wendl M C. Fundamentals of heat transfer theory and applications, class notes for ME 371. *Departments of Mechanical Engineering and School of Medicine, Washington University, Saint Louis, U.S.A*, 2005.

[77] G. Njiekak Kofman R., A. Rabbani. Influence of cooling and heating rate on co_2 condensation and evaporation observed in a saturated synthetic rock sample. In *GeoConvention 2013*, 2013.

[78] AH Jay. The thermal expansion of quartz by x-ray measurements. In *Proceedings of the Royal Society of London Series a-Containing Papers*

of a Mathematical and Physical Character, volume 142, pages 237–247, 1933.

[79] Lukaszek TJ & Ballato AD Bechmann, R. Higher-order temperature coefficients of elastic stiffnesses and compliances of alpha-quartz. In *Proceedings of the Institute of Radio Engineers*, volume 50, pages 1812–1822, 1962.

[80] O. Coussy Bourbie, T. and B. Zinsner. *Acoustics of Porous Media*. Gulf Publishing Co., Houston, 1987.

[81] C. F. Jov E. H. Oelkers Kieffer, B. and J. Schott. An experimental study of the reactive 497 surface area of the fontainebleau sandstone as a function of porosity, permeability, and fluid 498 flow rate. *Geochim. Cosmochim. Acta*, 63:3525–3534, 1999.

[82] Bernard Zinszner and Franois-Marie Pellerin. *A Geoscientist's Guide to Petrophysics*. Editions Technip, 2007.

[83] M. Bertrand-Ayraullt Thiry, M. and J. C. Grisoni. Ground-water silicification and leaching in sands: example of the fontainebleau sandstone (oligocene) in the paris basin. *Geol. 556 Soc. Amer. Bull.*, 100:1283–1290, 1988.

[84] T. Bourbi and B. Zinsner. Hydraulic and acoustic properties as a function of porosity in 451 fontainebleau sandstone. *J. Geophys. Res*, 90:11524–11532, 1985.

[85] P.M. Doyen. Permeability, conductivity, and pore geometry of sandstone. *J. Geophys. 469 Res.*, 93:7729–7740, 1988.

[86] J. P. Du Plessis and L. I. Roos. Predicting the hydrodynamic permeability of sandstone 471 with a pore scale model. *J. Geophys. Res.*, 99:19771–19776, 1994.

[87] G. Mavko and A. Nur. The effect of a percolation threshold in the kozeny-carman 516 relation. *Geophysics*, 62:1480–1482, 1997.

[88] C. Durand. Improvement of fluid distribution description during floods by combined use 473 of x-ray ct scan and continuous local resistivity measurements. In *The 17th International Symposium of the Society of Core Analysts*, number SCA2003-29, page 112. Society of Core Analysts, Pau, France, 2003.

[89] C.H. Arns-A. Ghous A. Sakellariou T.J. Senden A.P. Sheppard R.M. 503 Sok H. Averdunk W.V. Pinczewski G.S.Padhy Knackstedt, M.A. and M.A. Ioannidis. Pore scale 504 analysis of electrical resistivity in complex core material. In *21st International Symposium of 505 the Society of Core Analysts,Calgary, Canada*, volume 33, page 112, 2007.

[90] M. Han, S. Youssef, E. Rosenberg, M. Fleury, and P. Levitz. Deviation from archies law in partially saturated porous media: Wetting film versus disconnectedness of the conducting phase. *Phys. Rev. E*, 79(3):031127, 2009.

[91] Jack Dvorkin Gomez C.T. and T. Vanorio. Laboratory measurements of porosity, permeability, resistivity, and velocity on fontainebleau sandstones. *Geophysics*, 75(6):E191E204, 2010.

[92] Y. Cinar W. V. Pinczewski Yanici S, J.-Y. Arns and C. H. Arns. Percolation effects of grain contacts in partially saturated sandstones: deviations from archies law. *Transport in Porous Media*, 96:457467, 2013.

[93] Edward W. Washburn. The dynamics of capillary flow. *Physical Review*, 17(3):273–283, 1921.

[94] L. J. Klinkenberg. The permeability of porous media to liquids and gases. *Drilling and Production Practice*, pages 200–213, 1941.

[95] Morrow N. R. Kilmer, N. H. and J. K Pitman. Pressure sensitivity of low permeability sandstones. *Journal of Petroleum Science and Engineering*, 1:65–81, 1987.

[96] D. S. Springer, Cullen S. J. Loaiciga, H. A., and L. G. Everetta. Air permeability of porus materials under controlled laboratory conditions. *Ground Water*, 36:558–565, 1998.

[97] Pruess K. Wu, Y. and P. Persoff. Gas flow in porous media with klinkenberg effects. *Transport in Porous Media*, 32:117–137, 1998.

[98] C. Scala Sen, P. N. and M. H. Cohen. Self-similar model for sedimentary rocks with application to the dielectric constant of fused glass beads. *Geophysics*, 46:781–795, 1981.

[99] A. Revil. Genesis of mud volcanoes in sedimentary basins: A solitary wave-based mechanism. *Geophysical research letters*, 29(12,):15–115–4, 2002.

[100] A. Revil. Electrical conductivity and permeability of the fontainebleau sandstone. *To Be Published*.

[101] A.C. Kak and M. Slaney. Principles of computerized tomographic imaging. *SIAM, New York*, 2001.

[102] Hu Dong. *Micro-CT imaging and pore network extraction.* PhD thesis, Imperial College Lodon, 2007.

[103] J. D. Bass. *Elasticity of Minerals, Glasses, and Melts in Mineral Physics and Crystallography: A Handbook of Physical Constants.* American Geophysical Union, Washington, USA, 1995.

[104] Chadwick A. Eiken O. Thibeau S. Nooner S. Arts, R. 10 years experience of monitoring CO_2 injection in the utsira sand at sleipner, offshore norway. *First Break*, 26:2936, 2008.

[105] Noy D. Lindeberg E. Arts R. Eiken O. Williams G. Chadwick, R.A. Calibrating reservoir performance with time-lapse seismic monitoring and flow simulations of the sleipner CO_2 plume. *8th International Conference on Greenhouse Gas Control Technologies (GHGT-8), Trondheim, Norway*, 2006.

[106] Michael E. Cates Zhijing Wang and Robert T. Langan. Seismic monitoring of a CO_2 flood in a carbonate reservoir; a rock physics study. *Geophysics*, 63:1604–1617, 1998.

[107] Marion D. and Jizba D. *Acoustic Properties of Carbonate Rocks: Use in Quantitative Interpretation of Sonic and Seismic Measurements.* Society of Exploration Geophysicists, 1997.

[108] Colpaert A. Eberli G.P. Weger R.J. Baechle, G.T. Effects of microporosity on sonic velocity in carbonate rocks. *The Leading Edge*, 27:10121018, 2008.

[109] Peter Japsen Christian Hier Gary Mavko andJacob M. Pedersen Birte Rgen, Ida L. Fabricius. Ultrasonic velocities of north sea chalk samples: influence of porosity, fluid content and texture. *Geophysical Prospecting*, 53:481496, 2005.

Appendices

AppendixA The Franc Fontainebleau Sample

Mass (g)	Grain Density kg/m^3	Porosity (%)	Modal Pore Size (μm)	Air Permeability (mD)	Tortousity (unitless)
137.16	2640	6.28 (Hg porosimeter), 8 (Helium Pycnometer)	7.23	16.58	7.09

Table A.1: Petrophysical properties measured from Franc Fontainebleau sandstone sample

AppendixA.1 Dry Runs

AppendixA.1.1 Room Temperature, T= 21 ^0C

Confining Pressure MPa	V_p (m/s)	V_s (m/s)
6.02	3964 ± 13	2382 ± 8
8.02	4140 ± 13	2497 ± 8
10	4329 ± 14	2652 ± 8
15.99	4769 ± 16	3011 ± 10
19.99	4973 ± 16	3154 ± 10
25.01	5138 ± 17	3260 ± 10
29.97	5189 ± 17	3354 ± 11
35	5236 ± 17	3404 ± 11
39.98	5296 ± 17	3426 ± 11
45	5296 ± 17	3452 ± 11
50	5350 ± 17	3475 ± 11
55	5296 ± 17	3504 ± 11
50	5363 ± 18	3477 ± 11
45	5302 ± 17	3477 ± 11
40	5302 ± 17	3452 ± 11
35	5302 ± 17	3426 ± 11
30	5308 ± 17	3379 ± 11
25	5189 ± 17	3333 ± 11
20	5081 ± 17	3240 ± 10
16	4973 ± 16	3154 ± 10
10	4631 ± 15	2865 ± 9
8	4407 ± 14	2684 ± 9
6	4254 ± 14	2485 ± 8

Table A.2: Dry P- and S-wave velocities of the Franc Fontaineblue sandstone at T= 21 ^0C under various confining pressure.

AppendixA.1.2 High Temperature, T= 50 ^0C

Confining Pressure MPa	V_p (m/s)	V_s (m/s)
6.02	4032 ± 14	2419 ± 8
8.02	4254 ± 15	2580 ± 8
10	4411 ± 15	2746 ± 9
15.99	4769 ± 17	3031 ± 10
19.99	5027 ± 18	3154 ± 10
25.01	5027 ± 18	3260 ± 11
29.97	5189 ± 18	3330 ± 11
35	5178± 18	3379 ± 11
39.98	5236 ± 18	3401 ± 11
45	5357 ± 19	3452 ± 11
50	5350 ± 19	3449 ± 11
55	5296 ± 19	3477 ± 12
50	5363 ± 19	3477 ± 12
45	5302 ± 19	3477 ± 11
40	5242 ± 18	3452 ± 11
35	5242 ± 18	3426 ± 11
30	5189 ± 18	3379 ± 11
25	5189 ± 18	3333 ± 11
20	5027 ± 18	3240 ± 11
16	5027 ± 18	3154 ± 10
10	4678 ± 16	2865 ± 10
8	4492 ± 16	2684 ± 9
6	4374 ± 15	2485 ± 8

Table A.3: Dry P- and S-wave velocities of the Franc Fontaineblue sandstone at T= 50 ^0C under various confining pressure.

AppendixA.2 Nitrogen measurements

Pore Pressure MPa	V_p (m/s)	V_s (m/s)
1.00	4953 ± 16	3141 ± 10
2.03	4952 ± 16	3141 ± 10
3.96	4955 ± 16	3141 ± 10
6.00	4952 ± 16	3140 ± 10
7.99	4949 ± 16	3140 ± 10
10.00	4952 ± 16	3139 ± 10
12.02	4954 ± 16	3139 ± 10
9.99	4957 ± 16	3140 ± 10
8.00	4970 ± 16	3140 ± 10
5.99	4972 ± 16	3140 ± 10
4.02	4974 ± 16	3143 ± 10
1.98	4977 ± 16	3141 ± 10
0.98	4973 ± 16	3141 ± 10

Table A.4: Nitrogen saturated P- and S-wave velocities of the Franc Fontaineblue sandstone under various pore pressure.

AppendixA.3 CO_2 saturated measurements

Liquid to Gas Transition Measurements

Pore Pressure MPa	V_p (m/s)	V_s (m/s)
1.00	5054 ± 16	3166 ± 10
3.00	4990 ± 16	3151 ± 10
4.97	4988 ± 16	3131 ± 10
5.98	4912 ± 16	3070 ± 10
6.99	4905 ± 16	3070 ± 10
8.01	4914 ± 16	3076 ± 10
10	4911 ± 16	3076 ± 10
15	4915 ± 16	3087 ± 10
20.00	4914 ± 16	3090 ± 10
15	4917 ± 16	3102 ± 10
10	4922 ± 16	3099 ± 10
8	4924 ± 16	3098 ± 10
7.00	4931 ± 16	3098 ± 10
6.0	4921 ± 16	3102 ± 10
5	5063 ± 17	3188 ± 10
3	5082 ± 17	3221 ± 10
1.00	5102 ± 17	3235 ± 10

Table A.5: CO_2 saturated P- and S-wave velocities of the Franc Fontaineblue sandstone under various pore pressure in the case of liquid to gas transition.

AppendixA.3.1 Gas to Supercritical fluid Transition Measurements

Pore Pressure MPa	V_p (m/s)	V_s (m/s)
1.00	5054 ± 18	3199 ± 11
2.92	5040 ± 18	3190 ± 11
5.02	5009 ± 18	3170 ± 10
6.02	5008 ± 18	3163 ± 10
7.07	4990 ± 17	3154 ± 10
7.98	4989 ± 17	3148 ± 10
10.01	4964 ± 17	3126 ± 10
15	4936 ± 17	3095 ± 10
20.00	4919 ± 17	3072 ± 10
15	4938 ± 17	3108 ± 10
10	4975 ± 17	3139 ± 10
8	4988 ± 17	3160 ± 10
7.00	4995 ± 17	3171 ± 10
6.0	5002 ± 17	3177 ± 11
3	5047 ± 18	3201 ± 11
1.00	5102 ± 18	3207 ± 11

Table A.6: CO_2 saturated P- and S-wave velocities of the Franc Fontaineblue sandstone under various pore pressure in the case of gas to supercritical fluid transition.

AppendixA.3.2 Liquid to Supercritical fluid Transition Measurements at $P_p = 8MPa$

Temperature ^0C	V_p (m/s)	Temperature ^0C	V_s (m/s)
50.00	5059 ± 8	50.00	3209 ± 4
47.00	5065 ± 8	47.00	3211 ± 4
45.00	5070 ± 8	45.00	3209 ± 4
41.90	5092 ± 8	41.50	3213 ± 4
40.00	5081 ± 8	40.00	3213 ± 4
38.00	5087 ± 8	38.00	3222 ± 4
35.00	5092 ± 8	35.00	3220 ± 4
33.00	5092 ± 8	33.00	3220 ± 4
32.00	5092 ± 8	32.00	3215 ± 4
31.00	5098 ± 8	31.00	3217 ± 4
30.00	5098 ± 8	30.00	3220 ± 4
29.00	5098 ± 8	29.00	3220 ± 4
27.00	5104 ± 8	27.00	3222 ± 4
25.00	5104 ± 8	25.00	3226 ± 4
24.00	5109 ± 8	24.00	3226 ± 4
23.00	5115 ± 8	23.00	3229 ± 4
22.00	5115 ± 8	21.00	3231 ± 4
21.00	5120 ± 8	18	3224 ± 4
18	5115 ± 8	20.00	3224 ± 4

Temperature ^0C	V_p (m/s)	Temperature ^0C	V_s (m/s)
20.00	5121 ± 8	21.30	3224 ± 4
21.00	5121 ± 8	23.00	3224 ± 4
23.00	5132 ± 8	25.00	3224 ± 4
25.00	5121 ± 8	27.00	3221 ± 4
27.00	5121 ± 8	29.00	3221 ± 4
29.00	5115 ± 8	30.00	3215 ± 4
30.00	5110 ± 8	31.00	3208 ± 4
31.00	5110 ± 8	32.00	3213 ± 4
32.00	5110 ± 8	33.00	3208 ± 4
33.00	5098 ± 8	35.00	3201 ± 4
35.00	5098 ± 8	38.00	3208 ± 4
38.00	5098 ± 8	41.00	3208 ± 4
40.00	5093 ± 8	42.00	3213 ± 4
42.00	5098 ± 8	45.00	3210 ± 4
45.00	5082 ± 8	47.00	3204 ± 4
47.00	5082 ± 8	50.00	3201 ± 4
50.00	5076 ± 8		

Table A.7: CO_2 saturated P- and S-wave velocities of the Franc Fontaineblue sandstone under various pore pressure in the case of Liquid to supercritical fluid transition.

AppendixA.4 Water measurements

Pore Pressure MPa	V_p (m/s)	V_s (m/s)
1.00	5223 ± 8	3277 ± 3
2.00	5228 ± 8	3282 ± 3
4.00	5219 ± 8	3281 ± 3
6.00	5216 ± 8	3281 ± 3
8.00	5219 ± 8	3281 ± 3
10.00	5221 ± 8	3285 ± 4
12.00	5218 ± 8	3284 ± 4
15.00	5220 ± 8	3284 ± 4
20.00	5235 ± 8	3290 ± 4
23.00	5237 ± 8	3289 ± 4
25.00	5240 ± 8	3294 ± 4
23.00	5229 ± 8	3290 ± 4
20.00	5233 ± 8	3290 ± 4
15.00	5239 ± 8	3291 ± 4
12.00	5243 ± 8	3292 ± 4
10.00	5233 ± 8	3292 ± 4
8.00	5236 ± 8	3288 ± 4
6.00	5238 ± 8	3288 ± 4
4.00	5241 ± 8	3293 ± 4
2.00	5220 ± 8	3287 ± 4
1.00	5233 ± 8	3287 ± 4

Table A.8: Water saturated P- and S-wave velocities of the Franc Fontaineblue sandstone under various pore pressure.

AppendixB The Vif Fontainebleau Sample

Mass (g)	Grain Density kg/m^3	Porosity (%)	Modal Pore Size (μm)	Air Permeability (mD)	Tortousity (unitless)
167.2	2647	12.5 (Hg porosimeter), 10 (Helium Pycnometer)	17.25	16.56	3.673

Table A.9: Petrophysical properties measured from Vif Fontainebleau sandstone sample

AppendixB.1 Dry Runs

AppendixB.1.1 Room Temperature, T= 21 ^0C

Confining Pressure MPa	V_p (m/s)	V_s (m/s)
1.01	3144 ± 7	2258 ± 5
2.96	3223 ± 8	2292 ± 5
6	3256 ± 8	2299 ± 5
7.98	3251 ± 8	2331 ± 5
10.03	3589 ± 9	2564 ± 5
12.98	3911 ± 10	2853 ± 6
15.95	4235 ± 12	3139 ± 7
19.97	4441 ± 13	3336 ± 8
24.98	4715 ± 14	3603 ± 9
29.97	4893 ± 15	3794 ± 10
35	5010 ± 15	3930 ± 10
39.96	5123 ± 16	4059 ± 11
50.28	5288 ± 17	4252 ± 12
54.98	5325 ± 17	4307 ± 12
49.95	5278 ± 17	4270 ± 12
45	5233 ± 16	4201 ± 11
40.03	5162 ± 16	4139 ± 11
35.00	5081 ± 15	4010 ± 11
29.9	4961 ± 15	3881 ± 10
25.01	4797 ± 14	3699 ± 9
20.03	4598 ± 13	3488 ± 9
16.05	4350 ± 12	3264 ± 8
13.05	4140 ± 11	3052 ± 7
9.98	3857 ± 10	2792 ± 6
8.01	3850 ± 10	2579 ± 5
6.03	3717 ± 9	2307 ± 5
3.02	3626 ± 9	2305 ± 5
1.00	3479 ± 9	2297 ± 5

Table A.10: Dry P- and S-wave velocities of the Vif Fontaineblue sandstone at T= 21 ^0C under various confining pressure.

AppendixB.1.2 High Temperature, T= 50 ^0C

Confining Pressure MPa	V_p (m/s)	V_s (m/s)
1	2505 ± 5	2222 ± 4
3	2673 ± 6	2252 ± 5
6.03	2724 ± 6	2274 ± 5
7.93	2976 ± 7	2357 ± 5
9.99	3559 ± 9	2574 ± 5
12.98	3602 ± 9	2849 ± 6
16	4189 ± 11	3070 ± 7
19.99	4441 ± 13	3317 ± 8
25.02	4679 ± 14	3563 ± 9
30	4858 ± 14	3743 ± 10
35.03	4993 ± 15	3910 ± 10
40	5102 ± 16	4027 ± 11
44.93	5180 ± 16	4132 ± 11
50	5251 ± 16	4214 ± 11
54.97	5320 ± 17	4277 ± 12
50.04	5279 ± 17	4240 ± 12
45.04	5229 ± 17	4169 ± 12
40.02	5149 ± 16	4084 ± 11
35.02	5123 ± 16	3984 ± 11
30.02	4949 ± 15	3844 ± 10
25	4808 ± 14	3683 ± 9
20.04	4622 ± 13	3476 ± 9
13.03	4171 ± 11	3041 ± 7
10.01	3859 ± 10	2778 ± 6
8	3148 ± 7	2552 ± 5
6.05	2990 ± 7	2315 ± 5
3.01	2848 ± 6	2303 ± 5
0.92	2615 ± 6	2263 ± 5

Table A.11: Dry P- and S-wave velocities of the Franc Fontaineblue sandstone at T= 50 ^0C under various confining pressure.

AppendixB.2 Nitrogen measurements

Pore Pressure MPa	V_p (m/s)	V_s (m/s)
1.00	4518 ± 17	3393 ± 11
2.03	4569 ± 17	3394 ± 11
3.96	4573 ± 17	3458 ± 11
6.00	4577 ± 17	3460 ± 11
7.99	4631 ± 17	3493 ± 11
10.00	4635 ± 17	3495 ± 11
12.02	4691 ± 18	3530 ± 12
9.99	4691 ± 18	3495 ± 11
8.00	4635 ± 18	3493 ± 11
5.99	4631 ± 18	3492 ± 11
4.02	4627 ± 18	3458 ± 11
1.98	4619 ± 18	3488 ± 11
0.98	4617 ± 18	3455 ± 11

Table A.12: Nitrogen saturated P- and S-wave velocities of the vif Fontaineblue sandstone under various pore pressure.

AppendixB.3 CO_2 saturated measurements

AppendixB.3.1 Liquid to Gas Transition Measurements

Pore Pressure MPa	V_p (m/s)	V_s (m/s)
1.00	5130 ± 16	3166 ± 10
3.00	5110 ± 16	3960 ± 9
4.97	5100 ± 16	3940 ± 9
5.98	5000 ± 15	3800 ± 9
6.99	5000 ± 15	3790 ± 9
8.01	5000 ± 15	3790 ± 9
10	5000 ± 15	3780 ± 9
15	5010 ± 15	3780 ± 9
20.00	5020 ± 15	3770 ± 9

Table A.13: CO_2 saturated P- and S-wave velocities of the Vif Fontaineblue sandstone under various pore pressure in the case of liquid to gas transition.

AppendixB.3.2 Gas to Supercritical fluid Transition Measurements

Pore Pressure MPa	V_p (m/s)	V_s (m/s)
1.00	5074 ± 15	3947 ± 9
2.92	5067 ± 15	3948 ± 9
5.02	5047 ± 15	3867 ± 9
6.02	5045 ± 15	3844 ± 9
7.07	5030 ± 15	3828 ± 9
7.98	5002 ± 15	3809 ± 9
10.01	4969 ± 15	3785 ± 9
15	4961 ± 15	3751 ± 9
20.00	4969 ± 15	3866 ± 9

Table A.14: CO_2 saturated P- and S-wave velocities of the Vif Fontaineblue sandstone under various pore pressure in the case of gas to supercritical fluid transition.

AppendixB.3.3 Liquid to Supercritical fluid Transition Measurements at $P_p = 8MPa$

Temperature ^0C	V_p (m/s)	V_s (m/s)
50.10	5026 ± 15	3776 ± 8
47.10	5026 ± 15	3771 ± 8
45.00	5014 ± 15	3768 ± 9
41.20	5012 ± 15	3771 ± 9
39.10	5004 ± 15	3746 ± 9
35.10	4994 ± 15	3733 ± 8
33.10	4986 ± 15	3736 ± 8
31.10	4979 ± 15	3737 ± 8
28.90	4971 ± 15	3740 ± 9
27.3	4973 ± 15	3739 ± 9
25.1	4969 ± 15	3740 ± 9
24.4	4964 ± 15	3737 ± 9
22.10	4968 ± 15	3735 ± 9

Table A.15: CO_2 saturated P- and S-wave velocities of the Vif Fontaineblue sandstone under various pore pressure in the case of Liquid to supercritical fluid transition.